Applications of time-dependent configuration-interaction singles for photoelectrons in attosecond and free-electron laser sciences

Bertolino, Mattias

2023

Applications of time-dependent configuration-interaction singles for photoelectrons in attosecond and free-electron laser sciences

MATTIAS BERTOLINO
DEPARTMENT OF PHYSICS | FACULTY OF ENGINEERING | LUND UNIVERSITY

Applications of time-dependent configuration-interaction singles for photoelectrons in attosecond and free-electron laser sciences

Applications of time-dependent configuration-interaction singles for photoelectrons in attosecond and free-electron laser sciences

by Mattias Bertolino

LUND
UNIVERSITY

Thesis for the degree of Doctor of Philosophy in Physics
Thesis advisors: Assoc. Prof. Jan Marcus Dahlström, Prof. Anne L'Huillier, Prof. Eva Lindroth
Faculty opponent: Prof. Alicia Palacios

To be presented, with the permission of the Faculty of Engineering, LTH of Lund University, for public criticism in Rydbergsalen at the Department of Physics on Friday, the 26th of May 2023 at 09:15.

Organization
LUND UNIVERSITY

Department of Physics
Box 118
SE–221 00 LUND
Sweden

Document name
DOCTORAL DISSERTATION

Date of disputation
2023-05-26

Sponsoring organization

Author(s)
Mattias Bertolino

Title and subtitle
Applications of TDCIS for photoelectrons in attosecond and free-electron laser sciences

Abstract
This thesis addresses the theoretical treatment of photoelectrons in attosecond and free-electron laser sciences. We have implemented methods that extract information on the photoionization process, which we use to investigate interferometric schemes with particular focus on multiphoton ionization and strong-field effects in attosecond metrology and coherent control of photoelectrons in free-electron laser science.

This thesis comprises six papers.

In Paper I, we investigate photoelectron angular distributions in laser-assisted photoionization. We confirm earlier predictions of a propensity rule for continuum transitions and discuss interference effects.

In Paper II, we interpret experiments from attosecond and free-electron laser sciences in terms of an interaction phase and devise a rule of thumb for predicting general phase and amplitude effects in these experiments.

In Paper III, we experimentally determine the one-photon dynamics for each angular momentum channel, as a function of energy, by studying two-photon photoelectron angular distributions.

In Paper IV, we experimentally and theoretically investigate periodic population transfer between two bound states in helium at XUV wavelengths by studying the photoelectron spectra.

In Paper V, we present a general implementation of time-dependent configuration interaction for atomic systems.

In Paper VI, we discuss size-consistency problems in velocity gauge in truncated configuration spaces and propose a correction based on the Thomas–Reiche–Kuhn sum rule. We further predict the occurrence of dynamical interference in laser-assisted photoionization.

Key words
Laser-assisted photoionization, photoelectron interferometry, attosecond physics, free-electron laser, second quantization, time-dependent configuration-interaction singles, surface-flux techniques

Classification system and/or index terms (if any)

Supplementary bibliographical information

Language
English

ISSN and key title

ISBN
978-91-8039-514-4 (print)
978-91-8039-515-1 (pdf)

Recipient's notes

Number of pages
204

Price

Security classification

Applications of time-dependent configuration-interaction singles for photoelectrons in attosecond and free-electron laser sciences

by Mattias Bertolino

LUND
UNIVERSITY

A doctoral thesis at a university in Sweden takes either the form of a single, cohesive research study (monograph) or a summary of research papers (compilation thesis), which the doctoral student has written alone or together with one or several other author(s).

In the latter case the thesis consists of two parts. An introductory text puts the research work into context and summarizes the main points of the papers. Then, the research publications themselves are reproduced, together with a description of the individual contributions of the authors. The research papers may either have been already published or are manuscripts at various stages (in press, submitted, or in draft).

Cover illustration front: A field. A photoelectron spectrum.

Cover illustration back: A coffee in our apartment in Lund.

Funding information: The thesis work was financially supported by the Knut and Alice Wallenberg Foundation.

Division of Mathematical Physics, Faculty of Engineering, LTH, Department of Physics

ISBN: 978-91-8039-514-4 (print)
ISBN: 978-91-8039-515-1 (pdf)

Printed in Sweden by Media-Tryck, Lund University, Lund 2023

Contents

List of publications and contributions of the author

This thesis is based on the following publications, referred to by their Roman numerals:

I **Propensity Rules and Interference Effects in Laser-Assisted Photoionization of Helium and Neon**
M. Bertolino, D. Busto, F. Zapata, J. M. Dahlström
J. Phys. B: At. Mol. Opt. Phys., pp. 144002 (2020)

We investigate angular dependencies of photoelectrons created using laser-assisted photoionization. Based on the asymmetric angular dependency in sidebands reached by absorption and sidebands reached by emission, we confirm earlier reported results of a propensity rule for continuum–continuum transitions. We further find that this propensity rule may be masked by incoherent signals of different magnetic quantum numbers.

Contribution: I performed all the calculations and produced all the figures. I implemented the time-dependent surface-flux method to be used with the existing time-dependent configuration-interaction singles code in Fortran. I wrote the first draft of the manuscript and contributed actively to the communication with the editor and the referees.

II **Multiphoton Interaction Phase Shifts in Attosecond Science**
M. Bertolino, J. M. Dahlström
Phys. Rev. Research, pp. 013270 (2021)

We study phase shifts in three interferometric photoionization experiments from attosecond and free-electron laser sciences. We find that for experiment with an unbalanced number of interactions in the arms, the photoelectron distribution depends on the directionality of the photoelectron and on an *interaction phase* that accumulates for each interaction. We argue that this interaction phase is often overlooked and that it is needed to explain the general phase modulations in interferometric photoionization experiment and to ensure conservation laws in continuum transitions.

Contribution: I performed all the calculations and produced all the figures. I wrote the first draft of the manuscript and contributed actively to the interpretation of the results. I contributed actively to the communication with the editor and the referees.

III **Attosecond Dynamics of Multi-Channel Single Photon Ionization**
J. Peschel, D. Busto, M. Plach, M. Bertolino, M. Hoflund, S. Maclot, H. Wikmark, F. Zapata, J. M. Dahlström, A. L'Huillier, P. Eng-Johnsson
Nat Commun, pp. 5205 (2022)

We experimentally determine the one-photon phases and amplitudes, for each angular-momentum channel separately, in outer-shell photoionization of neon with linearly-polarized light. The analysis is based on measuring the two-photon photoelectron-angular distribution and makes use of continuum–continuum propensity rules to implicitly retrieve the information of the one-photon process. The one-photon phases and amplitudes provide the insight necessary for a complete reconstruction of the ultrafast ionization dynamics and the different roles of correlation and centrifugal effects.

Contribution: I was part in the theoretical development of the retrieval algorithm and performed the quantum defect calculations. I contributed to the manuscript with comments and suggestions.

IV **Observation of Rabi Dynamics with a Short-Wavelength Free-Electron Laser**
S. Nandi, E. Olofsson, M. Bertolino, S. Carlström, F. Zapata, D. Busto, C. Callegari, M. Di Fraia, P. Eng-Johnsson, R. Feifel, G. Gallician, M. Gisselbrecht, S. Maclot, L. Neoričić, J. Peschel, O. Plekan, K. C. Prince, R. J. Squibb, S. Zhong, P. V. Demekhin, M. Meyer, C. Miron, L. Badano, M. B. Danailov, L. Giannessi, M. Manfredda, F. Sottocorona, M. Zangrando, J. M. Dahlström
Nature, pp. 488–493 (2022)

We experimentally study coherent periodic population transfer, so called Rabi oscillations, between the ground state in helium and the $1s4p\,^1P_1$ excited state in helium using free-electron laser and report the first direct observation of this process at extreme-ultraviolet wavelengths. The Rabi dynamics are observed in situ by measuring the photoelectron spectra that reveal an Autler–Townes doublet and an avoided crossing. We further find that the photoelectron signal contains information on quantum interference between resonant and nonresonant photoionization pathways.

Contribution: I had an active role in the general theoretical development of this paper together with S. N., E. O. and J. M. D, with emphasis on the time-dependent configuration-interaction singles simulations of the helium atom and the surface-flux analysis of the photoelectrons. In particular, I provided data for Fig. 2(b) and Fig. 4(c) and identified the $1/2$ Rabi-period difference between sign changes of the two ionization channels. I contributed to the manuscript and the communication with the referees with comments and suggestions.

V **General Time-Dependent Configuration-Interaction Singles. II. Atomic Case**
S. Carlström, M. Bertolino, J. M. Dahlström, S. Patchkovskii
Phys. Rev. A, pp. 042806 (2022)

We describe an implementation of a two-component time-dependent configuration-interaction singles method tailored to atomic systems with relativistic pseudopo-

tentials. We provide a detailed presentation of the time-propagation scheme. The method is tested for recent experiments in attosecond physics.

Contribution: I provided reference and benchmarking calculations for mutual verification of the method and implementation. I contributed to the manuscript with comments and suggestions.

VI **Thomas–Reiche–Kuhn Correction for Truncated Configuration-Interaction Spaces: Case of Laser-Assisted Dynamical Interference**
M. Bertolino, S. Carlström, J. Peschel, F. Zapata, E. Lindroth, J. M. Dahlström
Phys. Rev. A, pp. 043108 (2022)

We identify that the velocity-gauge time-dependent configuration-interaction singles method is size inconsistent due to the missing coupling to the space of double excitations. We propose a correction to this based on time-dependent perturbation theory and the Thomas–Reiche–Kuhn sum rule. We further predict that dynamical interference may be observed using a coherent two-color setup that comprises of extreme-ultraviolet and infrared beams that overlap in time and space.

Contribution: I performed a majority of the calculations and produced all the figures. I implemented the Thomas–Reiche–Kuhn correction into the existing time-dependent configuration-interaction singles code. I wrote the first draft of the manuscript and contributed actively to the communication with the editor and the referees.

All papers are reproduced with permission of their respective publishers.

Acknowledgment

With these words, I would like to thank all of you who have been present during my time as a PhD student in Lund. Without you, this thesis would not have been possible.

First of all, I would like to address my supervisor, Marcus Dahlström. I am thankful for the trust and support you have given me, and I have had so much fun exploring physics together with you. I did not know much about attosecond physics when I came to Lund, but you made it sound cool. I have not regretted it a single day! I also want to thank my co-supervisors Eva Lindroth and Anne L'Huillier. You have both inspired me with your knowledge and your kindness. Thank you!

I want to thank the members of the Theoretical Light–Matter Dynamics group. Felipe and Lucia Zapata, thank you for being the encouraging friends you are. Being neighbours with you really made the time here in Lund for me and Nette so much more fun. Thank you Edvin Olofsson, thank you for the interesting discussions we had during the Rabi project. Stefanos Carlström, thank you for sharing your expertise. In particular for your support when writing the t+iSURFF implementation, but also the auxiliary codes like the flexible handling of envelopes and automatic differentiation. Rezvan Tahouri, Jimmy Vinbladh, Asimina Papoulia, and Axel Stenquist, thank you for the friendship and the many interesting discussions we have had on various topics. I have enjoyed them very much! I am happy that I got to see the group expanding from two to nine and working with you has been a real pleasure.

Along the same lines I would like to thank my office mates during the years. Alex Kalaee, for your sharp sense of humour and for creating a fantastic atmosphere in the division – I still want another bite of your Brunswige tårta; Betül Atalay, for your awesome intensity; Fredrik Brange, for your diligence and your friendly approach that I found very inspirational; Martin Andersson, for all the perspectives on life we have shared and for the great pub nights; Philipp Stürmer, for the joy of discovering common interests one at a time – keep up the good coffee; Johan Boström, for the shared technical interest; and Björn Annby-Andersson, for all the good conversations about life in academia; It has been great to share the office with you. Thank you!

A special thanks to Ekin Önder, for being a fantastic friend. It has been great to do a PhD at the same time as you. I look forward to go to the beach many more times! Thanks also to Tor Sjöstrand, for sharing perspectives on scale; Andrea Idini, for good laughs, and Katarina Lindkvist, for all the help in so many matters and for all the good chats. Thank you! I further want to thank the emeriti at the division, with a special thanks to Cecilia Jarlskog. I found it very interesting to listen to stories about the humility of Gian-Carlo Wick, the unsuccessful haircut by John Stewart Bell's father, or the time Niels Bohr sent a recommendation letter to the Swedish government.

I am further grateful to the many collaborators I have worked with and want to send a special thanks to the people at Atomic Physics. Hugo Laurell, what a nice coincidence that we would end up in the same place after graduating from engineering in Uppsala. I've had a great time with you and Gjertrud! David Busto, Jasper Peschel, Saikat Nandi, and Per Eng-Johnsson, thank you for good collaborations and for the experimental work. Thank you Zdeněk Mašín, Jakub Benda, Sergei Patchkovskii for the theoretical collaboration.

Finally, I would like to thank my friends outside work and my family. Vincent Björkquist, Adam Waks, and Lotta Ekblom for all the encouraging conversations we had about life as a PhD student. Also thank you Adam and Lotta Sellmann for providing shelter during my first months in Lund, and Lotta Ekblom the mid of my PhD. My parents Graziano and Kristina, my sisters Engla and Francesca, Carola, Selma, Marco and Kathi, Soile, for your encouragement, my grandpa Gunnar for your encouraging interest in my research, and finally, Nette, for your endless love and the best imaginable support.

Popular summary

Much of our knowledge about the world comes from shining light on objects. Some objects are transparent, while others are opaque and cast shadows. In the 17th century, Isaac Newton let a ray of sunlight, created by a small aperture in his shutter, pass through a prism to separate the white light into its continuous spectrum of frequencies. While he didn't *invent* the rainbow, he showed that white light contains a mixture of many different colors. About a century later, Thomas Young drilled a second hole in the curtain and showed that the two rays interfered in a wave-like manner. Light therefore seemed to be composed of a mixture of waves with different colors, which just like water waves could interfere to produce travelling waves of radiation.

By focusing sunlight into an intense spot we may ignite dry grass and cause a fire. Thus, shining light on things may alter the state of the object irreversibly. In a similar fashion, a pulse of light that hits a single atom may transmit energy to the atom. If the energy that is absorbed by the atom is sufficient, the atom can eject an electron in what is known as the photoelectric effect. Albert Einstein found that the kinetic energy of the emitted electron depended on the frequency of the light, and not the intensity – in sharp contrast to the burning grass. He discovered that the wave-like property of light was insufficient to describe this and proposed the idea of an energy *quantum* of light – the photon. This realization implied particle-like properties of light, and is widely considered as the starting point of the quantum era.

With the invention of the laser in the 1960's came the possibility to produce intense light of a single color whose oscillations, unlike the light of Newton and Young, are well controlled. This light can be tailored to precise conditions, such as ultra-short pulse durations in time or accurate control of frequencies, which has resulted in a large number of Nobel prizes in physics and chemistry such as Zewail's work on *femtochemistry*, Hänsch's work on *frequency combs*, and Strickland's work on the *chirped-pulse amplification*.

One of the early revelations that followed the invention of the laser was the extension of Einstein's theory of the photoelectric effect to the so called multiphoton-ionization effect, where an atom absorbs several photons, of possibly different colors, while ejecting an electron. This effect was a clear proof of the laser's ability to provide stable, coherent and intense radiation, and is both the foundation and the incentive for the theoretical simulations presented in this thesis. Just like light possesses both particle- and wave-like properties, so do electrons. It is therefore possible to do interferometric photoionization experiments, similar to Young's experiment, but with the emitted electrons instead of light. The beauty of these experiments is that both the information on the atomic structure and dynamics get imprinted in the ejected electrons in rich interference structures.

To understand these interferometric ionization experiments, we have implemented meth-

ods that are able to record the flux of electrons as they are ejected. By recording these fluxes, we have studied both the atomic dynamics and the ionization process. We present theoretical insight into the free electronic motion in ionization of noble gas atoms and explained the role of the directionality of the electron in the interference pattern. In particular we have studied experiments where one of the interfering ionization pathways of the electron includes more photon interactions than the other and showed how this affects the interference structures. We have further predicted interference in ionization that arise due to the electron taking the same pathways twice – but at two different times – due to a dynamical shift of the energy of the atom in the field. Moreover, we have studied how atoms can flop between different bound states, while ejecting electrons, due to coherent extreme-ultraviolet light pulses. By fine tuning the frequency of the extreme-ultraviolet radiation to match the energy separation between two energy states, we periodically controlled the state of the atom, and measured the state using the flux of the electrons.

Overall this thesis aims at increasing the understanding of ultrafast control of ionization experiments in atomic physics, with particular focus on electron interferometry with applications in attosecond and free-electron laser sciences.

Populärvetenskaplig sammanfattning

En stor del av vår kunskap om världen kommer från att lysa på föremål. Vissa objekt är transparenta, medan andra är ogenomskinliga och kastar skuggor. På 1600-talet lät Isaac Newton en solstråle, skapad genom en liten öppning i hans persienn, passera genom ett prisma för att separera det vita ljuset i dess kontinuerliga spektrum av frekvenser. Nog för att han inte *uppfann* regnbågen, men han visade att vitt ljus innehåller en blandning av många olika färger. Ungefär hundra år senare, borrade Thomas Young ett nytt hål i gardinen och visade att två strålar interfererar på ett våglikt sätt. Ljus verkade därmed bestå av en blandning av vågor med olika färger, vilka kunde interferera likt vågor i vatten för att skapa nya vågor av strålning.

Genom att fokusera solljuset till en intensiv brännpunkt kan vi sätta fyr på torrt gräs. Att belysa föremål kan alltså förändra dess tillstånd irreversibelt. På liknande vis kan en puls av ljus som träffar en enstaka atom överföra energi till atomen. Om energin som atomen absorberar är tillräcklig kan atomen skicka ut en elektron i vad som är känt som den fotoelektriska effekten. Albert Einstein fann att den kinetiska energin för den emitterade elektronen berodde på ljusets frekvens och inte dess intensitet – i direkt kontrast till det brinnande gräset. Han upptäckte att ljusets våglika egenskap var otillräcklig för att beskriva det här och föreslog idén om ljusets energikvantum – fotonen. Den här insikten implicerade partikellika egenskaper hos ljuset och är vedertagen som startskottet för kvantåldern.

Med uppfinnandet av lasern på 1960-talet följde möjligheten att skapa intensivt ljus av en enstaka färg vars oscillationer är välkontrollerade, till skillnad från Newtons och Youngs ljus. Det här ljuset kan bli skräddarsytt till precisa förhållanden, så som ultrakorta pulser i tiden och noggrann kontroll av frekvenser, vilket har resulterat i ett stort antal Nobelpris i fysik och kemi, så som Zewails arbete inom *femtokemi*, Hänschs arbete med *frekvenskammar* och Stricklands arbete med *chirped-pulse amplification*.

En av de tidiga upptäckterna som följde laserns uppkomst var utvidgningen av Einsteins fotoelektriska effekt-teori till den så kallade multifoton-jonisations-effekten, där en atom absorberar flertalet fotoner, möjligen av olika färger, medan den frigör en elektron. Den här effekten var ett tydligt bevis för laserns förmåga att producera stabil, koherent och intensiv strålning, och är både grunden och motiveringen för de teoretiska simuleringarna som presenteras i den här avhandlingen. Även elektroner, precis som ljus, innehar både partikel- och våglika egenskaper. Det är därför möjligt att göra interferometriska fotojonisationsexperiment, liknande Youngs experiment, men med de frigjorda elektronerna istället för ljus. Det vackra med de här experimenten är att både information om atomens struktur och dynamik lämnar spår i de frigjorda elektronerna som rika interferensmönster.

För att förstå de här interferometriska jonisationsexperimenten har vi implementerat metoder som kan avläsa strömmen av elektroner medan de frigörs. Genom att avläsa de här ström-

marna har vi studerat både atomär dynamik och jonisationsprocessen. Vi presenterar teoretiska insikter i elektronens fria rörelse i jonisation av ädelgaser och förklarar rollen av elektronens riktning i interferensmönstret. Särskilt har vi studerat experiment var en av de interfererande jonisationsvägarna innehåller fler fotoninteraktioner än den andra och visat hur det påverkar interferensstrukturerna. Vi har även förutspått att interferens i jonisering kan uppstå på grund av att elektronen tar samma väg två gånger – men vid två olika tillfällen – på grund av ett dynamiskt skift av atomens energi i fältet. Slutligen har vi studerat hur atomer kan styras mellan olika bundna energitillstånd, medan elektroner frigörs på grund av pulser av koherent ultraviolett strålning. Genom att finjustera frekvensen i det ultravioletta ljuset till att matcha energiskillnaden mellan två tillstånd kontrollerade vi periodiskt atomens tillstånd, vilket vi mätte i elektronströmmen.

Sammantaget har den här avhandlingen som mål att öka förståelsen för ultrasnabb kontroll av jonisationsexperiment i atomfysik med särskilt fokus på elektroninterferometri tillämpat på attosekund- och fri-elektronlaservetenskap.

List of abbreviations

$\omega/2\omega$ **HHG**	two-color high-order harmonic generation
ATI	Above-threshold ionization
CEP	Carrier-envelope phase
CI	Configuration interaction
CIS	Configuration-interaction singles
ECS	exterior complex scaling
ELI-ALPS	Extreme Light Infrastructure–Attosecond Light Pulse Source
FEL	Free-Electron Laser
FERMI	Free-Electron Laser Radiation for Multidisciplinary Investigations
FLASH	Free-electron LASer in Hamburg
FWHM	Full width at half maximum
GMRES	Generalized minimal residual method
HF	Hartree–Fock
HHG	High-order harmonic generation
iSURFF	Infinite-time surface flux
KFR	Keldysh–Faisal–Reiss theory
LAP	Laser-assisted photoionization
RABBIT	Reconstruction of Attosecond Beating By two-photon Transitions
SPA	Stationary-phase approximation
t+iSURFF	Combination of tSURFF and iSURFF
TDCIS	Time-dependent configuration-interaction singles
TRK	Thomas–Reiche–Kuhn sum rule
tSURFF	Time-dependent surface flux
XUV	Extreme ultraviolet

Introduction

En värld av endast ljus vore en mycket mörk plats.

Cecilia Jarlskog

1 Introduction to nonlinear photoionization processes

This thesis is about atoms interacting with light. When an atom is illuminated with an external light source with photons of energy $\hbar\omega$, larger than the ionization potential of the atom I_p, it may absorb a photon, eject an electron, and the rest of the electrons is left in some bound ionic state. This process is known as *photoionization* and is described by the reaction $A + \gamma \to A^+ + e^-$, where the composite atom–photon pair is transformed into an ion–electron pair.

1.1 Regimes of photoionization

The kinetic energy spectrum of the photoelectron is frequently used to gain information about the photoionization event. If the atom is illuminated by a weak field, an electron may be ejected with a kinetic energy equal to

$$E_k = \hbar\omega - I_p, \tag{1.1}$$

which enforces energy conservation of the one-photon ionization process. Since a pulse of electromagnetic radiation implies a range of photon energies, the resulting photoelectron will distribute over a range of kinetic energies. This is the famous photoelectric effect, described in e.g. Ref. [1]. The rate of the one-photon ionization process depends on the intensity I of the field and on the one-photon *cross section* σ_1, see e.g. Ref. [2, 3],

$$\Gamma_1 \sim \sigma_1 I, \tag{1.2}$$

where the cross section depends on the square of the transition matrix elements, $\sigma_1 \sim |D|^2$, between the bound and continuum states. The continuum states can be expanded in partial waves with specific orbital angular momentum and magnetic quantum numbers, ℓ and m, respectively [3].

In Fig. 1, ionization by absorption of a photon from a field with linear polarization is depicted. The multiple continua coupled to the atom, characterized by the orbital angular momenta of the photoelectron, are shown. The magnetic quantum number m is conserved since the field is polarized linearly, and we therefore omit it. The continuous energy states of the photoelectron are infinitely degenerate, because there exists an infinite number of angular momenta of a photoelectron with a given kinetic energy. We will however in the following of this thesis restrict the discussion to continua that are accessible by the *dipole selection rules* that derive from the dipole approximation elaborated in Sec. 3.2. Since the bound state of a closed-shell atom has a defined ℓ_0 and m_0, as discussed in Sec. 2.1 within the Hartree–Fock approximation (HF), it means that only a few of the matrix elements of the one-photon cross section in Eq. (1.2) are nonzero.

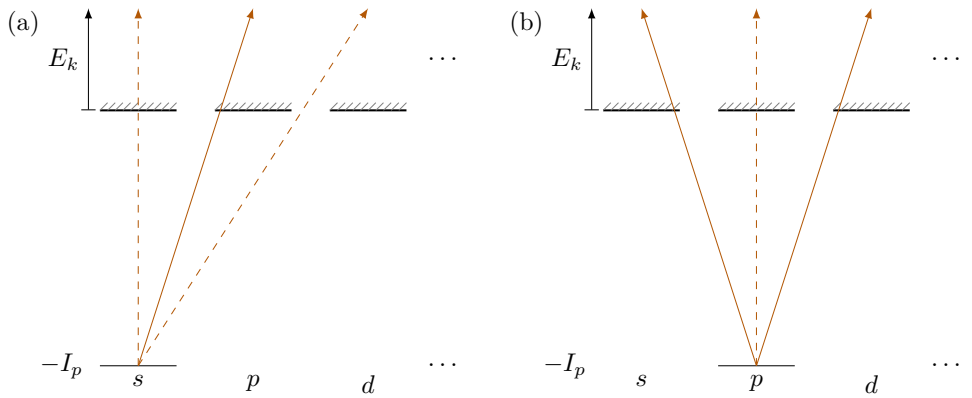

Figure 1: Photoionization into multiple degenerate continua characterized by orbital angular momentum ℓ in spectroscopic notation. The dipole-allowed transitions are emphasized with solid lines, and the others are drawn with dashed lines. (a) In ionization from s, only the transition to p is allowed in a dipole transition. (b) In ionization from p, only the transitions to s and to d are allowed in a dipole transition.

As expected from the photoelectric effect, the cross section is zero if the energy of the photon is smaller than the ionization potential, $\hbar\omega < I_p$. Ionization of atoms by photons of energy smaller than the ionization potential can however occur by absorption of multiple photons. This *multiphoton ionization* effect was first observed experimentally in the 1960's in connection to the invention of the laser [4, 5]. In line with the photoelectric effect, it was assumed that the kinetic energy of the photoelectron would be given by

$$E_k = n\hbar\omega - I_p, \tag{1.3}$$

and that the ionization rate from the n-photon absorption process, calculated by including higher-order terms of the perturbation expansion and therefore expressed as $\Gamma_n \sim \sigma_n I^n$ [6], where σ_n is the nth-order photoionization cross section, would be reduced for each absorbed photon. The intensity therefore needs to be high in order to observe this effect, especially for a low-frequency field, which would require absorption of many photons. For example, ionization of a helium atom exposed to an infrared field with a photon energy of about $\hbar\omega = 1.55\,\mathrm{eV}$ requires the absorption of 17 photons.

The extrapolation of the photoelectric effect in Eq. (1.3) was not completely satisfactory however. In a six-photon ionization experiment of xenon, a peak in the photoelectron spectrum corresponding to absorption of seven photons was observed [7]. That more photons than the minimal number required to overcome the ionization threshold had been absorbed meant that the electron had absorbed a photon in the continuum. This was termed *above-threshold ionization* [8] (ATI) and is discussed in more detail in Sec. 9. The absorption of a photon in the continuum caused confusion since a free electron cannot absorb photons and simultaneously conserve both the total energy and momentum, but it was later understood that the electron absorbs the photon in the Coulomb field of the ion

that serves as a momentum reservoir [6]. A schematic of the multiphoton ionization process in Ref. [7] is shown in Fig. 2. Multiphoton ionization is a central concept of attosecond physics, and core subject in this thesis.

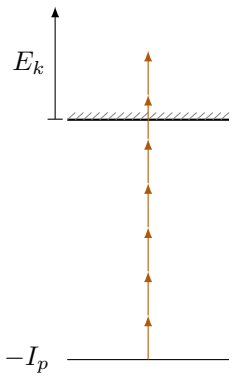

Figure 2: Schematic of multiphoton ionization of xenon atoms as in Ref. [7] that results in a peak corresponding to absorption of six photons and an ATI peak corresponding to absorption of an additional photon in the continuum.

1.2 What is a *strong* field?

To distinguish the different regimes of photoionization, we often specify the intensity of the light together with the central frequency of the light. There exist numerous measures of the strength of a field, and we will here introduce the ones that are relevant for the work of this thesis. We loosely define a *strong* field as an environment in which the electric field of the light is comparable to that of the atomic potential such that the electron dynamics is significantly distorted by the field. But the term is ambiguous and may refer to very different experimental conditions. On the one hand, there are table-top lasers like the Terawatt Laser in Lund that packs energies of up to 2 J into pulses of tens of femtoseconds before compression and delivers pulses of a relativistic intensity of the order $10^{19}\,\mathrm{W/cm^2}$ [9], an intensity much larger than the fields of intensities between 10^{11} – $10^{14}\,\mathrm{W/cm^2}$ that we consider in this thesis. The high power is achieved by means of chirped-pulse amplification [10], which lead to the 2018 Nobel Prize in Physics to Strickland and Mourou. There are also larger facilities, like the Extreme Light Infrastructure–Attosecond Light Pulse Source (ELI-ALPS) facility, where the high-field laser delivers pulses with an effect up to PW [11].

Another strong radiation source is the free-electron lasers (FEL), see e.g. Ref. [12] for a review, like the Free-Electron Laser Radiation for Multidisciplinary Investigations [13] (FERMI) or the Free-electron LASer in Hamburg [14] (FLASH). The extreme-ultraviolet (XUV) or X-ray pulses produced by these facilities are *strong* in a different regard. While the intensities may be large, typically of the order 10^{13} – $10^{14}\,\mathrm{W/cm^2}$, the high frequency of these fields make the distortions of the atomic potential by the light field small. Still,

FEL light produced at FLASH has been used to 21-fold ionize xenon atoms [15] – clearly a tremendous impact on the atomic target.

The ponderomotive energy of the photoelectron

A free classical electron exposed to a linearly polarized electric field undergoes a drifting, oscillatory, motion along the polarization direction.[1] This motion, which in the rest frame of the electron has an amplitude of

$$\alpha = \frac{qE_0}{m_e\omega^2}, \tag{1.4}$$

is known as the free electron's quiver motion and leads to an increased kinetic energy, averaged over an optical cycle, termed the *ponderomotive energy*. The ponderomotive energy is given by

$$U_p = \frac{q^2E_0^2}{4m_e\omega^2}, \tag{1.5}$$

where q is the charge of the electron and E_0 is the peak electric field. In order to exist in the field, the electron needs a kinetic energy at least equal to the ponderomotive energy. In a photoionization experiment, this means that the ionization threshold is shifted up such that the photoelectron is measured with a kinetic energy lower than that given in Eq. (1.3) [16], see Fig. 3b,

$$E_k = n\hbar\omega - I_p - U_p. \tag{1.6}$$

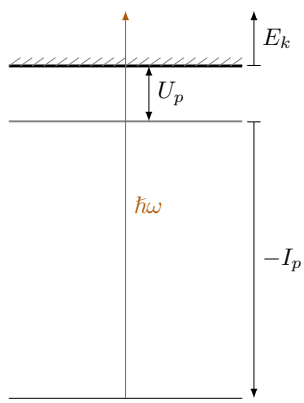

Figure 3: The shift of the ionization threshold due to the ponderomotive energy of an electron in an oscillating field.

[1] For very intense fields where the magnetic field is not negligible, the classical electron undergoes a figure-eight motion, in the plane spanned by the polarization direction and the propagation direction of the electric field, in the rest frame of the electron.

The Keldysh parameter

As we already alluded to, the question if the field is strong or not is a question that must be answered in relation to the target atomic system. This can be quantified with the help of the Keldysh parameter that distinguishes between two regimes of photoionization, *tunneling* and multiphoton ionization [17]. It provides a measure of the intensity of the electromagnetic field relative to the bound states of the atom that is targeted, and is given by

$$\gamma = \sqrt{\frac{I_p}{2U_p}}. \tag{1.7}$$

The Keldysh parameter indicates whether the situation is dominated by the bounded motion of the electron or the presence of the field and distinguishes the tunneling regime ($\gamma \ll 1$), and the multiphoton regime ($\gamma \gg 1$). These two regimes are illustrated in Fig. 4, where it is seen that in the tunneling regime the Coulombic barrier is suppressed to the point that the electron may tunnel through. In the multiphoton regime on the other hand, ionization is mainly due to absorption of multiple photons. However, while it is true that tunneling is the predominant process when $\gamma \ll 1$, Keldysh's theory does not exclude tunneling when $\gamma \gg 1$; the two processes co-exist [18]. There is further the intermediate regime, when $\gamma \approx 1$, which is a common regime in the generation of high-order harmonics [19–21] (HHG).

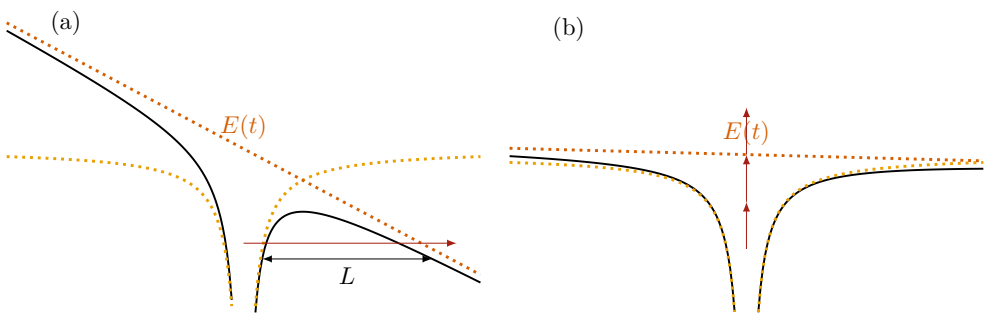

Figure 4: The two ionization regimes of the Keldysh parameter: (a) The tunneling regime, and (b) the multiphoton regime. In (a) the barrier is suppressed so that the electron may tunnel through, whereas in (b) the barrier is rather unperturbed by the field, and ionization occurs mainly by absorption of multiple photons.

From a classical viewpoint, the suppressed barrier that the electron must tunnel through is of length

$$L \propto \frac{I_p}{qE_0}, \tag{1.8}$$

where E_0 is the peak electric field, while the velocity of the tunneling electron is given by

$$v = \sqrt{\frac{I_p}{2m_e}}. \tag{1.9}$$

The time it takes to tunnel is hence

$$\tau = \frac{\sqrt{2m_e I_p}}{qE_0}. \tag{1.10}$$

When multiplying this time with the angular frequency of the field, we obtain the Keldysh parameter,

$$\gamma = \frac{\omega\sqrt{2m_e I_p}}{qE_0} = \sqrt{\frac{I_p}{2U_p}}. \tag{1.11}$$

If the frequency is comparatively low, the electron has plenty of time to tunnel through the distorted barrier.

Another interpretation of the Keldysh parameter involves the power broadening[2] of the atomic levels when exposed to a strong electric field with photon energy $\hbar\omega$ [23]. The broadening is of the order $|q\mathbf{r}\cdot\mathbf{E}| \approx qa_0E_0$, where a_0 is the Bohr radius, which for the hydrogen atom can be expressed as $a_0 = \hbar/\sqrt{2m_eI_p}$. Compared to the photon energy, this gives

$$\frac{\hbar\omega}{q\mathbf{r}\cdot\mathbf{E}} \approx \frac{\hbar\omega}{qa_0E_0} = \frac{\omega\sqrt{2m_eI_p}}{qE_0} = \sqrt{\frac{I_p}{2U_p}}. \tag{1.12}$$

For very strong fields, at small γ, the energy levels are therefore broadened by an amount of the order of the photon energy.

Rabi oscillations

For resonant fields with a photon energy equal to the energy spacing between two bound atomic states, periodic modulation of population between the two states occurs. We may model this as a two-level system in presence of an external monochromatic field, which couples the two levels. This field-driven periodic population transfer between the states in a two-level system is known as Rabi oscillations [24, 25]. The field is able to invert the atomic population and therefore control matter to a very exotic state, largely away from thermal equilibrium, and its description requires treatment beyond perturbation theory. The Hamiltonian that describes this situation is given by

$$\hat{H}(t) = \frac{1}{2}\hbar\omega_{ba}\hat{\sigma}_z + \hbar\Omega\cos(\omega t)\hat{\sigma}_x, \tag{1.13}$$

where $\hat{\sigma}_{x,z}$ are the x- and z-Pauli matrices, and Ω is known as the Rabi frequency defined from

$$\Omega = -\frac{q}{\hbar}\langle b|\hat{\mathbf{r}}\cdot\mathbf{E}_0|a\rangle, \tag{1.14}$$

[2]The power broadening of order $|q\mathbf{r}\cdot\mathbf{E}|$ happens due to absorption saturation at resonance, cf. Ref. [22].

and $\hbar\omega_{ba} = \varepsilon_b - \varepsilon_a$ is the energy difference between the two states. The solution of the time-dependent Schrödinger equation can be obtained by expansion onto the field-free eigenstates with time-dependent amplitudes due to the interaction with the field,

$$|\Psi(t)\rangle = a(t)\mathrm{e}^{-\mathrm{i}\omega_a t}|a\rangle + b(t)\mathrm{e}^{-\mathrm{i}\omega_b t}|b\rangle, \tag{1.15}$$

where the amplitudes $a(t)$ and $b(t)$ describes the modulation between the two states. If the system is initially in its ground state, $a(0) = 1$ and $b(0) = 0$, we may solve for the amplitudes within the rotating-wave approximation [25]. This yields the coefficients

$$a(t) = \left[\cos\frac{Wt}{2} - \mathrm{i}\frac{\Delta\omega}{W}\sin\frac{Wt}{2}\right]\exp(\mathrm{i}\Delta\omega t/2), \tag{1.16a}$$

$$b(t) = -\mathrm{i}\frac{\Omega}{W}\sin\frac{Wt}{2}\exp(-\mathrm{i}\Delta\omega t/2), \tag{1.16b}$$

where $\Delta\omega = \omega - \omega_{ba}$ is the detuning of the field from the resonance, and $W = \sqrt{\Omega^2 + \Delta\omega^2}$ is defined as the generalized Rabi frequency. The dependence on the generalized Rabi frequency means that the frequency of these oscillations increases, and further also the probability of finding the atom in the excited state decreases, with detuning. We discuss ionization from a Rabi-cycling atom in more detail in Sec. 10.1. For now, we conclude that the ambiguous term *strong* is not trivially defined, but requires careful analysis of the field's properties in relation to the atomic target.

1.3 Scope of this work

The outline of this thesis is as follows. In the second part, *Background and Theory*, we give a general theoretical review of the topics that form this thesis. We start by a description of how the atom is structured in Sec. 2 by introducing the Hartree–Fock approximation and its extension to the configuration-interaction singles approximation. We continue with a description of how radiation externally enters in Sec. 3, and present a brief discussion on the choice of gauge in truncated configuration spaces. Light–matter interactions are then discussed in Sec. 4, with a presentation of sum rules, and in Sec. 5, where the time-dependent configuration-interaction singles approximation is introduced. The theoretical chapter is concluded by a description of photoionization dynamics in Sec. 6, mainly in the form of surface-flux techniques.

In the third part, *Applications in attosecond physics and free-electron laser science*, the theoretical work published in Paper I– Paper VI is briefly presented and put into context. Laser-assisted photoionization is first discussed in Sec. 7. We touch on three different regimes: (i) a single weak XUV field under dressing of a weak IR field, (ii) a single weak XUV field under dressing of a strong IR field, and (iii) multiple weak XUV fields under dressing of a weak IR field. Several interferometric photoelectron schemes are discussed and compared

in Sec. 8. We further describe above-threshold ionization in Sec. 9 and Rabi dynamics in Sec. 10.

Finally, in *Publications*, the research papers are reprinted.

Background and theory

2 Atomic structure of many-electron systems

The dynamics of any quantum process that does not include relativistic effects is ruled by the time-dependent Schrödinger equation (TDSE)

$$\mathrm{i}\hbar\frac{\partial}{\partial t}\psi(t) = \hat{H}(t)\psi(t), \tag{2.1}$$

where $\psi(t)$ is the time-dependent quantum wavefunction of the system and $\hat{H}$ is the Hamiltonian operator, which determines the dynamics involved. The specific form of the Hamiltonian $\hat{H}(t)$ hence rules the interactions that may take place in the evolution of the quantum system. Throughout this thesis, we deal with light interacting with atomic systems. This choice of quantum system is reflected in the Hamiltonian, which will have one *atomic* part and one *interaction* part in the semi-classical description of light–matter interactions.

In this chapter, we summarize the background and theory of the papers that comprise this thesis. In Sec. 2 we begin with describing the structure of a many-electron atom and the treatment of the interelectronic Coulombic repulsion. We do so by first introducing the N-body atomic Hamiltonian and the Hartree–Fock approximation, which reduces the complexity of the problem to N single-electron equations affected by an central-field potential. We then let the atom be subject to an external electric field in Sec. 3 and discuss the form of interactions that we allow in this description. We restrict the treatment to the dipole approximation, where the electric field is uniform in space and magnetic effects are neglected.

With the description of an atom in an external field, light–matter processes can be investigated. We start this discussion in Sec. 4 where we discuss atomic sum rules and calculate energy shifts using these. We then introduce the time-dependent configuration-interaction singles approximation in Sec. 5, which is the theoretical framework that we use in this thesis to describe light–matter processes. Finally, in Sec. 6, we describe photoionization dynamics with emphasis on surface-flux methodologies to record photoelectron spectra.

The atomic part of the non-relativistic Hamiltonian will be denoted by $\hat{H}^{(\mathrm{atom})}$ and is given by

$$\hat{H}^{(\mathrm{atom})} = \sum_{n=1}^{N}\left(\frac{\hat{\mathbf{p}}_n^2}{2m_\mathrm{e}} - \frac{q^2}{4\pi\epsilon_0}\frac{Z}{|\mathbf{r}_n|}\right) + \frac{q^2}{4\pi\epsilon_0}\sum_{n>m=1}^{N}\frac{1}{|\mathbf{r}_n - \mathbf{r}_m|}, \tag{2.2}$$

where $\hat{\mathbf{p}}_n = -\mathrm{i}\hbar\nabla_n$ is the canonical momentum operator of the electron with label n and $\mathbf{r}_n$ is its position. The first sum describes the kinetic and potential energy of each electron under influence of the attractive nucleus with charge $Z > 0$, and the second sum describes the potential energy due to the two-electron electrostatic repulsion among the

electrons with charge $q = -e$ and mass m_e. We do not consider any contribution due to the nuclear degrees of freedom, or any magnetic interactions among the electrons. In the following of this thesis we will use atomic units[3] unless otherwise specified.

2.1 The Hartree–Fock approximation

The two-electron repulsion terms in Eq. (2.2) make the brute-force numerical solution of the problem intractable for any but the smallest systems since the separability of the electron coordinates is lost. As an approximate description, which will be used as a starting point for the method of configuration interaction (CI), which is introduced in Sec. 2.2, the two-electron terms are replaced by an average field where the electrons feel an effective potential. This effective potential is built up by summing over all electrons, and that acts the same way on all electrons. If the average field is further taken to be spherically symmetric, the description is known as the *central-field model*, see for instance Refs. [26, 27]. To arrive at this model, we may write the N-electron Hamiltonian in Eq. (2.2) by separating it into an independent-particle Hamiltonian and a correction term,

$$\hat{H}^{(\mathrm{atom})} = \hat{H}_0 + \hat{V}, \tag{2.3}$$

where $\hat{H}_0$ is now a sum over one-electron operators,

$$\hat{H}_0 = \sum_{n=1}^{N} \hat{h}_{0,n}, \tag{2.4}$$

which in turn are separated as

$$\hat{h}_{0,n} = \hat{h}_0 + \hat{u}_n(r_n). \tag{2.5}$$

The one-electron Hamiltonian $\hat{h}_0 = \frac{\hat{\mathbf{p}}^2}{2} - \frac{Z}{|\mathbf{r}|}$ is the hydrogenic Hamiltonian, and the effective potential $\hat{u}_n(r_n)$ accounts for the central field in which the nth electron moves. The average many-body effects are then contained in the approximate Hamiltonian $\hat{H}_0$, and the potential $\hat{V}$ accounts for the effects beyond the single-particle description,

$$\hat{V} = -\sum_{n} \hat{u}_n(r_n) + \sum_{n>m=1}^{N} \frac{1}{|\mathbf{r}_n - \mathbf{r}_m|}, \tag{2.6}$$

which we refer to electron-correlation effects. Which independent-particle central-field potential $\hat{u}_n(r_n)$ best captures the many-electron effects described in the full N-body Hamiltonian? That the electrons move independently and in a spherically symmetric potential

[3] Atomic units are used to simplify calculations in atomic physics. In atomic units the following constants equal unity: $\hbar = -q = a_0 = m_e = 4\pi\varepsilon_0 = 1$.

are two strong assumptions that are valid for the shell structure of the atom [26]. A solution to the independent-particle model is given by a *Hartree product* of the individual spin orbitals[4],

$$\Phi_{\boldsymbol{\alpha}}(\mathbf{r}) = \varphi_a(r_1)\varphi_b(r_2)\cdots\varphi_n(r_N), \tag{2.7}$$

where $a, b, \ldots$ represent the relevant quantum numbers for each individual one-electron orbital. Each of the individual orbitals satisfies the one-particle time-independent Schrödinger equation and corresponds to an eigenstate with energy $\varepsilon_{0,i}$. The product state is in turn an eigenstate to the mean-field Hamiltonian with corresponding energy $E_0 = \sum_{i=1}^{N} \varepsilon_{0,i}$. Since the mean-field Hamiltonian is invariant to any permutation of the product state, for example

$$\Phi'_{\boldsymbol{\alpha}}(\mathbf{r}) = \varphi_a(r_2)\varphi_b(r_1)\cdots\varphi_n(r_N), \tag{2.8}$$

the corresponding energy is the same. However, Fock found that the product-state wavefunctions alone violate the Pauli exclusion principle [27]. To ensure that the wavefunction is antisymmetric, and therefore respects the Pauli exclusion principle, we form a determinantal wavefunction – a *Slater determinant*:

$$\Phi_0(\mathbf{r}) = \frac{1}{\sqrt{N!}} \begin{vmatrix} \varphi_a(r_1) & \varphi_a(r_2) & \cdots & \varphi_a(r_N) \\ \varphi_b(r_1) & \varphi_b(r_2) & \cdots & \varphi_b(r_N) \\ \vdots & & & \\ \varphi_n(r_1) & \varphi_n(r_2) & \cdots & \varphi_n(r_N) \end{vmatrix}. \tag{2.9}$$

We adopt the notation used in Ref. [26], where a Slater determinant is denoted $|\Phi_0\rangle = |\{abc...n\}\rangle$. The antisymmetric property of the Slater determinant is seen from $|\{abc...n\}\rangle = -|\{bac...n\}\rangle$. The antisymmetry principle ensures that the electrons are indistinguishable. Any single-electron spin orbital present in Φ_0 is called an *occupied* orbital, and the other are called *virtual* orbitals. Occupied orbitals are denoted by indices $a, b, c, \ldots$, and virtual orbitals are denoted by indices $p, q, r, \ldots$. If an electron in an orbital a, occupied in the determinant, is promoted into a virtual orbital r, we denote this by $\Phi_a^p = \{pbc...n\}$. If an orbital may be either occupied or virtual, we denote this by indices $i, j, k, \ldots$. The labels $m, n, \ldots$ are reserved to index particles in position representation.

The Hartree–Fock equations are found from the variational principle, by minimizing the expectation value

$$\langle E\rangle = \langle\Phi_0|\hat{H}|\Phi_0\rangle, \tag{2.10}$$

with the explicit ansatz that the N-body system can be described by a single Slater determinant. Adding a small admixture of a singly-excited state,

$$|\Phi_0\rangle \to |\Phi_0\rangle + \eta|\Phi_a^p\rangle, \tag{2.11}$$

[4]The Pauli exclusion principle for fermions such as electrons, implies that all individual orbitals, which are referred to as spin orbitals $|\varphi_{i_\sigma}\rangle$, must be unique. We will omit writing the spin σ in the following of this section, with exception for Eq. (2.16).

would change the expectation value,

$$\langle E\rangle \rightarrow \langle E\rangle + \eta\left(\langle\Phi_a^p|\hat{H}|\Phi_0\rangle + \langle\Phi_0|\hat{H}|\Phi_a^p\rangle\right). \tag{2.12}$$

The *optimal* Slater determinant is therefore found when the expectation value in Eq. (2.10) is zero,

$$\langle\Phi_a^p|\hat{H}|\Phi_0\rangle = 0, \tag{2.13}$$

which is known as Brillouin's theorem, see e.g. Ref. [26].

In its general form, there are no restrictions on the solutions to Eq. (2.10), other than that the wavefunctions have to be represented by single Slater determinants. Since we however only study closed-shell atoms, we require the wavefunctions to correspond to a central-field potential as done in Eq. (2.5). To allow only central-field potentials is known as the *restricted* Hartree–Fock equations contrary to the *unrestricted* Hartree–Fock equations. We may therefore expand a spatial wavefunction into a radial part and an angular part,

$$\Phi_0(r,\theta,\varphi) = \frac{P(r)}{r}Y_{\ell m}(\theta,\varphi). \tag{2.14}$$

The angular part can be solved analytically by angular-momentum algebra, see e.g. Ref. [28], and we are left with the radial part only. This leads to solving a coupled set of radial Schrödinger equations for a single electron in a central potential, with an external potential that handles the coupling among the electrons, see Ref. [26],

$$\sum_a^{\text{occ}}\left[-\frac{1}{2}\frac{\mathrm{d}^2}{\mathrm{d}r^2} + \frac{\ell_a(\ell_a+1)}{2r^2} - \frac{Z}{r} + \hat{u}^{(\text{HF})}\right]P_a(r) = \sum_a^{\text{occ}}\varepsilon_a P_a(r). \tag{2.15}$$

The analysis that follows will to a large extent be expressed in the language of *second quantization*, where the Hamiltonian is composed of one- and two-particle operators while the atom is composed of N particles. The main reason for employing this formalism is that any operator can be expressed as basic excitations, and that the antisymmetric criterion is automatically satisfied. The determinants that represent singly-excited states are constructed in second quantization as

$$|\Phi_{a_\sigma}^{p_\sigma}\rangle = \hat{a}_{p_\sigma}^\dagger\hat{a}_{a_\sigma}|\Phi_0\rangle, \tag{2.16}$$

where $\hat{a}_{p_\sigma}^\dagger$ creates an electron with spin σ in the virtual spatial orbital φ_p, and $\hat{a}_{a_\sigma}$ annihilates an electron with spin σ in the occupied spatial orbital φ_a. In order to not overcrowd the notation, the symbol p and a imply also σ, unless otherwise stated. Any one- and two-particle operators can be written on the form

$$\hat{F} = \sum_{n=1}^N \hat{f}_n = \sum_{ij}\langle i|\hat{f}|j\rangle\ \hat{a}_i^\dagger\hat{a}_j, \tag{2.17a}$$

$$\hat{G} = \sum_{n<m}^N \hat{g}_{n,m} = \frac{1}{2}\sum_{ijkl}\langle ij|\hat{g}|kl\rangle\ \hat{a}_i^\dagger\hat{a}_j^\dagger\hat{a}_l\hat{a}_k, \tag{2.17b}$$

where sums over n and m run over all particle and the sums over i, j, k and l run over the full Fock space (occupied and virtual). The creation and annihilation operators thus act on the spatial orbitals and create and annihilate a particle in the (spatial) orbital i, j, k or l, respectively. The mean-field Hamiltonian $\hat{H}_0$ and the correction term $\hat{V}$ can hence be expressed as

$$\hat{H}_0^{(\mathrm{HF})} = \sum_n (\hat{h}_0 + \hat{u}_n^{(\mathrm{HF})}) = \sum_{ij} \langle i|\hat{h}^{(\mathrm{HF})}|j\rangle \; \hat{a}_i^\dagger \hat{a}_j, \tag{2.18a}$$

$$\hat{V} = \sum_{n<m}^{N} r_{nm}^{-1} - \sum_{n=1}^{N} \hat{u}_n^{(\mathrm{HF})} \tag{2.18b}$$

$$= \frac{1}{2} \sum_{ijkl} \langle ij|r_{12}^{-1}|kl\rangle \; \hat{a}_i^\dagger \hat{a}_j^\dagger \hat{a}_l \hat{a}_k - \sum_{ij} \langle i|\hat{u}^{(\mathrm{HF})}|j\rangle \; \hat{a}_i^\dagger \hat{a}_j, \tag{2.18c}$$

where $r_{12}^{-1} = 1/|\mathbf{r}_1 - \mathbf{r}_2|$ is the distance between the two electrons. In particular, the Hartree–Fock potential is given by

$$\langle i|\hat{u}^{(\mathrm{HF})}|j\rangle = \sum_c \left(\langle ci|r_{12}^{-1}|cj\rangle - \langle ci|r_{12}^{-1}|jc\rangle \right). \tag{2.19}$$

The second term, the exchange term, is nonlocal since each orbital is affected by the influence of the other orbitals evaluated at a different radial distance.

Since the matrix elements of the Hamiltonian can be decomposed into matrix elements of one- and two-body operators, we here present them. The matrix elements of the one- and two-particle operators between the reference Slater determinant and singly-excited states can be found by using the anticommutation relations of the creation and annihilation operators, found in e.g. Ref. [26], and are given by

$$\langle \Phi_0|\hat{F}|\Phi_0\rangle = \sum_a \langle a|\hat{f}|a\rangle, \tag{2.20a}$$

$$\langle \Phi_a^p|\hat{F}|\Phi_0\rangle = \langle p|\hat{f}|a\rangle, \tag{2.20b}$$

$$\langle \Phi_a^p|\hat{F}|\Phi_b^q\rangle = \sum_c \langle c|\hat{f}|c\rangle \delta_{pq}\delta_{ab} + \langle p|\hat{f}|q\rangle \delta_{ab} - \langle b|\hat{f}|a\rangle \delta_{pq}, \tag{2.20c}$$

$$\langle \Phi_0|\hat{G}|\Phi_0\rangle = \frac{1}{2} \sum_{ab} \left(\langle ab|\hat{g}|ba\rangle - \langle ab|\hat{g}|ab\rangle \right), \tag{2.20d}$$

$$\langle \Phi_a^p|\hat{G}|\Phi_0\rangle = \sum_b \left(\langle pb|\hat{g}|ab\rangle - \langle pb|\hat{g}|ba\rangle \right), \tag{2.20e}$$

$$\langle \Phi_a^p|\hat{G}|\Phi_b^q\rangle = \sum_c \left(\langle cp|\hat{g}|cq\rangle - \langle cp|\hat{g}|qc\rangle \right) \delta_{ab} - \langle bp|\hat{g}|aq\rangle + \langle bp|\hat{g}|qa\rangle. \tag{2.20f}$$

A product sequence of operator in second quantization can conveniently be put on *normal form*, which we denote by $\{\ldots\}$. This means that the sequence of operators should be permuted so that all core-creation operators $\hat{a}_a^\dagger$ and virtual-annihilation operators $\hat{a}_p$ appear to the right. An operator product on this form which acts on the vacuum state will then return numerical zero. There is an accumulated phase factor of -1 for each permutation according to the anticommutation relations [3]. The mean-field Hamiltonian can then be written as

$$\hat{H}_0^{(\mathrm{HF})} = \sum_{ij} \hat{a}_i^\dagger \hat{a}_j \langle i|\hat{h}^{(\mathrm{HF})}|j\rangle = \sum_c \varepsilon_c + \sum_i \{\hat{a}_i^\dagger \hat{a}_i\}\varepsilon_i, \tag{2.21}$$

and the correction term $\hat{V}$ can be written as, cf. Ref. [3],

$$\hat{V} = \hat{V}_0 + \hat{V}_2, \tag{2.22a}$$

$$\hat{V}_0 = -\sum_c \langle c|\hat{u}^{(\mathrm{HF})}|c\rangle + \frac{1}{2}\sum_{cd}\left(\langle cd|r_{12}^{-1}|cd\rangle - \langle cd|r_{12}^{-1}|dc\rangle\right), \tag{2.22b}$$

$$\hat{V}_2 = \frac{1}{2}\sum_{ijkl}\{\hat{a}_i^\dagger \hat{a}_j^\dagger \hat{a}_l \hat{a}_k\}\langle ij|r_{12}^{-1}|kl\rangle, \tag{2.22c}$$

This shows that the correction beyond mean-field contributions can be decomposed into a zero-body operator $\hat{V}_0$ and a two-body operator $\hat{V}_2$. For an arbitrary potential, there may also be a one-particle contribution of the form

$$\hat{V}_1 = \sum_{ij}\{\hat{a}_i^\dagger \hat{a}_j\}\langle i|\hat{v}|j\rangle; \tag{2.23}$$

however this vanishes when $\hat{u}_n$ is chosen the Hartree–Fock potential $\hat{u}_n^{(\mathrm{HF})}$. In the case of an external potential applied to the atom, the excitations will be treated as one-body interactions, as discussed in Sec. 3. Furthermore, since the second term in $\hat{V}_0$ is half the Hartree–Fock potential, we identify $\hat{V}_0$ as the first-order energy correction in Hartree–Fock,

$$\hat{V}_0 = E_1^{(\mathrm{HF})} = -\frac{1}{2}\sum_c \langle c|\hat{u}^{(\mathrm{HF})}|c\rangle, \tag{2.24}$$

and this term will shift the energy equally for all determinantal states. Since only relative energy shifts are physical, this joint energy shift will not affect any physical reaction. Regarding the two-body operator $\hat{V}_2$, the indices will run independently over all core and virtual orbitals. However, we will only be interested in certain combinations where i and j belong to different subspaces, and likewise k and l belong to different subspaces, such that one particle and one hole will enter the interaction and one particle and one hole will leave the interaction. The only terms that we will need to consider are therefore explicitly given

by

$$\hat{V}_2 = \frac{1}{2}\sum_{crsd} \hat{a}_r^\dagger \hat{a}_d \hat{a}_c^\dagger \hat{a}_s \Big(\langle cr|r_{12}^{-1}|sd\rangle + \langle rc|r_{12}^{-1}|ds\rangle - \langle cr|r_{12}^{-1}|ds\rangle - \langle rc|r_{12}^{-1}|sd\rangle \Big) \tag{2.25a}$$

$$= \sum_{crsd} \hat{a}_r^\dagger \hat{a}_d \hat{a}_c^\dagger \hat{a}_s \Big(\langle cr|r_{12}^{-1}|sd\rangle - \langle cr|r_{12}^{-1}|ds\rangle \Big), \tag{2.25b}$$

These contributions are interpreted as the direct and the exchange Coulomb interactions and are shown as Goldstone diagrams in Fig. 5.

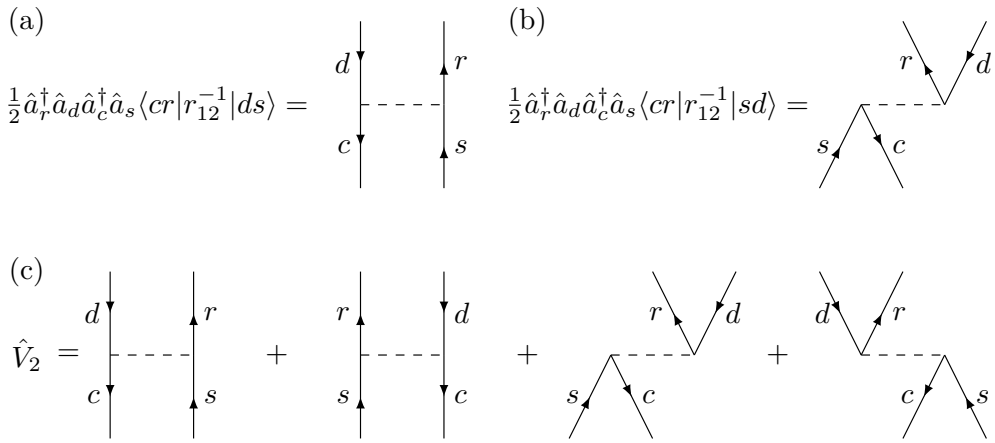

Figure 5: Goldstone diagrams of the (a) direct and (b) exchange matrix elements of the $\hat{V}_2$ potential in Eq. (2.25). (c) The $\hat{V}_2$ potential expressed as Goldstone diagrams. The matrix elements that do not give a contribution are omitted.

2.2 Configuration interaction

The connection between the central-field model and the N-body Hamiltonian is formed by separating the electron–electron effects from the one-electron Hamiltonian,

$$\hat{H} = \hat{H}_0 + \hat{V}, \tag{2.26}$$

with the many-electron effects beyond the mean-field description contained in $\hat{V}$, which implies that the two-body interactions in Eq. (2.25) must be taken into account to some level of approximation. If the central field contains most of the electron–electron interactions, the treatment of $\hat{V}$ can effectively be done with perturbation theory [26]. Alternatively, many-body effects beyond that of the Hartree–Fock model can be treated variationally. One variational procedure is the method of configuration interaction [29], which will be discussed in the following.

The determinant $|\Phi_0\rangle$, found by solving the restricted Hartree–Fock equations, Eq. (2.15), will serve as a starting point. Since all other possible determinants can be expressed as excitations from the Hartree–Fock determinant, any N-body determinant can be expanded onto the linear combination

$$|\Phi\rangle = \alpha_0|\Phi_0\rangle + \sum_{a,p} \alpha_a^p|\Phi_a^p\rangle + \sum_{ab,pq} \alpha_{ab}^{pq}|\Phi_{ab}^{pq}\rangle + \ldots, \tag{2.27}$$

where the coefficients α_i are found variationally and $|\Phi_a^p\rangle$ are constructed using Eq. (2.16). For an N-electron system composed out of K (core and virtual) orbitals, this will yield $\binom{K}{N}$ configurations to account for. Hence, even for small systems, the number of terms in the CI expansion is enormous. Therefore, the CI expansion is in practice truncated at some point such that the main part of the electronic correlation effects is still accounted for while ensuring that the computational basis is small enough. There are several ways the CI expansion can be truncated. It is natural to directly truncate the number of virtual orbitals in the calculation, but this would require an optimization of the virtual states to represent physical excited states. If the expansion however is truncated at the level of single excitations, it is known as configuration-interaction singles (CIS),

$$|\Phi\rangle = \alpha_0|\Phi_0\rangle + \sum_{a,p} \alpha_a^p|\Phi_a^p\rangle. \tag{2.28}$$

Truncation of the CI expansion will however have problems of size inconsistency. This means that the energy of including two noninteracting particles is not twice the energy of one of them [29]. When we will extend CIS to a time-dependent theory in Sec. 5, size inconsistency will also enter in the sense that the field-polarization effects are accounted for differently for the Hartree–Fock determinant and the singly-excited states. We will return to the effect of truncating the configuration space when including a nonlocal potential such as the exchange potential in Hartree–Fock, the second term of Eq. (2.19), in Sec. 4.1 where we discuss the Thomas–Reiche–Kuhn (TRK) sum rule, see e.g. Ref. [3, 30]. In Fig. 6, the particle–hole formalism used to describe the CIS basis is exemplified.

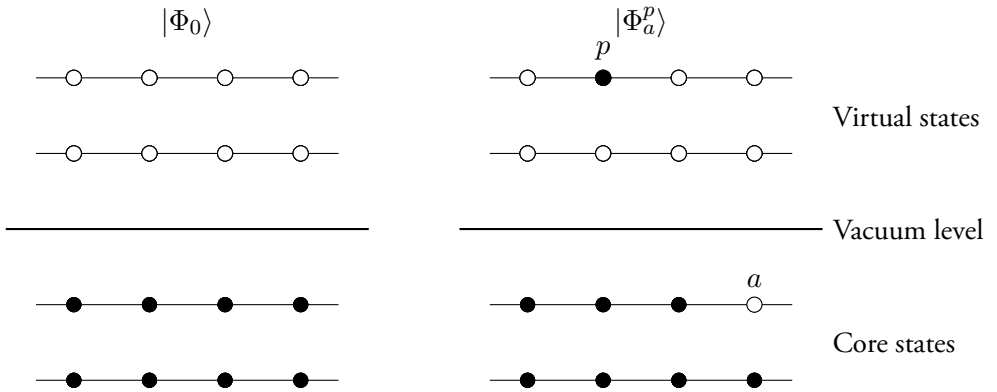

Figure 6: Illustration of the creation of a particle and a hole from the ground state given by the Hartree–Fock determinant $|\Phi_0\rangle$ to a singly-excited state given by the determinant $|\Phi_a^p\rangle$. The illustration is adapted from Ref. [26].

To decrease the computational effort of CIS we may choose to allow excitation from only a subset of the included orbitals in the Hartree–Fock ground state. An example of this is when only allowing excitation from, for instance, the $2p$ orbital in neon, while keeping the electrons in the $1s$ and $2s$ orbitals in the core. We have used this approach in all of our works involving CIS calculations in neon; allowing excitation (ionization) from the $2p$ orbital only in Paper I, Paper II and Paper IV, and the $\{2s, 2p\}$ orbitals in Paper VI.

In Fig. 7 the $2s$, $3s$, and $4s$ wavefunctions in hydrogen are compared to corresponding CIS wavefunctions in helium. The CIS wavefunctions follow the same nodal structure as the hydrogen counterpart, but they are pulled in slightly by the Hartree–Fock potential.

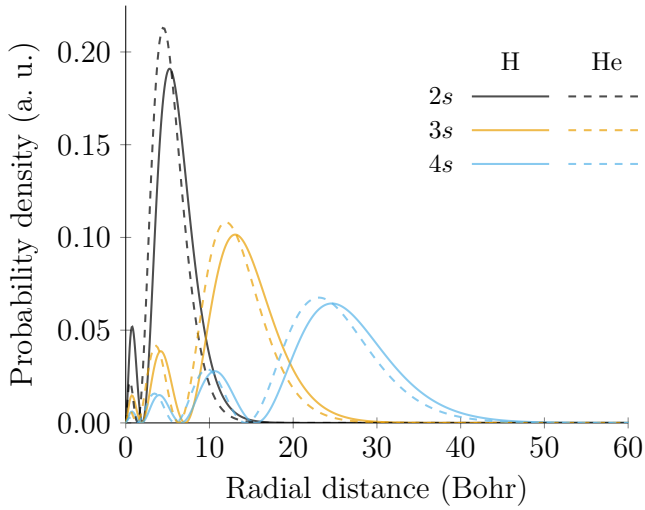

Figure 7: Comparison between the $2s$, $3s$, and $4s$ wave functions in hydrogen and in CIS helium.

3 Form of light–matter interactions

To introduce light–matter interactions, we treat the field externally and make the substitution $\hat{\mathbf{p}}_i \to \hat{\mathbf{p}}_i - q\mathbf{A}(\mathbf{r}_i, t)$ [1]. The light–matter description is hence understood semi-classically, with the light part treated classically and acting on the quantized-matter part treated quantum mechanically. The potentials $\mathbf{A}(\mathbf{r}, t)$ and $U(\mathbf{r}, t)$ need to be constructed such that the derived fields satisfy Maxwell's equations (see Ref. [31]):

$$\nabla \cdot \mathbf{E}(\mathbf{r}, t) = \frac{\rho(\mathbf{r})}{\epsilon_0}, \tag{3.1a}$$

$$\nabla \cdot \mathbf{B}(\mathbf{r}, t) = 0, \tag{3.1b}$$

$$\nabla \times \mathbf{E}(\mathbf{r}, t) = -\frac{\partial \mathbf{B}(\mathbf{r}, t)}{\partial t}, \tag{3.1c}$$

$$\nabla \times \mathbf{B}(\mathbf{r}, t) = \mu_0 \mathbf{j}(\mathbf{r}, t) + \epsilon_0 \mu_0 \frac{\partial \mathbf{E}(\mathbf{r}, t)}{\partial t}, \tag{3.1d}$$

where μ_0 is the vacuum permeability, and $\rho(\mathbf{r}, t)$ and $\mathbf{j}(\mathbf{r}, t)$ are the charge density and current density, respectively. The electric and magnetic fields derived from the potentials are respectively given by

$$\mathbf{B}(\mathbf{r}, t) = \nabla \times \mathbf{A}(\mathbf{r}, t), \tag{3.2a}$$

$$\mathbf{E}(\mathbf{r}, t) = -\nabla U(\mathbf{r}, t) - \frac{\partial \mathbf{A}(\mathbf{r}, t)}{\partial t}. \tag{3.2b}$$

The total N-body Hamiltonian then becomes

$$\hat{H} = \sum_{n=1}^{N} \left(\frac{1}{2m_\mathrm{e}} [\hat{\mathbf{p}}_n - q\mathbf{A}(\mathbf{r}_n, t)]^2 - \frac{q^2}{4\pi\epsilon_0} \frac{Z}{|\mathbf{r}_n|} \right) + \frac{q^2}{4\pi\epsilon_0} \sum_{n>m=1}^{N} \frac{1}{|\mathbf{r}_n - \mathbf{r}_m|}, \tag{3.3}$$

which can be separated into the field-free Hamiltonian in Eq. (2.2) and a light–matter-interaction Hamiltonian,

$$\hat{H} = \hat{H}^{(\mathrm{atom})} + \hat{V}^{(\mathrm{int})}(\mathbf{r}_n, t), \tag{3.4}$$

where the atomic Hamiltonian is given by Eq. (2.2), and the interaction Hamiltonian is given by two terms,

$$\hat{V}^{(\mathrm{int})}(\mathbf{r}_n, t) = \hat{V}_1^{(\mathrm{int})}(\mathbf{r}_n, t) + \hat{V}_2^{(\mathrm{int})}(\mathbf{r}_n, t) : \tag{3.5}$$

one linear in the vector potential,

$$\hat{V}_1^{(\mathrm{int})}(\mathbf{r}_n, t) = -\frac{q}{2m_\mathrm{e}} \sum_{n=1}^{N} (\hat{\mathbf{p}}_n \cdot \mathbf{A}(\mathbf{r}_n, t) + \mathbf{A}(\mathbf{r}_n, t) \cdot \hat{\mathbf{p}}_n) ; \tag{3.6}$$

and one term quadratic in the vector potential,

$$\hat{V}_2^{(\mathrm{int})}(\mathbf{r}_n, t) = \frac{q^2}{2m_\mathrm{e}} \sum_{n=1}^{N} |\mathbf{A}(\mathbf{r}_n, t)|^2. \tag{3.7}$$

This interaction Hamiltonian is central to our treatment of ionization. There is a slight discrepancy in notation compared to the Coulombic $\hat{V}$ that is introduced as a correction to the mean-field Hamiltonian in Sec. 2, Eq. (2.22). There, the indices $0, 1, 2$ refer to the potential being a zero-, one-, or two-body operator in the framework of second quantization. For the interaction potentials $\hat{V}_1^{(\mathrm{int})}$ and $\hat{V}_2^{(\mathrm{int})}$, on the other hand, the indices refer to the order in which the vector potential appears.

3.1 Gauge considerations

By inserting the definition of the fields from the potentials in Eq. (3.2) into Maxwell's equations in Eq. (3.1), we obtain Maxwell's equations in potential form:

$$\Delta U + \frac{\partial}{\partial t}(\nabla \cdot \mathbf{A}) = -\frac{\rho}{\epsilon_0}, \tag{3.8a}$$

$$\Delta \mathbf{A} - \frac{1}{c^2} \frac{\partial^2 \mathbf{A}}{\partial t^2} - \nabla \left(\nabla \cdot \mathbf{A} + \frac{1}{c^2} \frac{\partial U}{\partial t} \right) = -\mu_0 \mathbf{j}. \tag{3.8b}$$

Maxwell's equations in potential form do not have a unique solution, but an infinite number of potentials solve Eq. (3.8). This class of functions is found by a *gauge transformation*, given by

$$\mathbf{A}(\mathbf{r}_n, t) \to \mathbf{A}'(\mathbf{r}_n, t) = \mathbf{A}(\mathbf{r}_n, t) + \nabla F(\mathbf{r}, t), \tag{3.9a}$$

$$U(\mathbf{r}_n, t) \to U'(\mathbf{r}_n, t) = U(\mathbf{r}_n, t) - \frac{\partial}{\partial t} F(\mathbf{r}_n, t). \tag{3.9b}$$

These potentials all satisfy Eq. (3.8), while still corresponding to the same physical fields. Since the potentials $\mathbf{A}$ and U do not uniquely determine the physical electric fields and magnetic fields, while still satisfying Maxwell's equations in Eq. (3.8), we need a *gauge fixing condition* that removes the ambiguity of the potentials. A common choice is the *Coulomb gauge*, $\nabla \cdot \mathbf{A} = 0$. The scalar potential U can arbitrarily be chosen to zero asymptotically. Under this condition, the canonical momentum operator and the vector potential commute and the interaction Hamiltonian can be simplified to

$$\hat{V}^{(\mathrm{int})}(\mathbf{r}_n, t) = \sum_{n=1}^{N} \left[-\frac{q}{m_\mathrm{e}} \hat{\mathbf{p}}_n \cdot \mathbf{A}(\mathbf{r}_n, t) + \frac{q^2}{2m_\mathrm{e}} |\mathbf{A}(\mathbf{r}_n, t)|^2 \right]. \tag{3.10}$$

In a quantum-mechanical description of matter interacting with light, the gauge transformation in Eq. (3.9) corresponds to a time-dependent unitary transformation ($T^\dagger T = 1$), see Ref. [32],

$$|\psi(\mathbf{r}_n, t)\rangle \to |\psi'(\mathbf{r}_n, t)\rangle = T|\psi'(\mathbf{r}_n, t)\rangle, \tag{3.11}$$

with

$$T = \exp\left(\mathrm{i}\frac{q}{\hbar} F\right). \tag{3.12}$$

Not all unitary transformations correspond to a gauge transformation however. In order for the unitary transformation to satisfy the *gauge principle*, the transformation function $F = F(\mathbf{r}_n, \mathbf{A}, U, t)$ needs to be a local function of $\mathbf{r}_n$, $\mathbf{A}$, U, and t, as these (or their time derivatives) are the only variables necessary to completely specify the dynamics of the system [32]. We refer to the local transformation of the wavefunction in Eq. (3.11) as a gauge transformation of the first kind and the gauge transformations in Eq. (3.9) as a gauge transformation of the second kind [33].

By entering the unitary transformation in Eq. (3.11) into the time-dependent Schrödinger equation, we obtain

$$\mathrm{i}\hbar \frac{\partial}{\partial t} \psi'(t) = \hat{H}'(t) \psi'(t), \tag{3.13}$$

where the transformed Hamiltonian is given by

$$\hat{H}'(t) = T\hat{H}(t)T^\dagger + \mathrm{i}\hbar \frac{\partial T}{\partial t} T^\dagger. \tag{3.14}$$

Both the Hamiltonian and the wavefunction adapt to the gauge chosen and therefore also the evolution operator. The evolution operator evolves a wavefunction, from an initial state $|\psi(t_0)\rangle$ to a state $|\psi(t)\rangle$, and is given by

$$\hat{U}(t,t_0) = \mathcal{T}\exp\left(-\frac{\mathrm{i}}{\hbar}\int_{t_0}^{t}\mathrm{d}t'\;\hat{H}(t')\right), \tag{3.15}$$

where $\mathcal{T}$ is the time-ordering operator. We obtain by inserting the evolution operator into Eq. (3.11)

$$\begin{aligned}|\psi'(\mathbf{r}_n,t)\rangle &= T|\psi(\mathbf{r}_n,t)\rangle \\ &= T\hat{U}(t,t_0)|\psi(\mathbf{r}_n,t_0)\rangle \\ &= T\hat{U}(t,t_0)T^\dagger|\psi'(\mathbf{r}_n,t_0)\rangle \\ &= \hat{U}'(t,t_0)|\psi'(\mathbf{r}_n,t_0)\rangle.\end{aligned} \tag{3.16}$$

While the wavefunction depends on the gauge by the gauge transformation of the first kind, Eq. (3.11), it follows from Eq. (3.16) that *transition amplitudes* are *gauge invariant* by

$$\langle\psi_\mathrm{f}(t)|\hat{U}(t,t_0)|\psi_\mathrm{i}(t_0)\rangle = \langle\psi'_\mathrm{f}(t)|\hat{U}'(t,t_0)|\psi'_\mathrm{i}(t_0)\rangle. \tag{3.17}$$

Any *physical* observable, derivable from the evolution operator, will hence be invariant under a gauge transformation, c.f. Ref. [34], which means that

$$\langle\psi|\hat{O}|\psi\rangle = \langle\psi'|\hat{O}'|\psi'\rangle. \tag{3.18}$$

It is not enough however that the observable is represented by a linear hermitian operator. For instance, the Hamiltonian corresponds to an observable, but the *absolute* energy is not a physical measurable in an experiment [32]. Another example of a gauge-dependent quantity is the canonical momentum, which will be considered in our review of the dipole approximation in Sec. 3.2. Moreover, the gauge principle in Eq. (3.18) is only valid if the configuration space is complete. In Sec. 2.2 we introduced truncated configuration spaces, in particular to the level of single excitations, CIS, for which the gauge principle is not guaranteed. Indeed, in Sec. 5 where we extend the CIS approximation to a time-dependent formulation, the gauge principle does not hold. We will discuss this matter for the cases of *velocity gauge* and *length gauge*, which are introduced in Sec. 3.2. The gauge choice will then be important since it affects the possible agreement with experimental data. For instance, Kobe showed that velocity gauge is an unsuitable choice for describing a two-level atom in a field [35], why length gauge should be preferred when studying Rabi dynamics. On the other hand, the gauge choice is important from a practical point of view since a calculation in a certain gauge may converge considerably faster. Notably, the length gauge is notorious for requiring a large number of angular momenta to converge strong-field processes with long-wavelength fields [23, 36], which inspired us to develop the TRK correction to velocity gauge time-dependent configuration-interaction singles (TDCIS), described in Sec. 5.2, in Paper VI.

3.2 The dipole approximation

Consider a single electron bound to an atom that interacts with a field given by the vector potential in the interaction Hamiltonian in Eq. (3.10). The extension to many electrons, with coordinates $\mathbf{r}_n$, is readily obtainable. The vector potential, for simplicity monochromatic, but easily generalizable to any spectral components, is given by

$$\mathbf{A}(\mathbf{r},t) = A_0 \cos(\omega t - \mathbf{k}\cdot\mathbf{r}) = \frac{A_0}{2}\left[\mathrm{e}^{-\mathrm{i}(\omega t - \mathbf{k}\cdot\mathbf{r})} + \mathrm{e}^{\mathrm{i}(\omega t - \mathbf{k}\cdot\mathbf{r})}\right]\hat{\varepsilon}, \tag{3.19}$$

where $\hat{\varepsilon}$ is the direction of polarization, ω is the angular frequency of the field, $\mathbf{k}$ is the associated wave vector with magnitude $|\mathbf{k}| = 2\pi/\lambda$, and $A_0 = |\mathbf{A}(\mathbf{r},t)|$ describes the amplitude of the vector potential. The first term in the interaction Hamiltonian in Eq. (3.10), $\hat{V}_1^{(\mathrm{int})}$, may induce a transition from a bound state in the atom, $|\psi_i\rangle$, to a continuum state $|\psi_f\rangle$, by absorption of a photon. The transition rate for an interaction of duration T is given by *Fermi's golden rule*, see for instance Ref. [1],

$$\Gamma = \sum_f w_{fi} = \frac{2\pi}{\hbar}\frac{q^2}{m_\mathrm{e}^2}\frac{A_0^2}{4}\sum_f |\langle\psi_f|\hat{p}_{\hat{\varepsilon}}\mathrm{e}^{-\mathrm{i}(\omega t - \mathbf{k}\cdot\mathbf{r})}|\psi_i\rangle|^2 \delta^{(T)}(E_f - E_i - \hbar\omega), \tag{3.20}$$

where $\delta^{(T)}$ is the delta function of width $\hbar/T$ of the final continuum states, which we evaluate at $E_f = E_i + \hbar\omega$. We only consider $\exp[-\mathrm{i}(\omega t - \mathbf{k}\cdot\mathbf{r})]$ for absorption, and the individual transition rates are therefore given by

$$w_{fi} = \frac{A_0^2 q^2 \pi}{2m_\mathrm{e}^2\hbar}|\langle\psi_f|\hat{p}_{\hat{\varepsilon}}\mathrm{e}^{-\mathrm{i}(\omega t - \mathbf{k}\cdot\mathbf{r})}|\psi_i\rangle|^2. \tag{3.21}$$

For a wavelength much longer than the atomic radius, $\lambda \gg \alpha_0 \approx 5.29 \times 10^{-11}\,\mathrm{m} = 5.29$ Å, referred to the Bohr radius, the spatial dependence of the vector potential can be neglected since the electrons are (approximately) subject to a spatially uniform field. This is done by keeping only the zeroth-order term of the expansion,

$$\mathrm{e}^{\mathrm{i}\mathbf{k}\cdot\mathbf{r}} = 1 + \mathrm{i}\mathbf{k}\cdot\mathbf{r} + \mathcal{O}\left(|\mathbf{k}\cdot\mathbf{r}|^2\right) \approx 1. \tag{3.22}$$

The first-order term is small, $\mathbf{k}\cdot\mathbf{r} \sim 2\pi r/\lambda \ll 1$, for the fields considered. A typical XUV field with photon energy $\hbar\omega \sim 50\,\mathrm{eV}$ has a wavelength of roughly $\lambda \sim 25\,\mathrm{nm}$, compared to the *radius* of the atom of a few Å[5], which is a fraction of a percent of the wavelength.

Within the dipole approximation it follows from Eq. (3.2) that the magnetic field is zero and the electric field is a function of only time,

$$\mathbf{E}(t) = -\frac{\mathrm{d}\mathbf{A}(t)}{\mathrm{d}t}. \tag{3.23}$$

[5]The radius of an atom is however not a well-defined physical constant as one can assert many different measures of the atom's spatial extent.

The one-particle Hamiltonian, which we refer to as the *velocity gauge* Hamiltonian, becomes

$$\hat{H}^{(\mathrm{vg})}(\mathbf{r},t) = \frac{\hat{\mathbf{p}}^2}{2m_\mathrm{e}} + \hat{V}_1^{(\mathrm{int})} + \hat{V}_2^{(\mathrm{int})} + \hat{V}_\mathrm{c}(\mathbf{r}), \tag{3.24}$$

with the term linear in the vector potential given by

$$\hat{V}_1^{(\mathrm{int})}(t) = -\frac{q}{m_\mathrm{e}}\hat{\mathbf{p}}\cdot\mathbf{A}(t), \tag{3.25}$$

and the term quadratic in the vector potential given by

$$\hat{V}_2^{(\mathrm{int})}(t) = \frac{q^2|\mathbf{A}(t)|^2}{2m_\mathrm{e}}. \tag{3.26}$$

By performing a gauge transformation with $F = -\mathbf{A}(t)\cdot\mathbf{r}$, we obtain the length gauge Hamiltonian,

$$\hat{H}^{(\mathrm{lg})}(\mathbf{r},t) = \frac{\hat{\mathbf{p}}^2}{2m_\mathrm{e}} - q\hat{\mathbf{r}}\cdot\mathbf{E}(t) + \hat{V}_\mathrm{c}(\mathbf{r}). \tag{3.27}$$

In the same way as the dipole approximation enters Fermi's golden rule in Eq. (3.20), we may describe bound state transitions within the dipole approximation. In length gauge, the transition matrix elements are given by

$$\hbar\Omega = -q\langle\psi_m|\hat{\mathbf{r}}\cdot\mathbf{E}(t)|\psi_n\rangle, \tag{3.28}$$

which we recall defines the Rabi frequency in Eq. (1.14). From this matrix element we may define the (e.g. z-component) *oscillator strength* between two bound states,

$$f_{mn} = \frac{2m_\mathrm{e}}{\hbar}\omega_{mn}|\langle\psi_m|\hat{z}|\psi_n\rangle|^2, \tag{3.29}$$

which describes the dimensionless probability of an (electric) dipole transition. We will return to the oscillator strength in Sec. 4.1 where we discuss sum rules for atomic transitions. Sum rules will be important to understand the limitations of truncated configuration spaces as mentioned briefly in the end of Sec. 3.1.

The dipole moment $\langle\psi_m|\hat{z}|\psi_n\rangle$ imposes a set of rules, between which quantum states a transition may occur. These well-known *selection rules* are stringent and decide whether a dipole transition is possible [22]. Apart from these rules, Fano discussed the existence of *propensity rules* [37], which say that the angular momentum tends to increase, rather than decrease, after absorption of a photon. These rules were extended by Busto et al. [38] to include continuum transitions, and studied in higher order by including exchange of multiple photons in the continuum in Paper I. In Sec. 7.1 where we summarize the results of Paper I, propensity rules and intrinsic differences between absorption and emission of photons in the continuum are discussed.

The canonical momentum in either gauge is given by $\hat{\mathbf{p}} = -\mathrm{i}\hbar\nabla$, but its connection to the kinetic momentum varies. In length gauge, the kinetic momentum equals the canonical momentum: $\hat{\mathbf{\Pi}} = \hat{\mathbf{p}}$, but in general it is given by

$$\hat{\mathbf{\Pi}} = \hat{\mathbf{p}} - q\mathbf{A}. \tag{3.30}$$

That $\hat{\mathbf{\Pi}} = \hat{\mathbf{p}}$ in length gauge can be understood directly from the gauge transformation in Eq. (3.9a) of $\mathbf{A}(t)$ which gives zero,

$$\mathbf{A}^{(\mathrm{lg})}(t) = \mathbf{A}^{(\mathrm{vg})}(t) + \nabla F = 0. \tag{3.31}$$

As mentioned, the canonical momentum is not a measurable quantity, but the kinetic momentum is on the other side, and has expectation value $\langle\hat{\mathbf{\Pi}}\rangle = \langle\hat{\mathbf{p}}\rangle - q\mathbf{A}$. In both length gauge and velocity gauge, the canonical momentum and the kinetic momentum will be equal asymptotically, when we deal with finite pulses, $\mathbf{A}(t > t_{\mathrm{asympt.}}) = 0$.

We will further employ the *reduced* velocity gauge, which is obtained from the velocity gauge by a gauge transformation with

$$T(t) = \exp\left[-\mathrm{i}\frac{q}{\hbar}\int^{t} \mathrm{d}t' \, \frac{\mathbf{A}^2(t')}{2}\right]. \tag{3.32}$$

In this case, the Hamiltonian becomes

$$\hat{H}^{(\mathrm{vg}')}(\mathbf{r}, t) = \frac{\hat{\mathbf{p}}}{2m_{\mathrm{e}}}\hat{V}_1^{(\mathrm{int})}(t) + \hat{V}_{\mathrm{c}}(\mathbf{r}). \tag{3.33}$$

4 Sum rules for oscillator strengths

Sum rules exist for the oscillator strengths. One sum rule that has been used extensively in this thesis is the TRK sum rule, see e.g. Ref. [3, 30]. The TRK sum rule is a general sum rule that is valid for any atom or molecule with or without an external static electric field [3].

TRK has been used extensively in Paper VI to calculate the polarization energy shift in a CIS calculation. In the following section, Sec. 4.1, TRK is derived. We then use TRK in Sec. 4.2 to calculate energy shifts for static and oscillating low-frequency fields by using perturbation theory.

4.1 Derivation of Thomas–Reiche–Kuhn sum rule

The Thomas–Reiche–Kuhn sum rule expresses that the sum of all oscillator strengths is equal to the number of electrons,

$$\sum_{n'} f_{nn'} = N, \tag{4.1}$$

see Eq. (61.1) in Ref. [3]. Consider the sum of all oscillator strengths, as defined in Eq. (3.29),

$$\sum_{m} f_{nm} = \frac{2m_\mathrm{e}}{\hbar} \sum_{m} (E_m - E_n) |\langle m|\hat{z}|n\rangle|^2, \tag{4.2}$$

where $|n\rangle$ and $|m\rangle$ are eigenstates to the one-particle Hamiltonian with a local potential with respective energies E_n and E_m. We will use two elementary commutation relations[6],

$$[\hat{H}, \hat{z}] = -\frac{\mathrm{i}\hbar}{m_\mathrm{e}} \hat{p}_z, \tag{4.3}$$

$$[\hat{p}_z, \hat{z}] = -\mathrm{i}\hbar \sum_{n,m=1}^{N_\mathrm{e}} \delta_{n,m} = -\mathrm{i}\hbar N, \tag{4.4}$$

the first of which is used to write

$$\sum_{m} f_{nm} = -\frac{2\mathrm{i}}{\hbar} \sum_{m} \langle n|\hat{z}|m\rangle \langle m|\hat{p}_z|n\rangle. \tag{4.5}$$

We further use that $f_{nm} = -f_{mn}$ to write

$$\sum_{j} f_{nm} = \sum_{m} \frac{1}{2} (f_{nm} - f_{mn}), \tag{4.6}$$

which gives the TRK relation

$$\sum_{m} f_{nm} = \frac{\mathrm{i}}{\hbar} \langle n|[\hat{p}_z, \hat{z}]|n\rangle = N. \tag{4.7}$$

[6]The first of these relations, Eq. (4.3), is valid only in the presence of local potentials such as the Hartree potential. For a nonlocal potential on the other hand, such as the Hartree–Fock exchange potential, it only holds approximately. We will return to this restriction when discussing the TRK correction to TDCIS in Sec. 5.2.

4.2 Energy shifts from sum rules

The eigenstates of the field-free Hamiltonian in Eq. (2.2), will no longer be the eigenstates if an external static electric field E is applied. An atom subjected to a static electric field will have its ground state energy level shifted proportional to the static polarizability of the atom α_0 in what is known as the dc Stark shift,

$$\frac{\mathrm{d}\Delta E_1}{\mathrm{d}E} = -\alpha_0 E. \tag{4.8}$$

The TRK sum rule in Eq. (4.7) can be used to calculate these energy shifts of a general atom in an external static potential [3]. Although the general applicability of TRK, we here perform the calculation of the Stark shift of the ground state for an atom in the context of CIS. We therefore use the Hartree–Fock ground state $|\Psi_0\rangle \to |\Phi_0\rangle$ as reference, and the singly-excited states $|\Psi_n\rangle \to |\Phi_a^p\rangle$ to represent excitations.

Consider the total Hamiltonian given by the atomic Hamiltonian with an external and spatially uniform static vector potential, acting along the z-axis. In the framework of second quantization, cf. Eq. (2.17), the potential is given by

$$\hat{V}_1^{(\mathrm{static})} = -\frac{q}{m_\mathrm{e}} A_0 \sum_{ij}^{N} \langle i|\hat{p}_z|j\rangle \hat{a}_i^\dagger \hat{a}_j. \tag{4.9}$$

Within CIS, and to second-order perturbation theory, the energy shift of the Hartree–Fock ground state, due to interaction with the potential in Eq. (4.9), is given by

$$\Delta E_1^{(2)} = \lim_{\eta\to 0^+} \sum_{ap} \frac{\langle\Phi_0|\hat{V}_1^{(\mathrm{static})}|\Phi_a^p\rangle\langle\Phi_a^p|\hat{V}_1^{(\mathrm{static})}|\Phi_0\rangle}{\varepsilon_a - \varepsilon_p + \mathrm{i}\eta}. \tag{4.10}$$

The Hartree–Fock ground state is defined to have zero energy, and we therefore omit it in the energy denominator. The one-particle matrix elements are nonzero only for the case when i is a bound orbital and j is a virtual orbital, in accordance with Eq. (2.20b), $\langle\Phi_0|\hat{V}_1^{(\mathrm{static})}|\Phi_a^p\rangle = \langle a|\hat{v}_1|p\rangle$. By using the relation between $\hat{p}_z$ and $\hat{z}$ under commutation with the atomic Hamiltonian in Eq. (4.3), we may write this as

$$\begin{aligned}\Delta E_1^{(2)} = \mathrm{i}\frac{q^2}{m_\mathrm{e}\hbar}\frac{A_0^2}{2} \lim_{\eta\to 0^+} \sum_{ap} \frac{1}{\varepsilon_a - \varepsilon_p + \mathrm{i}\eta} \\ \times \left(\langle a|\hat{p}_z|p\rangle\langle p|\left[\hat{H}^{(\mathrm{atom})},\ \hat{z}\right]|a\rangle + \langle a|\left[\hat{H}^{(\mathrm{atom})},\ \hat{z}\right]|p\rangle\langle p|\hat{p}_z|a\rangle\right),\end{aligned} \tag{4.11}$$

which simplifies to

$$\Delta E_1^{(2)} = \mathrm{i}\frac{q^2}{m_\mathrm{e}\hbar}\frac{A_0^2}{2} \sum_{ap} \left(\langle a|\hat{p}_z|p\rangle\langle p|\hat{z}|a\rangle - \langle a|\hat{z}|p\rangle\langle p|\hat{p}_z|a\rangle\right). \tag{4.12}$$

The sum over p can be simplified by the identity $\sum_p |p\rangle\langle p| = 1 - \sum_b |b\rangle\langle b|$, but the sum over core orbitals b yields zero. We may therefore replace the sum over the virtual space by identity to obtain

$$\sum_{ap} \left(\langle a|\hat{p}_z|p\rangle\langle p|\hat{z}|a\rangle - \langle a|\hat{z}|p\rangle\langle p|\hat{p}_z|a\rangle \right) = \sum_a \langle a|[\hat{p}_z,\ \hat{z}]|a\rangle = -\mathrm{i}\hbar N, \tag{4.13}$$

which is in accordance with the TRK rule. The second-order energy shift of a static vector potential is hence given by

$$\Delta E_1^{(2)} = \frac{q^2 A_0^2}{2m_\mathrm{e}} N. \tag{4.14}$$

The corresponding ac Stark shift of an atom in an oscillatory potential is calculated in a similar fashion. Consider the interaction terms in the velocity gauge Hamiltonian in Eq. (3.24) with the vector potential polarized along the z-axis, expressed in second quantization,

$$\hat{V}_1^{(\mathrm{int})}(t) = -\frac{q}{m_\mathrm{e}} A(t) \sum_{ij} \langle i|\hat{p}_z|j\rangle \hat{a}_i^\dagger \hat{a}_j, \tag{4.15}$$

for the term linear in the vector potential, and

$$\hat{V}_2^{(\mathrm{int})}(t) = \frac{q^2 A^2(t)}{2m_\mathrm{e}} \hat{n}, \tag{4.16}$$

for the term quadratic in the vector potential. The operator $\hat{n}$ is the number operator

$$\hat{n} = \sum_i \hat{a}_i^\dagger \hat{a}_i. \tag{4.17}$$

We can decompose the term linear in the vector potential into co-rotating and counter-rotating parts,

$$\hat{V}_1(t) = \hat{V}_1^{(+)} \exp(-\mathrm{i}\omega t) + \hat{V}_1^{(-)} \exp(\mathrm{i}\omega t), \tag{4.18}$$

with

$$\hat{V}_1^{(+)} = \hat{V}_1^{(-)} = -\frac{q}{2m_\mathrm{e}} A_0 \sum_{ij} \langle i|\hat{p}_z|j\rangle \hat{a}_i^\dagger \hat{a}_j. \tag{4.19}$$

In lowest-order perturbation theory, the energy shift due to interaction with the potential linear in the vector potential is given, within the rotating-wave approximation, by

$$\begin{aligned} \langle \Delta E_1^{(2)}(\omega) \rangle = \lim_{\eta \to 0^+} \sum_n & \frac{\langle \Psi_0|\hat{V}_1^{(+)}|\Psi_n\rangle\langle\Psi_n|\hat{V}_1^{(-)}|\Psi_0\rangle}{E_0 - \hbar\omega - E_n + \mathrm{i}\eta} \\ & + \frac{\langle \Psi_0|\hat{V}_1^{(-)}|\Psi_n\rangle\langle\Psi_n|\hat{V}_1^{(+)}|\Psi_0\rangle}{E_0 + \hbar\omega - E_n + \mathrm{i}\eta}. \end{aligned} \tag{4.20}$$

We may Taylor expand this expression about $\omega = 0$ to identify the leading terms of the energy shift. The expression and its Taylor expansion are on the form

$$\frac{v}{\varepsilon + \hbar\omega} + \frac{v}{\varepsilon - \hbar\omega} = 2\frac{v}{\varepsilon}\left(1 + \frac{\hbar^2\omega^2}{\varepsilon^2}\right) + \mathcal{O}(\omega^4), \tag{4.21}$$

which provides us with the expression

$$\begin{aligned}\langle \Delta E_1^{(2)}(\omega)\rangle &= 2\sum_{n\neq 0}\left(\langle \Delta E_{n,1,0}^{(2)}\rangle + \langle \Delta E_{n,1,2}^{(2)}\rangle\right) + \mathcal{O}(\omega^4) \\ &= 2\sum_{n\neq 0}\left(\frac{|(V_1^{(\mathrm{int})})_{0n}|^2}{E_0 - E_n} + \frac{\hbar^2\omega^2}{(E_0 - E_n)^2}\frac{|(V_1^{(\mathrm{int})})_{0n}|^2}{E_0 - E_n}\right) + \mathcal{O}(\omega^4),\end{aligned} \tag{4.22}$$

By using the expression for the oscillator strengths in Eq. (3.29), the zeroth-order term can now be evaluated using the TRK sum rule in Eq. (4.2), which gives

$$\langle \Delta E_{1,0}^{(2)}\rangle = -2\frac{q^2A_0^2}{8m_\mathrm{e}}\sum_{n\neq 0} f_{n0} = -\frac{q^2A_0^2}{4m_\mathrm{e}}N. \tag{4.23}$$

This is half the value obtained for a static field, Eq. (4.14). The factor of two difference is comes from averaging over the electric field and can be understood in terms of energy conservation. In order for the energy to be conserved, by absorbing one photon and emitting one photon, we must act once with $\hat{V}_1^{(+)}$ and once with $\hat{V}_1^{(-)}$. In the limiting case of $\omega \to 0$, we may however act with any combination of $\hat{V}_1^{(\pm)}$, while still fulfilling energy conservation. The total second-order energy shift due to $\hat{V}_1$ is therefore calculated to

$$\langle \Delta E_1^{(2)}(\omega)\rangle = -\frac{A_0^2}{4}\left(\frac{q^2}{m_\mathrm{e}}N + \omega^2\alpha_0\right) + \mathcal{O}(\omega^4), \tag{4.24}$$

where

$$\alpha_0 = \frac{q^2}{m_\mathrm{e}}\sum_{n\neq 0}\frac{f_{n0}}{(\omega_0 - \omega_n)^2} \tag{4.25}$$

is identified as the atomic polarizability [39]. The sum in Eq. (4.25) is interpreted as the sum of the polarizabilities of the individual atomic oscillators weighted by their respective oscillator strengths.

The energy shift due to the first-order interaction in $\hat{V}_2$ can be evaluated directly to

$$\langle \Delta E_2^{(1)}(\omega)\rangle = \frac{q^2\langle A^2(t)\rangle}{2m_\mathrm{e}}N = \frac{q^2A_0^2}{4m_\mathrm{e}}N, \tag{4.26}$$

which means that the zeroth-order energy shift due to the $\hat{V}_1$ potential cancels by the energy shift of the $\hat{V}_2$ potential. We are thus left with only the shift due to the atomic polarizability

$$\langle \Delta E^{(2)}(\omega) \rangle = -\frac{\omega^2 A_0^2 \alpha_0}{4} + \mathcal{O}(\omega^4) = -\frac{E_0^2 \alpha_0}{4} + \mathcal{O}(\omega^4). \tag{4.27}$$

This delicate cancellation is unique to the velocity gauge and is the background to the TRK correction to TDCIS in Paper VI, which we discuss in Sec. 5.2. In length gauge on the other hand, this energy shift is retrieved directly, and we do not rely on any such cancellation.

5 Time-Dependent Configuration-Interaction Singles

With the electronic structure of the atom established in Sec. 2 and the form of light–matter interactions given in Sec. 3 and Sec. 4, we here combine these parts to develop the equations of motion of an atom subject to an electric field. We treat this within the TDCIS approximation as done in Refs. [40, 41].

5.1 Derivation of equations of motion

We start from the CI expansion as given in Eq. (2.27), truncated at the level of single excitations, where $|\Phi_0\rangle$ is the HF determinant found from the variational principle by minimizing Eq. (2.10), and $|\Phi_a^p\rangle$ are single-excitation determinants constructed according to Eq. (2.16). The time dependence, which is contained in the electric field, is put in the expansion coefficients α, to yield

$$|\Psi(t)\rangle = \alpha_0(t)|\Phi_0\rangle + \sum_{a,p} \alpha_a^p(t)|\Phi_a^p\rangle. \tag{5.1}$$

These states are therefore the field-free eigenstates of the mean-field Hamiltonian since only the coefficients are let to vary. The corresponding equations of motion of the expansion coefficients will be a system of ordinary differential equations where we specify the initial condition in $\alpha(t_0)$. Often, but not necessarily always, the initial condition is that the atom is found in its ground state configuration described by the HF determinant $|\Phi_0\rangle$. This corresponds to the initial conditions $\alpha_0(t_0) = 1$ and $\alpha_a^p(t_0) = 0$, with the phase arbitrarily fixed to zero at $t = t_0$.

To derive the equations of motion in TDCIS, we insert the state in Eq. (5.1) into TDSE,

Eq. (2.1), and project on $|\Phi_0\rangle$ and $|\Phi_a^p\rangle$, to obtain

$$i\dot{\alpha}_0(t) = \alpha_0(t)\langle\Phi_0|\hat{H}|\Phi_0\rangle + \sum_{a,p}\alpha_a^p(t)\langle\Phi_0|\hat{H}|\Phi_a^p\rangle, \tag{5.2a}$$

$$i\dot{\alpha}_a^p(t) = \alpha_0(t)\langle\Phi_a^p|\hat{H}|\Phi_0\rangle + \sum_{b,q}\alpha_b^q(t)\langle\Phi_a^p|\hat{H}|\Phi_b^q\rangle. \tag{5.2b}$$

To work out the matrix elements in Eq. (5.2) we combine the atomic Hamiltonian from Sec. 2, expressed as a mean-field Hamiltonian and a perturbation as in Eq. (2.18), with the light–matter interaction Hamiltonian from Sec. 3, such that the N-electron system interacting with an external electric field is given by

$$\hat{H}(t) = \hat{H}_0^{(\mathrm{HF})} + \hat{V} + \hat{V}^{(\mathrm{int})}(t). \tag{5.3}$$

In particular, we make use of the normal form of the correction $\hat{V} = \hat{V}_0 + \hat{V}_2$, given in Eq. (2.22).

Within the noggles subspace

The diagonal HF matrix element within the subspace of no excitations (the *noggles* subspace) in Eq. (5.2a) gives an energy shift equal to the zeroth-order HF energy, $E_0^{(\mathrm{HF})}$, by summing over the one-particle HF orbital energies,

$$\begin{aligned}\langle\Phi_0|\hat{H}_0^{(\mathrm{HF})}|\Phi_0\rangle &= \sum_c \Big(\langle c|\hat{h}_0|c\rangle + \langle c|\hat{u}^{(\mathrm{HF})}|c\rangle\Big) \\ &= \sum_c \varepsilon_c = E_0^{(\mathrm{HF})}.\end{aligned} \tag{5.4}$$

We identify further an energy shift equal to the first-order HF energy, $E_1^{(\mathrm{HF})}$, due to the zero-body potential $\hat{V}_0$, see Eq. (2.24),

$$\langle\Phi_0|\hat{V}_0|\Phi_0\rangle = -\frac{1}{2}\sum_c\langle c|\hat{u}^{(\mathrm{HF})}|c\rangle = E_1^{(\mathrm{HF})}. \tag{5.5}$$

For the second-order correction term, we instead have

$$\langle\Phi_0|\hat{V}_2|\Phi_0\rangle = 0. \tag{5.6}$$

It is therefore customary to shift the energy by the total HF energy contribution $E^{(\mathrm{HF})} = E_0^{(\mathrm{HF})} + E_1^{(\mathrm{HF})}$, such that the ground-state energy is defined zero. This renders the TDCIS equations of motion compact and has no effect on the dynamics. This yields in total a Hamiltonian of the form

$$\hat{H}(t) = \hat{H}_0^{(\mathrm{HF})} + \hat{V}_0 + \hat{V}_2 - E^{(\mathrm{HF})} + \hat{V}_1^{(\mathrm{int})}(t), \tag{5.7}$$

where the total atomic matrix element within the noggles subspace is defined zero,

$$\langle \Phi_0 | \hat{H}_0^{(\mathrm{HF})} + \hat{V} - E^{(\mathrm{HF})} | \Phi_0 \rangle = 0. \tag{5.8}$$

The matrix element of the light–matter interaction term will be discussed below.

Within the singles supsace

For the matrix elements of the singly-excited states in Eq. (5.2b), we have for the mean-field Hamiltonian a one-body operator, evaluated using Eq. (2.20c),

$$\langle \Phi_a^p | \hat{H}_0^{(\mathrm{HF})} | \Phi_b^q \rangle = \sum_c \varepsilon_c \delta_{ab} \delta_{pq} + (\varepsilon_p - \varepsilon_a) \delta_{ab} \delta_{pq}, \tag{5.9}$$

which is the zeroth-order energy of the atom in its ground state plus the energy for moving one electron from a core orbital φ_a to a virtual orbital φ_p. For the potential $\hat{V}$, we obtain the first-order energy correction to the ground-state energy for the zeroth-order potential term, as in the case of the matrix element of the HF ground state in Eq. (5.5), and a correction to the two-body Coulomb interaction,

$$\langle \Phi_a^p | \hat{V}_0 + \hat{V}_2 | \Phi_b^q \rangle = E_1^{(\mathrm{HF})} \delta_{ab} \delta_{pq} + \langle bp | r_{12}^{-1} | qa \rangle - \langle bq | r_{12}^{-1} | aq \rangle. \tag{5.10}$$

Coulomb matrix elements

The signs of the (negative) direct and (positive) exchange terms in Eq. (5.10) can be understood by looking at the two-body matrix element, cf. Eq. (2.20f),

$$\langle \Phi_a^p | r_{12}^{-1} | \Phi_b^q \rangle = \sum_c \left(\langle cp | r_{12}^{-1} | cq \rangle - \langle cp | r_{12}^{-1} | qc \rangle \right) \delta_{ab} - \langle bp | r_{12}^{-1} | aq \rangle + \langle bp | r_{12}^{-1} | qa \rangle, \tag{5.11}$$

where the sum over the core orbitals φ_c is the HF potential between two virtual states, from which we adjust for that there is no occupation in orbitals φ_b and φ_a. We further shift the energies with $E^{(\mathrm{HF})}$, to get

$$\langle \Phi_a^p | \hat{H}_0^{(\mathrm{HF})} + \hat{V} - E^{(\mathrm{HF})} | \Phi_b^q \rangle = (\varepsilon_p - \varepsilon_a) \delta_{ab} \delta_{pq} + \langle bp | r_{12}^{-1} | qa \rangle - \langle bq | r_{12}^{-1} | aq \rangle. \tag{5.12}$$

According to Brillouin's theorem, Eq. (2.13), there is no coupling due to the atomic part of the Hamiltonian between the HF reference Slater determinant and the singly-excited determinants,

$$\langle \Phi_a^p | \hat{H}_0^{(\mathrm{HF})} + \hat{V} | \Phi_0 \rangle = \langle \Phi_a^p | \hat{H}_0^{(\mathrm{HF})} + \hat{V}_0 + \hat{V}_2 | \Phi_0 \rangle = 0. \tag{5.13}$$

Dipole matrix elements

For the interaction term $\hat{V}_1^{(\mathrm{int})}(t)$, we opt for the reduced velocity gauge as in Eq. (3.33), where the interaction term is given by the one-body momentum operator defined as in Eq. (4.15). The matrix elements represent dipole transitions between atomic states and therefore the diagonal matrix elements are zero in order to respect parity,

$$\langle\Phi_0|\hat{V}_1^{(\mathrm{int})}|\Phi_0\rangle = \langle\Phi_a^p|\hat{V}_1^{(\mathrm{int})}|\Phi_a^p\rangle = 0. \tag{5.14}$$

The interaction term is however responsible for transitions between the noggles and the singles subspaces. To evaluate the dipole matrix elements between the HF ground state and singly-excited states, as well as the dipole matrix elements between singly-excited states of opposite parity, we use Eq. (2.20b)–(2.20c). This provides us with the elements

$$\langle\Phi_0|\hat{V}_1^{(\mathrm{int})}|\Phi_a^p\rangle = \mathbf{A}(t)\cdot\langle a|\hat{\mathbf{p}}|p\rangle, \tag{5.15a}$$

$$\langle\Phi_a^p|\hat{V}_1^{(\mathrm{int})}|\Phi_b^q\rangle = \mathbf{A}(t)\cdot\left(\langle p|\hat{\mathbf{p}}|q\rangle\delta_{ab} - \langle b|\hat{\mathbf{p}}|a\rangle\delta_{pq}\right). \tag{5.15b}$$

Equations of motion

By inserting the Coulomb matrix elements and the dipole matrix elements retrieved above into Eq. (5.2), we obtain the equations of motion

$$i\dot{\alpha}_0 = \sqrt{2}\mathbf{A}(t)\cdot\sum_{a,p}\alpha_a^p(t)\langle a|\hat{\mathbf{p}}|p\rangle, \tag{5.16a}$$

$$\begin{aligned} i\dot{\alpha}_a^p(t) &= (\varepsilon_p - \varepsilon_a)\alpha_a^p(t) + \sum_{b,q}\alpha_b^q(t)\left(2\langle bp|r_{12}^{-1}|qa\rangle - \langle bp|r_{12}^{-1}|aq\rangle\right) \\ &\quad + \mathbf{A}(t)\cdot\left(\sqrt{2}\alpha_0(t)\langle p|\hat{\mathbf{p}}|a\rangle + \sum_q\alpha_a^q(t)\langle p|\hat{\mathbf{p}}|q\rangle - \sum_b\alpha_b^q(t)\langle b|\hat{\mathbf{p}}|a\rangle\right), \end{aligned} \tag{5.16b}$$

where the $\sqrt{2}$ factors in front of the matrix elements between core and virtual orbitals, and the factor 2 in front of the Coulomb matrix elements, come from using the *spin-singlet ansatz*, which takes the form

$$|\Phi_a^p\rangle = \frac{1}{\sqrt{2}}\left(\hat{a}_{p+}^\dagger\hat{a}_{a+} + \hat{a}_{p-}^\dagger\hat{a}_{a-}\right)|\Phi_0\rangle. \tag{5.17}$$

Otherwise in this thesis we specify matrix elements using spin orbitals.

We may further define the collected-excitation orbital, in line with Ref. [40], as the sum of all possible excitations associated with a hole in orbital φ_a,

$$|\mathrm{X}_a\rangle = \sum_p\hat{a}_p^\dagger\hat{a}_a|\Phi_0\rangle\alpha_a^p(t), \tag{5.18}$$

or the equivalent references from the vacuum,

$$|\chi_a\rangle = \sum_p \hat{a}_p^\dagger |\varnothing\rangle \alpha_a^p(t). \tag{5.19}$$

5.2 Thomas–Reiche–Kuhn correction

The polarizing energy shifts discussed in Sec. 4.2 are valid only in the case where the configuration space is complete. In Sec. 4 we point out the size-inconsistency problem, which appears for truncated configuration spaces. In Paper VI we observed a similar effect in velocity-gauge TDCIS because the virtual transitions to the doubles space are missing. In velocity-gauge TDCIS, the polarization is therefore unbalanced since the second-order polarization is included in the ground state, but not in the singly-excited states. We adjust for this by postulating an effective potential, which takes care of the polarization due to virtual transitions from the singles to the doubles space and back. The effective potential is formed based on arguments from the TRK sum rule, but adapted to a time-dependent formulation,

$$\hat{V}_{\mathrm{TRK}}^{(\mathrm{S})}(t) = \mathcal{V}_{\mathrm{TRK}}(t)\hat{P}_1 = -\frac{q^2}{2m_{\mathrm{e}}}(\tilde{N}-1)A^2(t)\hat{P}_1, \tag{5.20}$$

where $\tilde{N}$ is the *effective* number of electrons obtained with the TRK sum rule in CIS[7], and $\hat{P}_1$ is a projector onto the singles,

$$\hat{P}_1 = \sum_{ap} |\Phi_a^p\rangle\langle\Phi_a^p|. \tag{5.21}$$

We may add the effective potential in Eq. (5.20) to the Hamiltonian in Eq. (5.3), to obtain

$$\hat{H}_{\mathrm{TRK}} = \hat{H} + \hat{V}_{\mathrm{TRK}}^{(\mathrm{S})}. \tag{5.22}$$

To introduce this correction with minimal computational effort, we identify that the closure of CIS allows us to move the correction from the singles to the noggles by performing the transformation

$$\hat{H}'_{\mathrm{TRK}} = \hat{H}_{\mathrm{TRK}} - \mathcal{V}_{\mathrm{TRK}}(t)\hat{I}_{\mathrm{CIS}}, \tag{5.23}$$

[7] As mentioned, the derivation of TRK in Sec. 4.1 holds only for local potentials, but the exchange part of $\hat{V}_2$ does therefore not commute with the position operator. This means that the commutator relation in Eq. (4.3) can be used only approximately, and TRK can hence only be applied to calculate an approximate number of electrons $\tilde{N}$.

where $\hat{I}_{\mathrm{CIS}} = \hat{P}_0 + \hat{P}_1$. We obtain the following equations of motion in atomic units:

$$i\dot{\alpha}_0 = \sqrt{2}\mathbf{A}(t) \cdot \sum_{ap} \alpha_a^p(t)\langle a|\hat{\mathbf{p}}|p\rangle + \frac{\tilde{N}-1}{2}A^2(t)\alpha_0(t), \tag{5.24a}$$

$$\begin{aligned} i\dot{\alpha}_a^p(t) = (\varepsilon_p - \varepsilon_a)\alpha_a^p(t) + \sum_{bq} \alpha_b^q(t)\left(2\langle bp|r_{12}^{-1}|qa\rangle - \langle bp|r_{12}^{-1}|aq\rangle\right) \\ + \mathbf{A}(t) \cdot \left(\sqrt{2}\alpha_0(t)\langle p|\hat{\mathbf{p}}|a\rangle + \sum_q \alpha_a^q(t)\langle p|\hat{\mathbf{p}}|q\rangle - \sum_b \alpha_b^q(t)\langle b|\hat{\mathbf{p}}|a\rangle\right). \end{aligned} \tag{5.24b}$$

The effective potential that adjusts for the lack of core polarization of excited states to mitigate the size-inconsistency problem in velocity-gauge TDCIS that we discuss here and presented in Paper VI is a different approach than e.g. Sato et al. [42]. They instead deduce a gauge-independent formulation of TDCIS by successively rotating the orbitals in each time step. This enforces a time dependence of not only the expansion coefficients $\{\alpha_0,\ \alpha_a^p\}$, but also the orbitals $\{\Phi_0(t),\ \Phi_a^p(t)\}$, which is necessary in order to obtain gauge-independent observations, see e.g. Ref. [43] for a review on the topic.

6 Photoionization dynamics

In this Section, we introduce photoionization of atoms within CIS. We introduce the methodologies time-dependent surface flux [44, 45] (tSURFF) and its extension infinite-time surface flux [46] (iSURFF), described in Sec. 6.4 and Sec. 6.5, respectively. We describe photoionization of an N-electron atom in CIS by the process of removing an electron from one of the core orbitals and to create a free plane-wave particle described by the Volkov Hamiltonian. We therefore also present the Volkov solutions in Sec. 6.1, which were initially introduced to describe a single relativistic particle under the influence of a sinusoidal field [47], but are today routinely used to model non-relativistic electrons in strong low-frequency laser fields, as will be described in Sec. 6.1.

Much of the dynamics in photoionization experiments in attosecond and free-electron sciences can be described already at the single-electron level, especially for experiments that make use of strong laser fields that dominate the atomic dynamics. We therefore introduce the Keldysh–Faisal–Reiss theory [17, 48, 49] (KFR) in Sec. 6.3. As a preliminary, we introduce S-matrix theory to solve time-dependent scattering problems. This lays the groundwork for many of the methods in this thesis, depending on which Hamiltonian and which scattering states are used. For instance, KFR and tSURFF employ the Volkov states as scattering states. We restrict the discussion to light–matter interactions within the dipole approximation as described in Sec. 3.2, and provide expressions both in velocity gauge and in length gauge. We emphasize that the vector potential refers to the velocity gauge vector potential, $\mathbf{A}(t) = \mathbf{A}^{(\mathrm{vg})}(t)$.

6.1 Volkov solutions for a free particle in a field

The dynamics of a free electron under the influence of an external electric field is described by the Volkov Hamiltonian. This Hamiltonian is in atomic units given by

$$\hat{H}^{(\mathrm{V})}(t) = \begin{cases} \frac{\hat{\mathbf{p}}^2}{2} + \mathbf{A}(t)\cdot\hat{\mathbf{p}} + \frac{A^2(t)}{2} & \text{velocity gauge,} \\ \frac{\hat{\mathbf{p}}^2}{2} + \mathbf{E}(t)\cdot\hat{\mathbf{r}} & \text{length gauge.} \end{cases} \tag{6.1}$$

The solutions to the TDSE, Eq. (2.1), with the Volkov Hamiltonian is given by the Volkov state vector. Since the electron is free from any confining potential it takes the form of a plane wave,

$$|\chi_{\mathbf{k}}(\mathbf{r},t)\rangle = |\mathbf{k}\rangle \mathrm{e}^{-\mathrm{i}\mathcal{S}[\mathbf{k},t]}, \tag{6.2}$$

where the plane-wave wavefunction is given by

$$\langle \mathbf{r}|\mathbf{k}\rangle = \varphi_{\mathbf{k}}(\mathbf{r}) = \frac{\exp(\mathrm{i}\mathbf{k}\cdot\mathbf{r})}{(2\pi)^{-3/2}}. \tag{6.3}$$

The denominator ensures that the plane waves, and therefore also the Volkov waves, are δ-normalized,

$$\int \mathrm{d}^3 r\ \chi^*_{\mathbf{k}'}\chi_{\mathbf{k}} = \delta(\mathbf{k}-\mathbf{k}'). \tag{6.4}$$

As the particle propagates in the presence of the oscillating field it acquires a phase $\mathcal{S}[\mathbf{k},t]$, which depends on the kinetic momentum of the electron, and time. In velocity gauge, the acquired phase is given by the functional

$$\mathcal{S}[\mathbf{k},t] = \int_{t_{\mathrm{ref}}}^{t} \mathrm{d}t'\ \frac{(\mathbf{k}+\mathbf{A}(t'))^2}{2}. \tag{6.5}$$

The corresponding expression for the Volkov phase in length gauge can be retrieved by applying a gauge transformation, using Eq. (3.11) with the transformation function $F = -\mathbf{A}(t)\cdot\mathbf{r}$, to the Volkov state derived from Eq. (6.2). This yields a Volkov phase of the form

$$\mathcal{S}[\mathbf{k},\mathbf{r},t] = \int_{t_{\mathrm{ref}}}^{t} \mathrm{d}t'\ \left[\frac{(\mathbf{k}+\mathbf{A}(t'))^2}{2} - \mathbf{r}\cdot\mathbf{E}(t')\right]. \tag{6.6}$$

The reference time t_{ref} can be chosen arbitrarily, as it only yields a phase term that is insignificant to any physical observables. We identify the expressions for the phase as the *action integral* of an electron that propagates in a field,

$$\mathcal{S} = \int^{t} \mathrm{d}t'\ \mathcal{L}(t'), \tag{6.7}$$

where $\mathcal{L}$ is the Lagrangian corresponding to a free particle in a field, given by

$$\mathcal{L} = \begin{cases} \frac{(\mathbf{k}+\mathbf{A}(t))^2}{2} & \text{velocity gauge,} \\ \frac{(\mathbf{k}+\mathbf{A}(t))^2}{2} - \mathbf{r}\cdot\mathbf{E}(t) & \text{length gauge.} \end{cases} \tag{6.8}$$

An equivalent formulation of the Volkov waves is to write the plane waves with the kinetic momentum instead of the canonical momentum. The dependence on position is then moved out of the action integral, so that the treatment of the Volkov phase is common in both choices of gauge,

$$\chi_{\mathbf{k}}(\mathbf{r},t) = \frac{\mathrm{e}^{\mathrm{i}\tilde{\mathbf{k}}\cdot\mathbf{r}}}{(2\pi)^{3/2}}\mathrm{e}^{-\frac{\mathrm{i}}{2}\int^t \mathrm{d}t'\ (\mathbf{k}+\mathbf{A}(t'))^2}, \tag{6.9}$$

where

$$\tilde{\mathbf{k}} = \begin{cases} \mathbf{k} & \text{velocity gauge,} \\ \mathbf{k}+\mathbf{A}(t) & \text{length gauge.} \end{cases} \tag{6.10}$$

Further, the plane waves appearing in Eq. (6.2) are often evaluated in terms of the multipole expansion,

$$\mathrm{e}^{\mathrm{i}\mathbf{k}\cdot\mathbf{r}} = 4\pi\sum_{\ell=0}^{\infty}\mathrm{i}^{\ell}j_{\ell}(kr)\sum_{m=-\ell}^{\ell}Y^*_{\ell m}(\Omega_{\mathbf{r}})Y_{\ell m}(\Omega_{\mathbf{k}}), \tag{6.11}$$

where $j_\ell(kr)$ is the ℓth order spherical Bessel function evaluated at $z = kr$ and $j'(z)$ is the derivative with respect to z.

When discussing the tSURFF method in Sec. 6.4, we will make use of the Volkov state and Volkov Hamiltonian expressed in second quantization. The Volkov state is retrieved by creation of a plane wave,

$$|\chi_{\mathbf{k}}(t)\rangle = |\mathbf{k}\rangle\mathrm{e}^{-\mathrm{i}\mathcal{S}(\mathbf{k},t)} = \hat{a}^\dagger_{\mathbf{k}}|\varnothing\rangle\mathrm{e}^{-\mathrm{i}\mathcal{S}(\mathbf{k},t)}, \tag{6.12}$$

with an acquired phase given by the Volkov action, here expressed in velocity gauge. The plane waves are not orthonormal to the states in the CIS basis, and the usual anticommutation relations found for the core and virtual orbitals do therefore not hold. We may express the plane-wave creation operator in terms of the CIS basis as

$$\hat{a}^\dagger_{\mathbf{k}} = \sum_i \langle i|\mathbf{k}\rangle\hat{a}^\dagger_i, \tag{6.13}$$

and the corresponding anticommutation relations are given by

$$\{\hat{a}^\dagger_{\mathbf{k}},\ \hat{a}^\dagger_i\} = 0, \tag{6.14a}$$
$$\{\hat{a}_{\mathbf{k}},\ \hat{a}_i\} = 0, \tag{6.14b}$$
$$\{\hat{a}^\dagger_{\mathbf{k}},\ \hat{a}_i\} = \langle i|\mathbf{k}\rangle. \tag{6.14c}$$

When the Volkov state is created by removing a core electron from a reference state to create a plane wave, we account for this by writing the many-body equivalent of Eq. (6.12),

$$|\chi_{\mathbf{k},a}(t)\rangle = \hat{a}_{\mathbf{k}}^{\dagger}\hat{a}_a|\Phi_0\rangle \mathrm{e}^{-\mathrm{i}\mathcal{S}_a(\mathbf{k},t)}, \tag{6.15}$$

where

$$\exp[-\mathrm{i}\mathcal{S}_a(\mathbf{k},t)] = \exp[-\mathrm{i}\mathcal{S}(\mathbf{k},t)]\exp[-\mathrm{i}\varepsilon_a t]. \tag{6.16}$$

The dynamics are hence ruled by the *adjusted* Volkov Hamiltonian, cf. Ref. [50],

$$\hat{H}_a^{(\mathrm{V})} = \hat{H}^{(\mathrm{V})} - \varepsilon_a. \tag{6.17}$$

6.2 Time-dependent scattering theory

S-matrix theory is introduced to solve time-dependent scattering problems where the Hamiltonian can be split into two parts: one known reference Hamiltonian, $\hat{H}_0$, and one interaction Hamiltonian, $\hat{V}^{(\mathrm{int})}$, which gives rise to transitions. We discuss the S-matrix elements, which give the exact transition matrix elements in photoionization of atoms in the single-particle case. The reference Hamiltonian may have a time dependence, but all the external interactions need to be contained in the interaction Hamiltonian. We will ultimately deal with an atomic system interacting with an external light field, and hence the reference Hamiltonian will be the N-body atomic Hamiltonian in Eq. (2.2). However, all the photoelectron methods presented in this thesis reduce to single-particle expressions, where the S-matrix formalism serves as a starting point. The following derivation of the S matrix follows closely that of Ref. [23].

Let Ψ denote the exact solution to the TDSE in Eq. (2.1) with the full Hamiltonian in Eq. (3.4), and let Φ denote the exact solution to TDSE with the noninteracting Hamiltonian $\hat{H}_0$,

$$\mathrm{i}\hbar\frac{\partial}{\partial t}|\Phi(t)\rangle = \hat{H}_0|\Phi(t)\rangle. \tag{6.18}$$

For a finite field, the light–matter interaction will asymptotically vanish, and the full Hamiltonian will therefore approach the noninteracting Hamitlonian,

$$\lim_{t\to\pm\infty}\hat{H} = \hat{H}_0. \tag{6.19}$$

The asymptotic behavior of the solution to TDSE with the total Hamiltonian is therefore that they attain the noninteracting wavefunction in the beginning and end of time,

$$\lim_{t\to-\infty}|\Psi_{\mathrm{i}}^{(+)}(t)\rangle = |\Phi_{\mathrm{i}}\rangle, \tag{6.20a}$$

$$\lim_{t\to+\infty}|\Psi_{\mathrm{f}}^{(-)}(t)\rangle = |\Phi_{\mathrm{f}}\rangle. \tag{6.20b}$$

The wavefunction $\Psi_{\mathrm{i}}^{(+)}$ is therefore initially noninteracting, and $\Psi_{\mathrm{f}}^{(-)}$ is noninteracting at the end of time. The transition matrix elements, defined as the overlap between the asymptotic solutions $\Psi_{\mathrm{i/f}}^{(\pm)}(t)$ and the noninteracting solution $\Phi(t)$, are denoted the S-matrix elements. These S-matrix elements are given by

$$S_{\mathrm{fi}} = \lim_{t\to\infty} \left\langle \Phi_{\mathrm{f}}(t) \middle| \Psi_{\mathrm{i}}^{(+)}(t) \right\rangle, \tag{6.21}$$

for the forward time form and

$$S_{\mathrm{fi}} = \lim_{t\to-\infty} \left\langle \Psi_{\mathrm{f}}^{(-)}(t) \middle| \Phi_{\mathrm{i}}(t) \right\rangle, \tag{6.22}$$

for reversed time form.

The asymptotic S-matrix elements can be retrieved by introducing the Green's functions associated with TDSE with the noninteracting Hamiltonian $\hat{H}_0$, cf. Ref. [23],

$$G^{(+)}(t,t_0)|\Phi(t_0)\rangle = -\mathrm{i}\theta(t-t_0)|\Phi(t)\rangle, \tag{6.23a}$$
$$G^{(-)}(t,t_0)|\Phi(t_0)\rangle = \mathrm{i}\theta(t_0-t)|\Phi(t)\rangle, \tag{6.23b}$$

where $\theta(t)$ is the Heaviside step function. The operator in Eq. (6.23a) propagates the solution forward in time while the operator in Eq. (6.23b) propagates the solution backwards in time. Both these functions satisfy the equation

$$\left(\mathrm{i}\hbar\frac{\partial}{\partial t} - \hat{H}_0\right) G^{(\pm)}(t,t_0) = \delta(t-t_0), \tag{6.24}$$

where $\delta(t-t_0)$ is the Dirac delta function centered about t_0. The solution to Eq. (6.18) is now simultaneously solved by the integral equation, see for instance Ref. [51],

$$|\Psi^{(\pm)}(t)\rangle = |\Phi(t)\rangle + \int_{-\infty}^{t} \mathrm{d}t'\, G^{(\pm)}(t,t')\hat{V}^{(\mathrm{int})}(t')|\Psi^{(\pm)}(t')\rangle. \tag{6.25}$$

By substituting this expression into the expression for the S-matrix elements, for instance Eq. (6.21), we obtain

$$S_{\mathrm{fi}} = \lim_{t\to\infty} \left\{ \langle\Phi_{\mathrm{f}}|\Phi_{\mathrm{i}}\rangle + \int_{-\infty}^{t} \mathrm{d}t' \left\langle \Phi_{\mathrm{f}}(t)|G^{(+)}(t,t')\hat{V}^{(\mathrm{int})}(t')|\Psi_{\mathrm{i}}^{(+)}(t') \right\rangle \right\}. \tag{6.26}$$

The first term does not lead to transitions and is only nonzero if the initial and final states are the same,

$$S_{\mathrm{fi}} = \lim_{t\to\infty} \langle\Phi_{\mathrm{f}}|\Phi_{\mathrm{i}}\rangle = \delta(\Phi_{\mathrm{f}},\Phi_{\mathrm{i}}) := 1_{\mathrm{fi}}. \tag{6.27}$$

Hence, by substituting the expression for the Green's function in Eq. (6.23a) into Eq. (6.26), we obtain

$$(S-1)_{\mathrm{fi}} = -\mathrm{i}\int_{-\infty}^{\infty} \mathrm{d}t \left\langle \Phi_{\mathrm{f}}(t) \middle| \hat{V}^{(\mathrm{int})}(t) \middle| \Psi_{\mathrm{i}}^{(+)}(t) \right\rangle, \tag{6.28}$$

and likewise for the reverse-time solution,

$$(S-1)_{\mathrm{fi}} = -\mathrm{i}\int_{-\infty}^{\infty} \mathrm{d}t \, \left\langle \Psi_{\mathrm{f}}^{(-)}(t) \middle| \hat{V}^{(\mathrm{int})}(t) \middle| \Phi_{\mathrm{i}}(t) \right\rangle . \tag{6.29}$$

The expression in Eq. (6.29) is now the exact expression that describes an atom initially in the state $|\Phi_{\mathrm{i}}\rangle$, which through some interaction reaches an asymptotic state $|\Psi_{\mathrm{f}}^{(-)}\rangle$. The exact expression are rarely used since the asymptotic states $|\Psi_{\mathrm{f}}^{(\pm)}\rangle$ are difficult to obtain. We will in the following approximate the asymptotic state $|\Psi_{\mathrm{f}}^{(-)}\rangle$ with the Volkov state introduced in Eq. (6.12), or by the adjusted Volkov state created by first removing an electron from an atom, as described in Eq. (6.15).

6.3 Keldysh–Faisal–Reiss theory

The theories developed independently by Keldysh [17], Faisal [48] and Reiss [49] are used for non-perturbative treatment of light–matter interactions between a single atom with one electron in an external field. The three theories differ in the choice of gauge; Keldysh [17] uses length gauge, whereas Faisal [48] and Reiss [49] use velocity gauge. The Coulomb potential is considered weak compared to the potential due to the electromagnetic field, and the electron will therefore approximately be described by a Volkov wave when far from the nucleus, see Ref [32],

$$\lim_{t\to\infty} \langle \Psi_f^{(-)} | \hat{U}(t,t_0) = \langle \chi_{\mathbf{k}}(t)|. \tag{6.30}$$

Initially however, the electron is bound due to the Coulomb potential in the atom with nuclear charge Z and is described by the scaled hydrogenic $1s$ orbital,

$$|a\rangle = |\phi_0(\mathbf{r})\rangle \mathrm{e}^{-\mathrm{i}\varepsilon_a t}, \tag{6.31}$$

with $\varepsilon_a = -I_p < 0$, where I_p is the binding energy. By introducing these assumptions into the S-matrix expression in Eq. (6.29), we obtain the KFR expression

$$(S-1)_{\mathrm{fi}} \approx c_{\mathbf{k},a}(t) = -\mathrm{i}\int^{t} \mathrm{d}t' \, \langle \chi_{\mathbf{k}} | \hat{V}^{(\mathrm{int})}(t') | \varphi_0(\mathbf{r})\rangle \mathrm{e}^{-i\varepsilon_a t'}. \tag{6.32}$$

The electron is therefore bound for $t < t'$ at which point it is ejected and freed. This approximation is suitable for short-range potentials, but can though be used qualitatively to study photoionization of atoms in presence of the Coulomb potential, which is a long-range potential. The KFR theory presented here does not take into account the possibility of the rescattering mechanism, cf. [52], which allows the photoelectron to interact with the ion and is relevant in above-threshold ionization, discussed in Sec. 9. Excited bound states are further not included in KFR and it is not possible to describe e.g. resonant photoionization.

As we showed in Paper IV, KFR can therefore not be used to model photoionization of a Rabi-oscillating atom. We mention that corrections to the non-interacting free electron is discussed by Reiss [49], where a perturbation expansion in the Coulomb potential is used to obtain an expression, which somewhat takes into account the effect of a long-range potential.

In our implemented form of KFR, we evaluate the integral directly as

$$c_{\mathbf{k},a}(t) = -i\langle \mathbf{k}|\phi_0\rangle \int^t \mathrm{d}t' \left(kA(t')\cos\theta_k + \frac{A^2(t')}{2} \right) \mathrm{e}^{\mathrm{i}\mathcal{S}_a(\mathbf{k},t')}, \tag{6.33}$$

where $\mathcal{S}_a$ is the adjusted Volkov action from Eq. (6.16), and θ_k is the angle of emission measured from the polarization axis of the external field. The overlap is calculated analytically to

$$\langle \mathbf{k}|\phi_0\rangle = \frac{2^{3/2}}{\pi} \frac{Z^{5/2}}{(Z^2+k^2)^2}. \tag{6.34}$$

In experiments where the photoelectron is ejected with high kinetic energy along, or antiparallel to, the polarization axis, the first term of Eq. (6.33) is dominant. For slow photoelectrons, or for photoelectrons measured perpendicular to the polarization axis, the isotropic $A^2(t)/2$ term is important.

6.4 Time-Dependent Surface-Flux method

In this section, we discuss the tSURFF method [44, 45] that is used to calculate the outgoing flux of photoelectrons in a photoionization or photodetachment experiment. The flux of the photoelectrons is then used to calculate the photoelectron spectrum to gain quantitative information on the photoelectron's momentum and angular distributions, as well as the ionic degrees of freedom. The obtained photoelectron spectrum is fully differential, which means that all quantum numbers are resolved[8]. Information on photoionization dynamics can also be extracted by projecting the wavefunction onto scattering states, as done in e.g. Ref. [53], where single and double ionization amplitudes are extracted. Contrary to a direct calculation of the photoelectron spectrum by projection onto scattering states, tSURFF does not require the full wavefunction to be kept inside the computational volume when the pulse is turned on. When the flux is measured instead, the radial extent of the computational grid can be kept to a minimum, provided that the outgoing wave packet is damped with artificial boundary conditions, e.g. by using complex absorbing potentials [54] or exterior complex scaling [55–57] (ECS). We choose ECS, and discuss briefly the choice of parameters in Sec. 6.7.

[8]Spin dynamics is not considered, as implied by the singlet ansatz in Eq. (5.17), but the tSURFF equations we give here are expressed for a general treatment of spin orbitals.

Assumptions of the tSURFF method

In the tSURFF method, we make the two assumptions that

1. the wavefunction can be separated into a bound part and a scattered part after a finite time T,
$$\Psi(\mathbf{r}, T) = \Psi_{\mathrm{b}}(\mathbf{r}, T) + \Psi_{\mathrm{s}}(\mathbf{r}, T). \tag{6.35}$$
This is equivalent to assume that part of the electron density is freed from the attracting nucleus and electronic repulsion and that we may separate the photoelectron degrees of freedom from those of the excited neutral atom.

2. outside a certain radial distance r_c, there is no overlap between the bound and the scattered wavefunctions, given by
$$\Psi_{\mathrm{b}}(\mathbf{r}, T) = 0, \tag{6.36a}$$
$$\Psi_{\mathrm{s}}(\mathbf{r}, T) = \int \mathrm{d}\mathbf{k}\, b(\mathbf{k}) \psi_{\mathbf{k}}(\mathbf{r}), \tag{6.36b}$$
for some $r = |\mathbf{r}| > r_c$. This requires r_c to be large enough such that the relevant bound states are accommodated.

The finite time T must be chosen such that the full wave packet has passed through the sphere at r_c. This may require the time propagation to continue long after the pulse has ended in experiments that involve bound-state resonances, in which long-lived Rydberg states are populated [44]. If high Rydberg states are involved, with large radial extent of $\sim n^2$, the requirement of a large r_c and a large T may pose a problem, especially if low-kinetic momentum electrons are of interest. Since we dampen the outgoing wavefunction using ECS, we must also make sure that no part of the wavefunction re-enters the inner region after having passed over the radial distance r_c into the damping region. This is assured by moving the dampening region that starts at r_0 further out to leave room for the quiver motion of the electron. As a rule of thumb, the dampening region is typically set to be larger than two times the classical excursion in Eq. (1.4), which in velocity gauge is $\alpha = A_0/\omega$ in atomic units, such that $r_c < r_0 < r_{\mathrm{box}}$, where r_{box} is the radial extent of the computational volume. In Fig. 8 a typical radial grid is shown together with a bound orbital. The surface radius r_c is set such that the highest Rydberg state of interest is numerical zero at r_c.

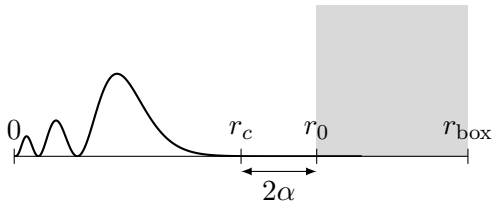

Figure 8: Typical computational grid for a tSURFF calculation compared to the probability density of some bound state wavefunction (as an example the $4s$ wavefunction in hydrogen). The surface radius r_c is chosen outside the bound wavefunctions of interest, and the dampening region, illustrated as a gray area, starts at r_0. The full radial extent of the computational volume is specified by r_{box}.

Since we assume that the initially bound electron is free outside r_c, its dynamics are completely driven by the electric field and is hence ruled by the adjusted Volkov Hamiltonian in Eq. (6.17). For the nuclear Coulomb potential however, which scales as $1/r$, this is not the case as the Volkov solutions do not correspond to the correct scattering states. This error is more prominent for low-kinetic energy photoelectrons, as discussed in Sec. 6.7. That the photoelectron part of the scattering state is described by the Volkov state is similar to the assumption in KFR, with the difference that there we impose this condition immediately after the photoexcitation as opposed to in tSURFF where this condition is assumed to hold at any radial distance greater than r_c.

Retrieving the spectal amplitudes

We now seek to analyse the spectral amplitudes in Eq. (6.36b), resolved on the ionization channel a, evaluated at a finite time T, which approximates the S-matrix amplitudes,

$$(S-1)_{\text{fi}} \approx b_a(\mathbf{k},T) = \langle \chi_{\mathbf{k},a}(\mathbf{k},T)|\hat{\Theta}(r_c)|\Psi(\mathbf{r},T)\rangle. \tag{6.37}$$

The spectral amplitudes depend on the photoelectron's attained momentum and ejection angle, as well as the hole in orbital φ_a of the target. The final state is given by removing an electron from one of the core orbitals and successively creating a Volkov plane wave, as given in Eq. (6.15). The Heaviside operator is a one-body radial operator of the form

$$\hat{\Theta}(r_c) = \sum_{ij}\{\hat{a}_i^\dagger \hat{a}_j\}\langle i|\hat{\theta}(r_c)|j\rangle \to \sum_{pq}\hat{a}_p^\dagger \hat{a}_q \langle p|\hat{\theta}(r_c)|q\rangle \tag{6.38}$$

that is introduced since the scattered photoelectron is assumed to have no overlap inside the sphere of radius r_c, in accordance with Eq. (6.35). Since the core orbitals have weak support outside r_c, and therefore contribute little for large r_c, the sum in the Heaviside operator runs over the virtual orbitals. The one-body matrix element of the Heaviside operator is given by the overlap in the outer region only,

$$\langle i|\hat{\theta}(r_c)|j\rangle \to \int_{r>r_c} \mathrm{d}\mathbf{r}\ \varphi_p(\mathbf{r})\varphi_q(\mathbf{r}), \tag{6.39}$$

which we refer to as the *outerlap*. The equations of motion for the spectral amplitudes in Eq. (6.37) may then be retrieved as

$$\begin{aligned} -\mathrm{i}\frac{\partial}{\partial t} b_a(\mathbf{k},t) &= -\mathrm{i}\frac{\partial}{\partial t}\langle\chi_{\mathbf{k},a}|\hat{\Theta}(r_c)|\Psi\rangle \\ &= \langle\chi_{\mathbf{k},a}|\hat{H}_a^{(\mathrm{V})}(t)\hat{\Theta}(r_c)|\Psi\rangle - \langle\chi_{\mathbf{k},a}|\hat{\Theta}(r_c)\hat{H}(t)|\Psi\rangle. \end{aligned} \tag{6.40}$$

These two matrix elements are derived in Apdx. A and are explicitly given below for the case when the system is described by the TDCIS Hamiltonian in Eq. (5.7). For the mean-field Hamiltonian, $\hat{H}_0^{(\mathrm{HF})}$, we evaluate the matrix element to

$$\langle\chi_{\mathbf{k},a}|\hat{\Theta}\hat{H}_0^{(\mathrm{HF})}|\Psi\rangle = \sum_q \left[\langle\mathbf{k}|\hat{\theta}\hat{h}^{(\mathrm{HF})}|q\rangle + \left(E_0^{(\mathrm{HF})} - \varepsilon_a\right)\langle\mathbf{k}|\hat{\theta}|q\rangle\right] \mathrm{e}^{\mathrm{i}\mathcal{S}_a(\mathbf{k},t)}\alpha_a^q(t), \tag{6.41}$$

which can be compared to the mean-field matrix element between two singly-excited states in Eq. (5.9).

For the Coulomb potentials $\hat{V} = \hat{V}_0 + \hat{V}_2$, and the light–matter-interaction potential $\hat{V}^{(\mathrm{int})}$, we obtain results similar to Eq. (5.10) for $\hat{V}_0$ and $\hat{V}_2$, and a coupling between two core orbitals due to $\hat{V}^{(\mathrm{int})}$,

$$\langle\chi_{\mathbf{k},a}|\hat{\Theta}\hat{V}_0|\Psi\rangle = E_1^{(\mathrm{HF})}\sum_q \langle\mathbf{k}|\hat{\theta}|q\rangle \mathrm{e}^{\mathrm{i}\mathcal{S}_a(\mathbf{k},t)}\alpha_a^q(t), \tag{6.42a}$$

$$\langle\chi_{\mathbf{k},a}|\hat{\Theta}\hat{V}^{(\mathrm{int})}|\Psi\rangle = \sum_q \left(\langle\mathbf{k}|\hat{\theta}\hat{v}^{(\mathrm{int})}|q\rangle\alpha_a^q(t) - \sum_b \langle\mathbf{k}|\hat{\theta}|q\rangle\langle b|\hat{v}^{(\mathrm{int})}|a\rangle\alpha_b^q(t)\right)\mathrm{e}^{\mathrm{i}\mathcal{S}_a(\mathbf{k},t)}, \tag{6.42b}$$

$$\langle\chi_{\mathbf{k},a}|\hat{\Theta}\hat{V}_2|\Psi\rangle = \sum_{b,qt}\langle\mathbf{k}|\hat{\theta}|t\rangle(\langle bt|r_{12}^{-1}|qa\rangle - \langle bt|r_{12}^{-1}|aq\rangle)\mathrm{e}^{\mathrm{i}\mathcal{S}_a(\mathbf{k},t)}\alpha_b^q(t). \tag{6.42c}$$

By combining Eq. (6.41)–(6.42) and subtracting the HF energy $E^{(\mathrm{HF})}$, we obtain for the second term on the right-hand side of Eq. (6.40) the expression

$$\langle\chi_{\mathbf{k},a}|\hat{\Theta}\hat{H}|\Psi\rangle = \sum_q \Bigg[\left(\langle\mathbf{k}|\hat{\theta}\hat{h}^{(\mathrm{HF})}|q\rangle - \varepsilon_a\langle\mathbf{k}|\hat{\theta}|q\rangle\right)\alpha_a^q(t) \tag{6.43a}$$

$$+ \sum_{b,t}\langle\mathbf{k}|\hat{\theta}|t\rangle\left(\langle bt|r_{12}^{-1}|qa\rangle - \langle bt|r_{12}^{-1}|aq\rangle\right)\alpha_b^q(t) \tag{6.43b}$$

$$+ \langle\mathbf{k}|\hat{\theta}\hat{v}^{(\mathrm{int})}|q\rangle\alpha_a^q(t) - \sum_b\langle\mathbf{k}|\hat{\theta}|q\rangle\langle b|\hat{v}^{(\mathrm{int})}|a\rangle\alpha_b^q(t)\Bigg]\mathrm{e}^{\mathrm{i}\mathcal{S}_a(\mathbf{k},t)}. \tag{6.43c}$$

The one-body HF Hamiltonian can be approximated by imposing the assumptions above. For a large r_c, the first term on the right-hand side of Eq. (6.43a) is approximatively given by

the one-body kinetic operator, and the two-body Coulomb potential in Eq. (6.43b) tends to zero. The matrix element of Eq. (6.43) is therefore approximated by

$$\begin{aligned}\langle\chi_{\mathbf{k},a}|\hat{\Theta}\hat{H}|\Psi\rangle \approx \sum_q \Bigg[&\Big(\langle\mathbf{k}|\hat{\theta}\hat{t}|q\rangle - \varepsilon_a\langle\mathbf{k}|\hat{\theta}|q\rangle + \langle\mathbf{k}|\hat{\theta}\hat{v}^{(\mathrm{int})}|q\rangle\Big)\,\alpha_a^q(t) \\ &- \sum_b \langle\mathbf{k}|\hat{\theta}|q\rangle\langle b|\hat{v}^{(\mathrm{int})}|a\rangle\alpha_b^q(t)\Bigg] \mathrm{e}^{\mathrm{i}\mathcal{S}_a(\mathbf{k},t)}.\end{aligned} \tag{6.44}$$

We note however that the interelectronic Coulomb interaction inside r_c is kept in Eq. (24) in Ref. [45]. Moreover, the first term in the right-hand side of Eq. (6.40) gives

$$\langle\chi_{\mathbf{k},a}|\hat{H}_a^{(\mathrm{V})}\hat{\Theta}|\Psi\rangle = \sum_q \Big(\langle\mathbf{k}|\hat{t}\hat{\theta}|q\rangle + \langle\mathbf{k}|\hat{v}^{(\mathrm{int})}\hat{\theta}|q\rangle - \varepsilon_a\langle\mathbf{k}|\hat{\theta}|q\rangle\Big)\,\mathrm{e}^{\mathrm{i}\mathcal{S}_a(\mathbf{k},t)}\alpha_a^q(t). \tag{6.45}$$

Combining Eq. (6.44) and Eq. (6.45), we get in total that the spectral amplitudes are obtained by a coupled set of single-electron problems,

$$\begin{aligned}-\mathrm{i}\frac{\partial}{\partial t}b_a(\mathbf{k},t) = \sum_q \Bigg(&\langle\mathbf{k}|[\hat{t}+\hat{v}^{(\mathrm{int})},\ \hat{\theta}]|q\rangle\alpha_a^q(t) \\ &- \sum_b \langle\mathbf{k}|\hat{\theta}|q\rangle\langle b|\hat{v}^{(\mathrm{int})}|a\rangle\alpha_b^q(t)\Bigg)\mathrm{e}^{\mathrm{i}\mathcal{S}_a(\mathbf{k},t)},\end{aligned} \tag{6.46}$$

where the ionization channels are coupled by the external field [50, 58]. In Sec. 6.7, we present the numerical procedure to solve Eq. (6.46) for the spectral amplitudes $b_a(\mathbf{k},t)$.

Single-channel expression

For the special case of uncoupled ion channels, the spectral amplitudes can be readily obtained by direct integration,

$$b_a(\mathbf{k},t) = \mathrm{i}\int^t \mathrm{d}t'\ s_a(\mathbf{k},t'). \tag{6.47}$$

where, for brevity, we denote the single-channel surface amplitudes as

$$s_a(\mathbf{k},t) = \langle\mathbf{k}|[\hat{t}+\hat{v}^{(\mathrm{int})},\ \hat{\theta}(r_c)]|\chi_a\rangle\mathrm{e}^{\mathrm{i}\mathcal{S}_a(\mathbf{k},t)}, \tag{6.48}$$

and the virtual orbitals are collected according to Eq. (5.19).

To evaluate the surface commutator in Eq. (6.48) we use the fact that the Heaviside operator is a function of the radial coordinate only, and therefore the angular part of the Hamiltonian

commutes, $[\hat{h}_\Omega^{(\mathrm{V})}, \hat{\theta}] = 0$. This yields

$$[\hat{h}^{(\mathrm{V})}(t),\ \hat{\theta}(r_c)] = \left[\frac{\hat{p}_r^2}{2}, \hat{\theta}(r_c)\right] + [\hat{v}^{(\mathrm{int})} \cdot \hat{e}_r,\ \hat{\theta}(r_c)]. \tag{6.49}$$

The first commutator is common to both choices of gauge, length or velocity. It amounts to the divergent electron flux through the surface without interaction with the field, and evaluates to

$$\left[\frac{\hat{p}_r^2}{2},\ \hat{\theta}(r_c)\right] = -\frac{1}{2} r^{-2} \frac{\partial}{\partial r} r^2 \delta(r - r_c) - \frac{1}{2}\delta(r - r_c)\frac{\partial}{\partial r}. \tag{6.50}$$

The second commutator describes on the other hand the electron flux due to the interaction with the field and depends therefore on the choice of gauge. In both gauges, this term is given by

$$[\hat{v}^{(\mathrm{int})} \cdot \hat{e}_r,\ \hat{\theta}(r_c)] = \begin{cases} -\mathrm{i}A_r(t)\delta(r - r_c) & \text{velocity gauge,} \\ 0 & \text{length gauge,} \end{cases} \tag{6.51}$$

since $[\hat{p}_r,\ \hat{\theta}(r_c)] = -\mathrm{i}\delta(r - r_c)$ and $[\hat{r},\ \hat{\theta}(r_c)] = 0$. It is not surprising that the length-gauge interaction term does not contribute since it lacks a divergence term. Likewise, the $\hat{V}_2^{(\mathrm{int})}$ in velocity gauge commutes with the Heaviside operator and does therefore not contribute. We arrive at the expression, for the single-channel surface amplitudes in Eq. (6.48),

$$\mathrm{i}s_a(\mathbf{k}, t) = \frac{\mathrm{i}}{2} r_c^2 \int \mathrm{d}\Omega \left(\frac{\partial \varphi_{\mathbf{k}}^*}{\partial r}\chi_a - \varphi_{\mathbf{k}}^* \frac{\partial \chi_a}{\partial r} + 2\mathrm{i}A_r(t)\varphi_{\mathbf{k}}^* \chi_a \right) \mathrm{e}^{\mathrm{i}\mathcal{S}_a(\mathbf{k},t)}, \tag{6.52}$$

where the last term disappears in length gauge in accordance with Eq. (6.51), and the fact that the vector potential is zero in length gauge anyways. There is a striking similarity between the integrand in Eq. (6.52) and the expression for the probability current in presence of a classical electromagnetic field, see e.g. Ref. [59],

$$j_r = \frac{\mathrm{i}}{2}\left(\frac{\partial \Psi^*}{\partial r}\Psi - \Psi^* \frac{\partial \Psi}{\partial r} + 2iA_r(t)|\Psi|^2 \right). \tag{6.53}$$

In fact, this shows that the spectral amplitudes are the accumulated probability current for a specific linear momentum k and a hole in the core orbital φ_a, through a solid angle $\mathrm{d}\Omega$, passing through the sphere with radius r_c under the assumption that the wavefunction is described by the Volkov waves at distances $r \geq r_c$. The introduction of the Heaviside operator in Eq. (6.37) hence reduces the volume integral to a surface integral that we will solve analytically, and a time integral that we will solve numerically.

To arrive at the final implemented form of $s_a(\mathbf{k}, t)$, we substitute the expression for the Volkov wave in Eq. (6.9), together with the multipole expansion in Eq. (6.11), and expand

the collected-excitation orbital χ_a in spherical coordinates

$$\chi_a(\mathbf{r},t) = \frac{1}{r}\sum_\ell \psi_{\ell m_a}(r,t) Y_{\ell m_a}(\Omega_\mathbf{r}). \tag{6.54}$$

From the integrand in Eq. (6.52) it is seen that the single-channel surface amplitudes can be divided into a field-free term and a term that depends on the field,

$$s_a(\mathbf{k},t) = \frac{1}{2\pi} e^{i\mathcal{S}_a(\mathbf{k},t)} \sum_\ell \left(s^{(0)}_{a,\ell}(\tilde{\mathbf{k}},t) + s^{(\text{field})}_{a,\ell}(\tilde{\mathbf{k}},t) \right), \tag{6.55}$$

where the latter term is zero for length gauge according to Eq. (6.51). Here we have made use of $\tilde{\mathbf{k}}$ from Eq. (6.10) to write the expression on a common form between the two gauges. We consider linearly polarized light along the z-axis, $\mathbf{A}(t) = (0,0,A_z(t))$, which means that the magnetic quantum number is conserved, $m = m_a$. The two terms that constitute the single-channel surface amplitudes are given by

$$\begin{aligned} s^{(0)}_{a,\ell}(\tilde{\mathbf{k}},t) &= (-i)^\ell \Big[(\tilde{k} r_c j'_\ell(\tilde{k} r_c) + j_\ell(\tilde{k} r_c)) \psi^a_{\ell m_a}(r_c,t) \\ &\quad - r_c j_\ell(\tilde{k} r_c) \psi^{a'}_{\ell m_a}(r_c,t) \Big] Y_{\ell m_a}(\Omega_{\tilde{\mathbf{k}}}), \end{aligned} \tag{6.56a}$$

$$\begin{aligned} s^{\text{field}}_{a,\ell}(\tilde{\mathbf{k}},t) &= -i 2 r_c A_z(t) \psi^a_{\ell m_a}(r_c,t) \sum_{\ell'=\ell\pm1} (-i)^{\ell'} j_{\ell'}(\tilde{k} r_c) Y_{\ell m_a}(\Omega_{\tilde{\mathbf{k}}}) \\ &\quad \times \sqrt{\frac{3}{4\pi}} (-1)^{m_a} \sqrt{(2\ell'+1)(2\ell+1)} \begin{pmatrix} \ell' & 1 & \ell \\ -m_a & 0 & m_a \end{pmatrix} \begin{pmatrix} \ell' & 1 & \ell \\ 0 & 0 & 0 \end{pmatrix}. \end{aligned} \tag{6.56b}$$

In the single-channel case in the reduced velocity gauge, this means that the spectral am-

plitudes can be retrieved directly by the integral[9]

$$
\begin{aligned}
b_a(\mathbf{k},T) = \mathrm{i}\sqrt{\frac{2}{\pi}}\int^{T}\mathrm{d}t\,\exp\left[\mathrm{i}\int_{t_{\mathrm{ref}}}^{t}\mathrm{d}t'\,\left(\frac{k^2}{2}+A_z(t')k_z-\varepsilon_a\right)\right] \\
\times\sum_{\ell}\Bigg\{\frac{(-\mathrm{i})^{\ell}}{2}[\tilde{k}r_c j_\ell'(\tilde{k}r_c)+j_\ell(\tilde{k}r_c)]\psi^a_{\ell m_a}(r_c,t)Y_{\ell m_a}(\Omega_{\tilde{\mathbf{k}}}) \\
-\frac{(-\mathrm{i})^{\ell}}{2}r_c j_\ell(\Pi r_c)\psi^{a\prime}_{\ell m_a}(r_c,t)Y_{\ell m_a}(\Omega_{\tilde{\mathbf{k}}}) \\
-\mathrm{i}\sqrt{\frac{4\pi}{3}}r_c A_z(t)\psi^a_{\ell m_a}(r_c,t)\sum_{\ell'=\ell\pm1}(-\mathrm{i})^{\ell'}j_{\ell'}(\tilde{k}r_c)Y_{\ell' m_a}(\Omega_{\tilde{\mathbf{k}}}) \\
\times\sqrt{\frac{3}{4\pi}}(-1)^{m_a}\sqrt{(2\ell'+1)(2\ell+1)}\begin{pmatrix}\ell' & 1 & \ell\\ -m_a & 0 & m_a\end{pmatrix}\begin{pmatrix}\ell' & 1 & \ell\\ 0 & 0 & 0\end{pmatrix}\Bigg\}.
\end{aligned}
\tag{6.57}
$$

6.5 Infinite-Time Surface-Flux method

As mentioned above, the tSURFF method requires the time propagation to continue after the pulse has ended at T in order to let the response of the atom settle and the low-energy part of the scattering wavefunction exit the inner region and pass through the surface at r_c. We denote this time propagation, during $t > T$, as *postpropagation*. During the postpropagation, the dynamics is determined by a now time-independent Hamiltonian, $\hat{H}_{\mathrm{s}}(t>T) = \hat{H}_{\mathrm{s},0}$, which can be seen as procrastination for the electron since it evolves trivially without any external forces from the field. In the single-channel case, continuing this propagation from the time where the pulse ends to infinite time gives the surface integral

$$
b_a(\infty) - b_a(T) = \mathrm{i}\int_T^{\infty}\mathrm{d}t\; s_a(\mathbf{k},t) = \mathrm{i}\int_T^{\infty}\mathrm{d}t\;\langle\Psi_{\mathrm{s},a}|[\hat{H}_{\mathrm{s},0},\,\hat{\theta}(r_c)]|\Psi\rangle, \tag{6.58}
$$

for some scattering state associated with channel a, $|\Psi_{\mathrm{s},a}\rangle$.

Derivation of the iSURFF method

Since the field has vanished, the integral in Eq. (6.58) can be evaluated analytically by expanding the wavefunction over the eigenfunctions of the time-independent Hamiltonian.

[9] We show this full expression to point out a slight difference to the expression reported in Paper I, where the minus sign before the last term was erroneously typed as a plus sign and the $(-1)^{m_a}$ on the last line was written as $(-\mathrm{i})^{m_a}$.

This is the idea of the infinite-time surface-flux (iSURFF) method [46, 60]. The time evolution of the wavefunction is therefore given by

$$|\Psi(t > T)\rangle = \sum_{\gamma} |\gamma\rangle\langle\gamma|\Psi(T)\rangle \mathrm{e}^{-\mathrm{i}(E_\gamma - \varepsilon_k)(t-T)}, \tag{6.59}$$

where γ collects all necessary quantum numbers needed to represent an eigenfunction of the Hamiltonian. We reference the eigenenergies from the target photoelectron kinetic energy ε_k. By inserting the time evolution in Eq. (6.59) into the iSURFF surface amplitudes in Eq. (6.58), we obtain

$$s_a(\mathbf{k}, t) = \sum_{\gamma} g_{\gamma,a} \mathrm{e}^{-\mathrm{i}(E_\gamma - \varepsilon_k)(t-T)}, \tag{6.60}$$

where we have compactly expressed the two matrix elements,

$$g_{\gamma,a} = \langle \Psi_{\mathrm{s},a} | [\hat{H}_{\mathrm{s},0},\ \hat{\theta}(r_c)] | \gamma \rangle \langle \gamma | \Psi(T) \rangle. \tag{6.61}$$

We can then write the spectral amplitudes as

$$b_a(\infty) - b_a(T) = \sum_{\gamma} \frac{g_{\gamma,a}}{(\varepsilon_k - E_\gamma) + \frac{i}{2}\Gamma_\gamma}, \tag{6.62}$$

which is equivalent to

$$b_a(\infty) - b_a(T) = \langle \Psi_{\mathrm{s},a} | [\hat{H}_{\mathrm{s},0}, \hat{\theta}(r_c)] | (\hat{H}_0 - \varepsilon_k)^{-1} | \Psi(T) \rangle. \tag{6.63}$$

This amounts to solving the linear system

$$|Z\rangle = (\hat{H}_0 - \varepsilon_k)^{-1} |\Psi(T)\rangle, \tag{6.64}$$

for each target photoelectron kinetic energy. Inversion of $\hat{H}_0 - \varepsilon_k$ is impractical for any atomic system but hydrogen or systems treated within the single-active electron approximation, where $\hat{H}_0$ is diagonal. The matrix representation of $\hat{H}_0$ is however sparse and the diagonal, which roughly contains the electron–hole pair energy, is in most cases dominant. This makes possible the use of a linear solver such as the generalized minimal residual (GMRES) method [61].

Combining tSURFF and iSURFF

The asymptotic spectral amplitudes can now be retrieved by summing the contributions from tSURFF and iSURFF,

$$b_a(\mathbf{k}, \infty) = b_a(\mathbf{k}, T) + \mathrm{i} \int_T^\infty \mathrm{d}t\ s_a(\mathbf{k}, t), \tag{6.65}$$

where the first term is retrieved from tSURFF and the second from iSURFF. We denote the combination of tSURFF and iSURFF as t+iSURFF. In Fig. 9 we show a multiphoton ionization experiment along the polarization axis in hydrogen using tSURFF, iSURFF and the combination of the two. The one-, two-, and three-photon peaks are shown magnified in Fig. 9a, Fig. 9b, and Fig. 9c, respectively. The three spectra resolved on the full kinetic energy axis are shown in Fig. 9d. With tSURFF only, shown as a black dashed line, the one- and two-photon peaks are distinctly visible and there is a subtle sign of the three-photon peak. The four-photon peak is however masked by the high spectrum floor that prohibits any sign of higher-order peaks to appear. With iSURFF only, shown as a dotted gray line, there is a small increase in photoionization yield, seen as a background for the one-photon peak. Inspection of the spectrum from iSURFF only does not provide much information on the photoionization process in this case since most of the photoelectron has been recorded by tSURFF. However, when adding the tSURFF spectrum and the iSURFF spectrum coherently as in Eq. (6.65), the higher-order peaks emerge clearly. Note further the broadening of the photoelectron peaks for each absorbed photon, which results from the convolution involved in each interaction.

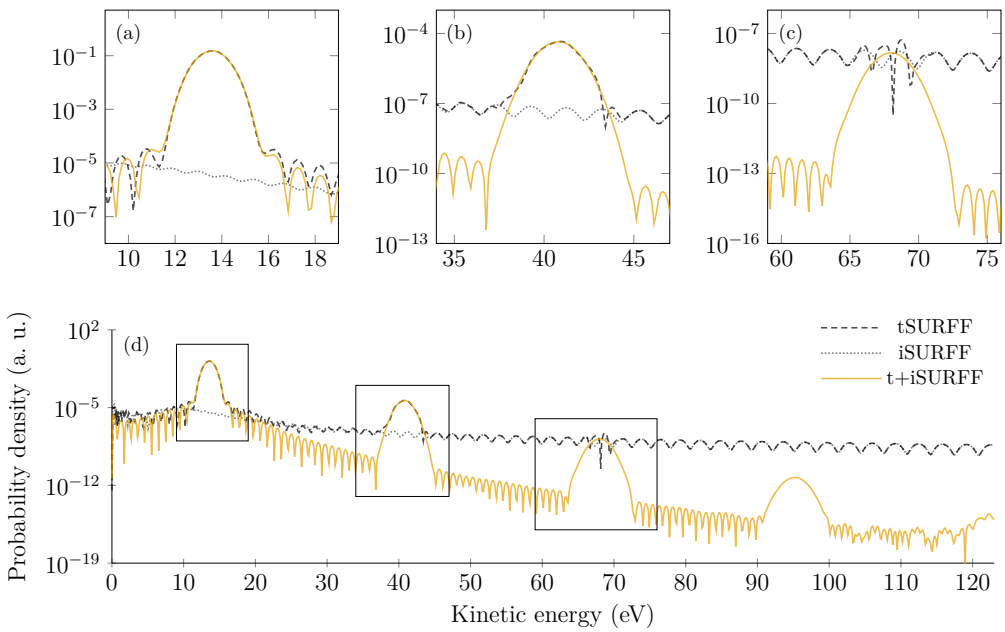

Figure 9: Photoelectron spectra of multiphoton ionization in hydrogen along the polarization axis using tSURFF, iSURFF, and t+iSURFF. For a spectrum captured directly after the pulse has finished, some of the photoelectron density has not yet reached the surface when the tSURFF amplitudes are evaluated, and is instead captured using iSURFF. The spectra are zoomed in on the one-photon peak in (a), the two-photon peak in (b), the three-photon peak in (c), and shown on the full kinetic energy axis in (d).

The scattering states we have used in our implementation of iSURFF are the adjusted Volkov states from Eq. (6.17). In principle, one can employ other scattering states, like

for instance the asymptotic Coulomb scattering states to the hydrogen atom, as described in Ref. [46]. Since no analytical solution exists to the Coulomb problem with a field, the full wave function needs to be kept inside the tSURFF radius r_c when the pulse is active, and compute the spectrum with only iSURFF. The iSURFF method with the Coulomb scattering states to the hydrogen atom is still an approximation when used to calculate photoelectron spectra to N-electron targets, which scattering states are Coulomb-like states[10]. The iSURFF method with the Coulomb scattering states resembles the procedure presented in Ref. [53], where (i) the final states are found numerically by solving the TDSE while the pulse is active, and (ii) the wave function is projected onto field-free asymptotic scattering states. In the case of double ionization, it is assumed that the asymptotic state is a product of one-electron asymptotic states. In step (ii) the outgoing wave function is expanded onto the field-free eigenstates and solved within the formalism of ECS to enforce the proper outgoing boundary conditions.

6.6 Partial-wave analysis

The spectral amplitudes $b_a(\mathbf{k}, t)$ are naturally retrieved as a function of momentum in spherical coordinates, with magnitude k, polar emission angle θ, and azimuthal emission angle φ. The combined laser–atom system displays cylindrical symmetry about the polarization axis z, why we may choose to evaluate the spectra in any angle φ. We may however change the angular part of the basis by projecting the wavefunction described by the coefficients $b_a(\mathbf{k}, t)$ onto a basis of electron partial waves,

$$b_{a,\ell,m}(k) = \int \mathrm{d}\Omega \; Y^*_{\ell,m}(\Omega) b_a(k, \Omega). \tag{6.66}$$

From a computational point of view, the number of nodes n_θ on the polar grid on which we evaluate the spectral amplitudes may then be limited to a minimum. If we restrict the computation to partial waves of some maximum orbital angular momentum $\ell_{\max}$, we can choose to evaluate the spectral amplitudes on a grid required by the quadrature of choice. When the partial-wave spectral amplitudes have been retrieved, we may retrieve the spectral amplitudes in any angle by interpolation.

In Fig. 10 and Fig. 11 we show photoelectron spectra from above-threshold ionization experiments in hydrogen and in neon with $2s$ and $2p$ channels open obtained with TDCIS-TRK, respectively. The electric fields are derived from vector potentials with truncated Gaussian envelopes[11] of full width at half maximum of 59.9174 fs,

$$A(t) = A_0 \sin(\Omega t) f(t, \tau), \tag{6.67}$$

[10]The Coulomb wave functions however form a complete basis, why the correct solution can in principle be given by a linear combination.

[11]The truncated Gaussian temporal envelope follows a Gaussian distribution in an inner region, but are truncated smoothly at the flanks as in Ref. [62] or the Appendix of paper VI.

following Eq. (3.23). The photon energy is chosen such that the one-photon peak from hydrogen and the $2p$ orbital in neon are located at $E_k = 0.5\,\text{a.u}$, $\hbar\Omega - I_p = 0.5\,\text{a.u.}$ The ionization potential of hydrogen is $I_p = 0.5\,\text{a.u.}$, of the $2p$ orbital in neon is $I_p = -\varepsilon_{2p}^{(\text{HF})} = 0.8504\,\text{a.u.}$, and of the $2s$ orbital in neon is $I_p = -\varepsilon_{2s}^{(\text{HF})} = 1.9304\,\text{a.u.}$ The intensity of the field is $1\,\text{TW}/\text{cm}^2$. The spectra are resolved on partial waves s in Fig. 10a, p in Fig. 10b, d in Fig. 10c, and f in Fig. 10d, and likewise in Fig. 11, and are compared to the total angle-integrated spectrum. The left column hence represents partial waves with even parity, and the right column represents partial waves with an odd parity. The alternating parity of the photoelectron for each exchange of photon is seen. In Fig. 10, the first peak corresponds to one-photon ionization of $1s$ and is hence mainly of p-character. The following peaks alternate between odd and even parities in accordance with the dipole selection rules. In the fourth peak, we expect some mixture of a g-wave, which we however do not project on. We also comment on the small peak between the one- and two-photon peaks in the s and d channels, located at 23.8 eV in Fig. 10a,c. This peak is due to sequential ionization from an intermediate Rydberg state, $2p_0$, which is reached by the spectral wings of the pulse [62], and is suppressed if a longer pulse in used.

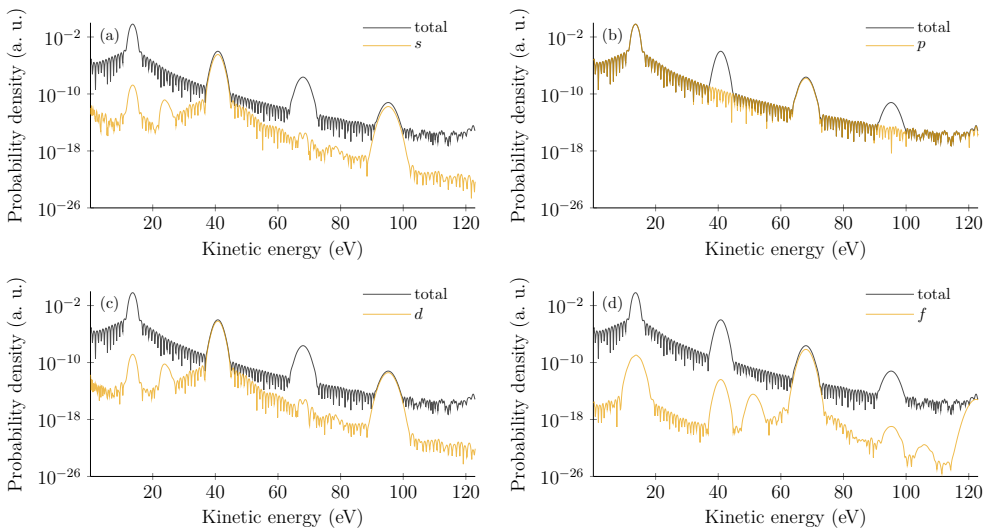

Figure 10: Above-threshold ionization spectra from a t-iSURFF calculation in hydrogen compared to the projections on partial waves (a) s, (b) p, (c) d, and (d) f. The parity alternates between odd and even for each absorbed photon.

In Fig. 11 the double-peak structure stems from ionization from one-photon ionization from $2p$ and two-photon ionization from $2s$. The ionization potential of $2s$ is given by $I_p^{2s} = 1.9304\,\text{a.u.}$ and the two-photon peak from $2s$ therefore almost overlaps with the one-photon peak from $2p$. The two peaks have the same parity because of the surplus of one photon exchange for the electrons stemming from $2s$. The propensity rule for continuum–

continuum transitions, discussed in Sec. 7.1, is further seen, i.e. in the second peak were the d wave is stronger than the s wave in Fig. 10 in hydrogen, and the f wave is stronger than the p wave in Fig. 11 in neon.

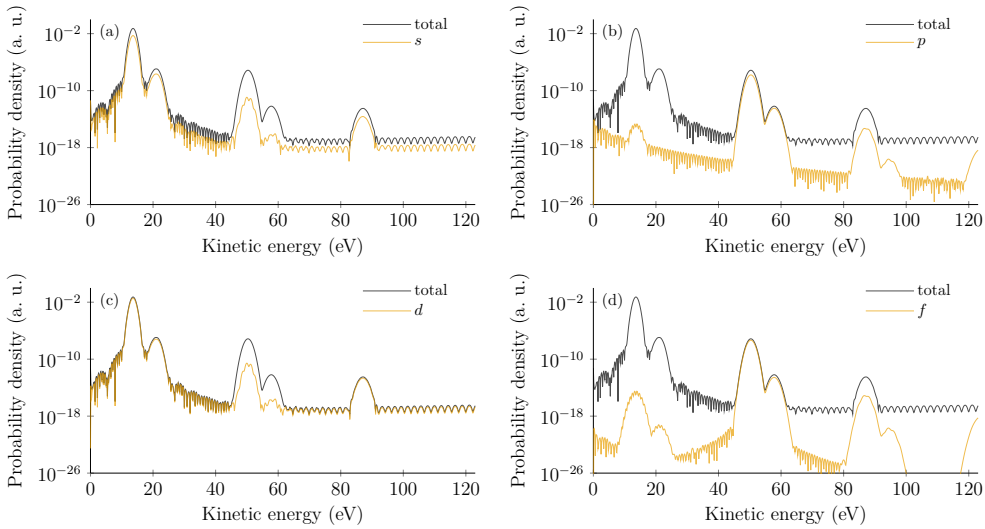

Figure 11: Above-threshold ionization spectra from a t+iSURFF calculation in neon, with $2s$ and $2p$ open, based on a TDCIS-TRK calculation, compared to the projections on partial waves (a) s, (b) p, (c) d, and (d) f. The parity alternates between odd and even for each absorbed photon. The double-peak structure comes from ionization from $2s$ and $2p$. Compared to the $2p$ state, it requires the absorption of one more photon to ionize from the $2s$ state, which is why the double peak has consistent parity.

6.7 Consistency tests of tSURFF and iSURFF

In order to make sure that tSURFF and iSURFF are correctly implemented, a number of tests can be performed. In this section, we present some of the key tests that we have done in order to test the consistency of the implementation of tSURFF and iSURFF.

Faded Coulomb potential

We occasionally turn off the Coulomb tail smoothly during the consistency tests to ensure that the tSURFF assumption of short-range potentials holds. This of course changes the physical problem, and in particular we must put care into not distorting the energy levels of interest, but it means that the Volkov states can be used as the *correct* final states. The Coulomb potential is turned off similar to how it is done in Morales et al. [46]. The two-

electron Slater integrals, cf. Eq. (3.44b) in Ref. [26], then becomes

$$R^k(ab,cd) = \int\int \mathrm{d}r_1 \mathrm{d}r_2 \; P_a(r_1) P_b(r_2) f_{\mathrm{supp}}(r_1) f_{\mathrm{supp}}(r_2) \frac{r_<^k}{r_>^{k+1}} P_c(r_1) P_d(r_2), \tag{6.68a}$$

$$f_{\mathrm{supp}} = \begin{cases} 1, & r \leq R_{\mathrm{off}}, \\ \frac{1}{2} - \frac{1}{2} f_{\mathrm{B}}\left(f_{\mathrm{B}}\left(f_{\mathrm{B}}\left(2\frac{r-R_{\mathrm{off}}}{r-R_0} - 1\right)\right)\right), & R_{\mathrm{off}} \leq r \leq R_0, \\ 0, & r > R_0, \end{cases} \tag{6.68b}$$

where the suppression function is formed by the Becke switching function [63], $f_{\mathrm{B}} = 3x/2 - x^3/2$. In Fig. 12a, the lowest excited-state energies of neon with $\ell_{\max} = 3$, found by diagonalizing the CIS Hamiltonian, are shown and compared to the case where the Coulomb potential is truncated smoothly. In the inset we show the suppression function f_{supp} from Eq. (6.68b) over the radial distance. With a smoothly faded potential, the lowest excited-state energies are intact while the higher-lying Rydberg states become less bound and rise in energy. In the present case, $R_0 = 95\,\mathrm{Bohr}$ and $R_{\mathrm{off}} = 115\,\mathrm{Bohr}$, the twenty first excited-state energies agree to graphical precision. We must therefore make sure that the Rydberg states of interest are not altered too much by using a computational box *large enough*. For a spectrally narrow high-energy XUV pulse, which does not populate any excited state, this is easily done, while it must be considered for a pulse which does populate Rydberg states. In Fig. 12b, we show a photoelectron spectrum from ionization of outer-shell neon with two XUV fields with photon energies $\hbar\Omega_1 = 22.96\,\mathrm{eV}$ and $\hbar\Omega_2 = 26.0214\,\mathrm{eV}$, close to the ionization potential, $I_p = 21.5786\,\mathrm{eV}$. The intensities of the fields are set to $I_\Omega = 1\,\mathrm{TW/cm^2}$. The photoelectron spectra are recorded at $r_c = 120\,\mathrm{Bohr}$ with t-iSURFF for a faded Coulomb potential and compared to the corresponding spectra without fading of the Coulomb potential. Despite the agreement between the two bases, there is a difference between the two spectra, which is most notable at low kinetic energies, where rapid oscillations are seen in the first photoionization peak. The oscillations on the peak are due to the Volkov states' inability to act as scattering states to the TDSE with a Coulomb potential. With the faded Coulomb potential these oscillations are reduced.

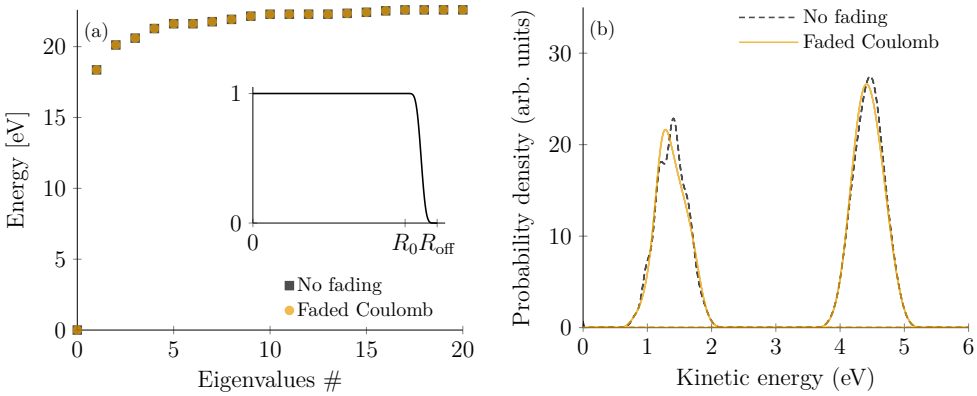

Figure 12: (a) Comparison of the energies of the first excited bound states in neon with $\ell_{\max} = 3$, found by diagonalizing the CIS Hamiltonian, compared to the corresponding energies retrieved when fading the Coulomb potential using Eq. (6.68a). (b) Comparison of photoelectron spectra retrieved with t-iSURFF when using the CIS Hamiltonian and the CIS Hamiltonian with a faded Coulomb potential.

At very low kinetic energies, we still expect a breakdown of the spectrum when using the faded Coulomb potential. According to the Levinson theorem, see Ref. [64, 65], there is a phase shift of $\delta(0) = \mu(\infty)\pi$ when approaching the ionization threshold for the short-ranged faded Coulomb potential, where $\mu(\infty)$ is the quantum defect. In addition to the phase shift predicted by the Levinson theorem, there is a diverging phase shift due to the Coulomb potential, c.f. Ref. [64, 65], which cannot be accounted for by the Volkov states at threshold. It is therefore expected that the Volkov scattering states fail to reproduce this.

Postpropagation time

The combination of tSURFF and iSURFF to evaluate the asymptotic spectral amplitudes $b_a(\mathbf{k}, \infty)$ in Eq. (6.65) should yield the same result regardless of the choice of final tSURFF time T, provided that the pulse has finished. A good test for consistency is thus to compare two spectra obtained with different choices of T. This simply moves the postpropagation time from the tSURFF integral to the iSURFF integral and should give identical results.

In Fig. 13, we show two multiphoton-ionization spectra from a weak XUV pulse of photon energy $\hbar\omega - I_p = 0.5$ a.u. The spectra in black are obtained with the tSURFF stop time $T = t_{\text{off}}$ chosen directly when the pulse is turned off, and the spectra in orange are obtained with a postpropagation time of $T = t_{\text{off}} + 200$ a.u. Fig. 13a shows the comparison in hydrogen and Fig. 13b shows the comparison in helium. The pulse envelope is chosen to a truncated Gaussian with a full width at half maximum (FWHM) of $\tau = 59.9174$ a.u. ($\tau = 1.45$ fs), which is smoothly truncated to zero between four and six standard deviations of the Gaussian distribution such that the pulse is zero at $t_{\text{off}} = 152.6673$ a.u. The two

spectra are identical up to numerical accuracy in the converged region, which confirms that the implementation has been correctly performed for the single-electron case.

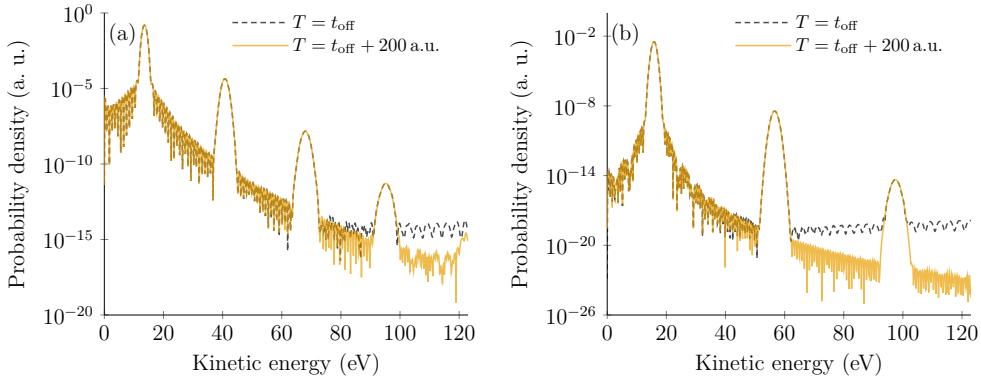

Figure 13: Consistency test for the combination of tSURFF and iSURFF, in (a) hydrogen, and in (b) helium, by comparing the case when the tSURFF stop time is chosen at the time when the pulse is turned off, $T = t_{\text{off}}$, to the case when the tSURFF stop time is chosen after 200 a.u. of postpropagation, $T = t_{\text{off}} + 200$ a.u. The two spectra are identical to numerical accuracy where the convergence is met.

In a similar fashion, we show in Fig. 14 photoelectron spectra in neon recorded with t+iSURFF to compare the two cases of postpropagation time, $T = t_{\text{off}}$, and no postpropagtion time $T = t_{\text{off}} + 200$ a.u. In Fig. 14a neon with only $2p$ active, and Fig. 14b neon with $2s$ and $2p$ active. In the converged regions, the spectra agree. In Fig. 14b, the n-photon peaks from $2p$ almost overlap with the $n+1$-photon peaks from $2s$, similar to Fig. 11, which is why there are double peaks in the spectrum.

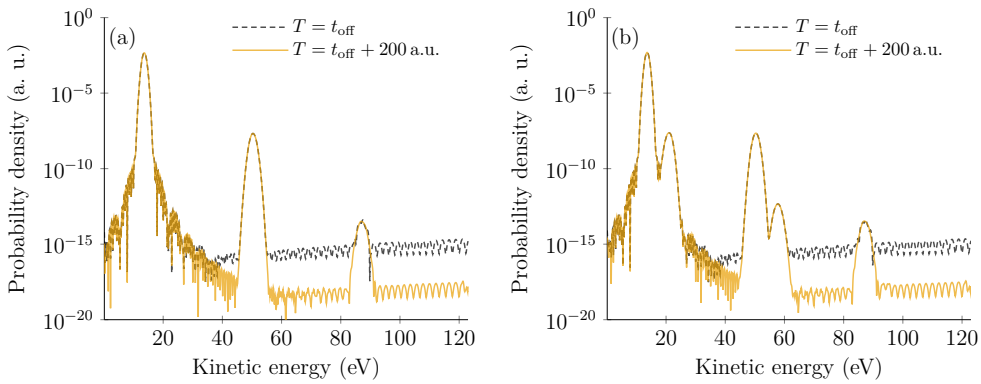

Figure 14: Consistency test for the combination of tSURFF and iSURFF by comparing the case when the tSURFF stop time is chosen at the time when the pulse is turned off, $T = t_{\text{off}}$, to the case when the tSURFF stop time is chosen after 200 a.u. of postpropagation, $T = t_{\text{off}} + 200$ a.u. In (a) the spectra are retrieved in neon with $2p$ active and (b) the spectra are retrieved in neon with $2s$ and $2p$ active. In both (a) and (b), the two spectra are identical to numerical accuracy where the convergence is met.

Absorbing boundary conditions

To avoid reflections of the outgoing wave packet from the end of the numerical radial grid, some artificial boundary conditions must be implemented that pads the inner computational region from reflections. We make use of exterior complex scaling [55, 66, 67], which analytically continues the radial coordinates to the complex plane outside some radius R_0 by rotating it as

$$r \to \begin{cases} r, & r \leq R_0, \\ R_0 + (r - R_0)\mathrm{e}^{i\theta}, & r > R_0. \end{cases} \tag{6.69}$$

One could view the exterior complex scaling as a transformation of out- and ingoing plane waves at the end of the grid [57]. The transformed plane waves then have the form

$$\mathrm{e}^{+\mathrm{i}kr} \to \mathrm{e}^{+\mathrm{i}kR_0}\mathrm{e}^{+\mathrm{i}k\cos\theta(r-R_0)}\mathrm{e}^{-k\sin\theta(r-R_0)}, \tag{6.70a}$$

$$\mathrm{e}^{-\mathrm{i}kr} \to \mathrm{e}^{-\mathrm{i}kR_0}\mathrm{e}^{-\mathrm{i}k\cos\theta(r-R_0)}\mathrm{e}^{+k\sin\theta(r-R_0)}, \tag{6.70b}$$

where the outgoing waves in expression (6.70a) become exponentially damped and the ingoing waves in expression (6.70b) grows exponentially. We thus have the possibility to separate the out- and ingoing waves on their normalizability [57].

Another perspective on ECS is that the Hamiltonian is unitarily transformed by

$$\hat{H}(t) \to U_\theta \hat{H}(t) U_\theta^{-1}, \tag{6.71}$$

as also discussed in Ref. [57]. Because the continuation is analytic, the new solutions Ψ_θ are the same as the original solutions Ψ inside the domain $[0,\ R_0]$ – the *inner* region – but the hermiticity of $\hat{H}$ is lost and the left and right eigenvectors are thus not complex conjugates. The matrix elements in our implementation are computed with the left vectors being the transpose of the right eigenvectors.

In order to assure that no spurious reflections appear in the photoelectron spectrum, the extent of the dampening region r_{ecs} and the scaling angle θ must be chosen. The spectra are however not very sensitive to these parameters, as can be see in Fig. 15, where we short the first- and second-order peaks from multiphoton ionization in hydrogen. In Fig. 15a, we use a inner box size of $r_0 = 80.4657\,\mathrm{Bohr}$ and a dampening region of $r_{\mathrm{ecs}} - r_0 = 8.04657\,\mathrm{Bohr}$ and vary the scaling angle θ. The four spectra are retrieved for different values of the scaling angles θ and are vertically displaced for easier comparison. For small angles (black), spurious reflections of the outgoing wave packet severely distort the photoelectron spectrum. These reflections can also be seen in the slightly larger angle $\theta = 5\,\mathrm{deg}$ (orange). For the larger angles, $\theta = 10\,\mathrm{deg}$ and $\theta = 20\,\mathrm{deg}$, the reflections are dampened sufficiently. In Fig. 15b we show the same photoionization experiment

retrieved with $\theta = 20\,\mathrm{deg}$, but varying the dampening region, r_{ecs}. For a small dampening region, in the calculation $r_{\mathrm{ecs}} = 0.8\,\mathrm{a.u.}$ (black), reflections are clearly distorting the photoelectron spectrum. For larger values of r_{ecs} the spectra converge quickly, effectively dampening the reflections.

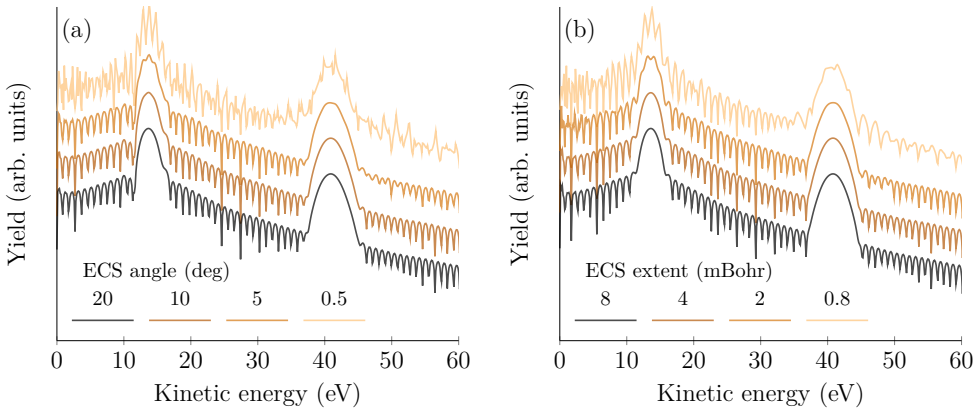

Figure 15: One- and two-photon peaks in multiphoton ionization in hydrogen using (a) different scaling angles θ, and (b) different extents of the ECS region.

Time integration of tSURFF

We solve the coupled set of equations for the spectral amplitudes $b_a(\mathbf{k}, t)$ in Eq. (6.46) by means of the second-order accurate trapezoidal method[12], as also done in Ref. [60]. We integrate in time for each value of the momentum and emission angle separately and omit $\mathbf{k}$ in the notation to not clutter the notation. On matrix form, the trapezoidal method applied to Eq. (6.46) gives

$$-\mathrm{i}\frac{\mathbf{b}_{n+1} - \mathbf{b}_n}{\Delta t} = \frac{1}{2}\left[\mathbf{s}(t_{n+1}) + \mathbf{s}(t_n)\right] - \frac{1}{2}\left[\mathbf{b}_{n+1}\hat{H}_{\mathrm{cc}}(t_{n+1}) + \mathbf{b}_n\hat{H}_{\mathrm{cc}}(t_n)\right], \quad (6.72)$$

where $\hat{H}_{\mathrm{cc}}$ is the *channel-coupling* matrix [50, 58], which is the second term of Eq. (6.46), and $\Delta t = t_{n+1} - t_n$. Eq. (6.72) can be rearranged as

$$\left[\hat{\mathbb{I}} + \frac{\mathrm{i}\Delta t}{2}\hat{H}_{\mathrm{cc}}(t_{n+1})\right]\mathbf{b}_{n+1} = \left[\hat{\mathbb{I}} - \frac{\mathrm{i}\Delta t}{2}\hat{H}_{\mathrm{cc}}(t_n)\right]\mathbf{b}_n + \frac{\mathrm{i}\Delta t}{2}\left[\mathbf{s}(t_{n+1}) + \mathbf{s}(t_n)\right], \quad (6.73)$$

[12] In principle, one could solve this system to higher order. The accuracy would however be capped by the accuracy used in retrieving the expansion coefficients of the wavefunction. In our case, we use a second-order scheme for propagating the TDCIS equations of motion in Eq. (5.16), see Ref. [41, 68], and therefore benefit little from using a more accurate method than the trapezoidal method.

where $\hat{\mathbb{I}}$ is the identity operator of size $n_a \times n_a$, where n_a is the number of active core orbitals; $n_a = 3$ for neon and $n_a = 2$ for neon with only the $2s$ and the $2p$ orbitals active, for instance.

To test that the time integration in tSURFF is consistently implemented with respect to the time propagation of the TDCIS amplitudes from Eq. (5.16), we compare in Fig. 16 the error of the spectra from Fig. 13–14 when increasing the time step, Δt. In Fig. 16a, the error of convergence for spectra retrieved with t+iSURFF are estimated by

$$e^{(n)} = \int \mathrm{d}E_k \, ||S^{(n)}(E_k) - S^{(0)}(E_k)||_1, \tag{6.74}$$

where $S^{(n)}(E_k)$ denotes the photoelectron spectrum measured at a photoelectron kinetic energy E_k with a time step $\Delta t = 0.001 \times 2^n$ a.u., and $||\cdot||_1$ denotes the 1-norm. The error is compared to Δt^n (black lines of Fig. 16a) and it is seen that the error descreases as Δt^2. This makes sure that the phase is defined equally in tSURFF and the TDCIS time discretization. We show the obtained spectra in Fig. 16b, retrieved with the time steps marked in Fig. 16a. For the large time steps, the spectra saturates earlier at lower kinetic energies of the photoelectron.

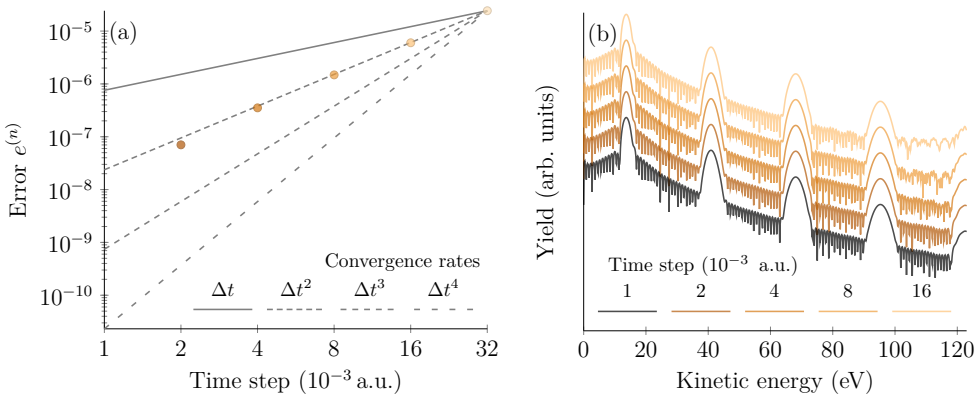

Figure 16: (a) Estimated convergence rate in time step for the implementation of tSURFF. (b) Comparison between the spectra retrieved with the time steps in (a). The atomic unit of time corresponds to one femtosecond as $1\,\mathrm{fs} = 1000/24.2\,\mathrm{a.u.}$

Applications in attosecond physics and free-electron laser science

7 Laser-Assisted Photoionization

The major part of the applications in this thesis addresses laser-assisted photoionization (LAP). Laser-assisted photoionization describes an atom that is ionization by absorption of a photon from a short-wavelength field, while an additional long-wavelength field *dresses* the atom. Typically, the short-wavelength field is an XUV field generated from HHG [19, 20] or generated in a FEL facility such as FERMI [13]. Laser-assisted photoionization is then described by the reaction

$$A + \gamma_{\mathrm{XUV}} \pm q\gamma_{\mathrm{IR}} = A^{+} + e^{-}, \tag{7.1}$$

where an atom A absorbs an XUV photon, γ_{XUV}, and exchanges q IR photons, γ_{IR}, to form an ion A^{+} and a free electron e^{-}. The energy of the XUV photon, $\hbar\Omega$, and the energy of the net exchange of IR photons, $\pm q\hbar\omega$, together with the ionization potential of the atom and the ponderomotive energy of the IR field, determine the classical estimate for the kinetic energy of the ejected photoelectron,

$$E_k = \hbar\Omega - I_p - U_p \pm q\hbar\omega. \tag{7.2}$$

The interactions can happen in any order, but we will model the time order where interactions with the XUV field appear before the exchange of the IR photons. The reverse time order, where the IR photons are exchanged first are though important in e.g. photodetachment of negative ions [69]. All possible time orders are however included when we solve TDSE within TDCIS. The question of gauges and time orders have been recently reviewed by Vinbladh et al. by evaluation of two-photon matrix elements for ATI, which are relevant for calculations of attosecond time delays in photoionization [70].

LAP problems can further be subdivided into several different regimes, for instance if the assisting IR field is an intense or a weak field, or if the XUV field includes multiple carrier frequencies. We will in this section discuss the following three regimes of LAP, which have been studied in the work that comprises this thesis:

7.1 Single weak XUV field under dressing of a weak IR field.

The atom is ionized by the XUV field by absorption of one XUV photon with subsequent instantaneous exchange of IR photons that strongly decrease in probability with the order of IR photons involved. The weak dressing of the IR field makes possible the use of perturbation theory to explain the photoionization dynamics and the final photoelectron distribution. Here, we discuss the angular distributions in the photoelectron spectrum and discuss propensity rules for continuum–continuum transitions.

7.2 Single weak XUV field under dressing of a strong IR.

The atom is ionized by the XUV field by absorption of one XUV photon, but under influence of the strong IR field. The photoelectron density is redistributed in the continuum by exchange of IR photons, but the photoelectron peaks in the spectrum may show sign of dynamical interference for smoothly varying envelopes. We discuss laser-assisted dynamical interference and discuss why this effect appears in a two-color setup, but not when using a single-color field.

7.3 Multiple weak XUV fields under dressing of a weak IR field.

The multiple XUV fields ionize the atom, to create a comb of photoelectron peaks in the spectrum. These peaks are made to interfere in sideband peaks by a synchronized IR field. The multiple pathways to the sidebands contain phase information, which may be used to characterize the pulses or to provide information about the target system. We discuss these interference effects using a simple rule of thumb, capable of describing the general phase and amplitude effects in the limit of a small ponderomotive energy.

The fields in all of these regimes may be described by the vector potential, linearly polarized along the z-axis,

$$A(t) = \sum_i A_{\Omega_i,0} \sin(\Omega_i t - \delta_i) F_{\Omega_i}(t, \tau_{\Omega_i}) + A_{\omega,0} \sin(\omega t - \varphi) F_\omega(t, \tau_\omega), \qquad (7.3)$$

where a temporal envelope with length τ is denoted $F(t, \tau)$. The XUV fields are denoted by subscript Ω_i, and the dressing IR field is denoted by subscript ω. The vector potentials are defined as sine waves. This implies that the corresponding electric fields would be (negative) cosine waves for slowly varying envelopes. While this choice is arbitrary at this point, we have found in Paper II that it is important to obtain equations that allow for simple interpretations of multiphoton transitions in terms of interaction phases, which are discussed in Sec. 7.3.

The general applicability of LAP in attosecond and free electron lasers of course extends outside the scope of this thesis, which by the use of TDCIS includes single ionization in noble gas atoms. Among the experimental and theoretical applications of LAP outside the scope of this thesis we mention pump–probe schemes using XUV radiation from HHG and IR in e.g. molecules [71, 72], and using autoionizing states [73].

7.1 Angular distribution and propensity rules

The multiple angular-momentum channels in LAP have inspired attosecond experiments with angular resolution. While the importance of angular resolution has been known for

some time, see e.g. early work by Cooper and Zare [74, 75], it is only recently that angle-resolved attosecond experiments have been performed, see for instance Ref. [38, 76].

For an experiment with angular resolution, the signal in the angle-resolved photoelectron spectrum from a noble gas atom is given by

$$S(k,\theta) = \sum_m \left| \sum_\ell b_{a,\ell,m}(k,\theta) \right|^2 , \tag{7.4}$$

where the electron orbital angular momenta are summed coherently and the electron magnetic quantum number, as well as the ionic degrees of freedom, are summed incoherently. In a LAP experiment, the photoelectron angular distribution of the sidebands differs between sidebands created by absorption of photons in the continuum and sidebands created by emission of photons in the continuum. This was identified by Busto et al. [38] in extending the propensity rule for ionization [37] to continuum–continuum transitions. It was found that absorption of photons in the continuum is to a larger degree associated with an increase of angular momenta, while emission of photons in the continuum is to a larger degree associated with a decrease, analogous to what is known for bound–bound transitions [3]. The opposite behaviour of absorption and of emission is due to time-reversal symmetry. The propensity rule is further shown to stem from the radial part of the transition matrix element, and is therefore most prominent in the low-energy electrons [38].

As an example, consider an electron ejected from the $1s$ orbital in helium, which thus generates a p-wave, and which subsequently exchanges one IR photon. The electron will be in a superposition state between s and d partial waves, $b_{a,s,0} + b_{a,d,0}$. The propensity rule for continuum–continuum transitions then predicts that the sideband reached by absorption of one IR photon (the $q = +1$ sideband) has a larger proportion of d than s, and reversely that the sideband reached by emission of one IR photon (the $q = -1$ sideband) has a larger proportion of s. As a consequence, the $q = +1$ sideband shows two nodes while the $q = -1$ sideband shows one node. This of course requires long enough pulses so that the photoelectron peaks are separated in the spectrum. The additional nodes in the photoelectron angular distribution in the absorption path appear due to a π phase shift of the d-wave as it vanishes, and there has therefore been an interest in studying the correspondence between photoionization time delays and angular distributions [77–79].

When we studied angle-resolved LAP in Paper I, we confirmed the propensity rule for continuum transitions and that it was responsible for a disproportion between the dipole-allowed partial waves. We further saw that this disproportion accumulated in the low-energy limit to higher-order sidebands that include exchange of multiple IR photons. We show this disproportion in helium in Fig. 17, where we schematically show ionization pathways and plot angular distributions as the logarithm of the signal S from Eq. (7.4). The first sideband peaks $q = \pm 1$ are shown in Fig. 17a and the second sideband peaks $q = \pm 2$ are shown in Fig. 17b.

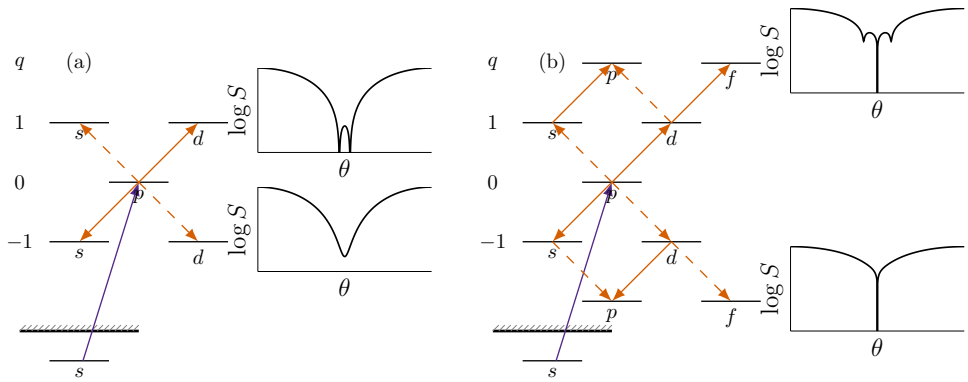

Figure 17: Ionization pathways in helium and angular distributions of the (a) $q = \pm 1$ peaks, and (b) $q = \pm 2$ peaks. The solid lines in the pathway diagrams represent the transitions that are favoured by the propensity rule. Angular distributions are plotted on a logarithmic scale.

However, when studying the photoelectron spectrum of electrons coming from outer-shell neon, we could not observe any qualitative difference between the $q = +1$ and $q = -1$ sidebands. This was because the multiple m channels, $m = 0$ and $m = \pm 1$, add incoherently, and since the $m = 0$ channel has two maxima approximately where the $m = \pm 1$ channels have two minima the difference between absorption and emission is effectively wiped out. The ionization pathways and the angular distributions for $q = \pm 1$ are shown in Fig. 18 for neon, with $m = 0$ and $m = \pm 1$, respectively.

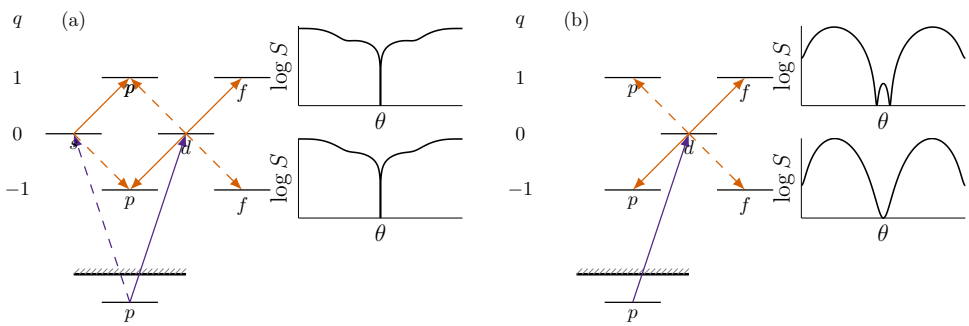

Figure 18: Ionization pathways in neon and angular distributions of the $q = \pm 1$ peaks, for (a) $m = 0$, and (b) $m = \pm 1$, respectively. The solid lines in the pathway diagrams represent the transitions that are favoured by the propensity rule. Angular distributions are plotted on a logarithmic scale.

To quantify the role of the propensity rule one may calculate the ratio of the absolute complex amplitudes of different partial waves, characterized by ℓ and m, at an electron kinetic energy corresponding to a peak reached by absorption (or emission) of q IR photons. In the high-energy limit, this ratio is determined by the ratio of the angular part of the dipole-transition matrix element. For the first sidebands of helium, for instance, this means

that the proportion of d and s (for both absorption and emission), approaches

$$\lim_{k\to\infty}\left|\frac{b^{\pm1}_{a,2,0}}{b^{\pm1}_{a,0,0}}\right| = \left|\frac{\langle Y_{20}|Y_{10}|Y_{10}\rangle}{\langle Y_{00}|Y_{10}|Y_{10}\rangle}\right| = \frac{2}{\sqrt{5}}. \tag{7.5}$$

A node in the angular distribution requires that the two partial waves in the superposition cancel and therefore that $b_{a,\ell_>,m} = -b_{a,\ell_<,m}$. We can thus write the node condition that

$$\frac{\tilde{b}_{a,\ell_>,m}}{\tilde{b}_{a,\ell_<,m}} = -\frac{Y_{\ell_<m}(\theta,\varphi)}{Y_{\ell_>m}(\theta,\varphi)} \tag{7.6}$$

needs to be fulfilled, where $\tilde{b}$ denotes the radial part of the spectral amplitude. We found that the asymptotic value calculated in Eq. (7.5) can be retrieved by evaluating the ratio between the partial waves at an angle where a node is located[13]. In helium, which shows a node at $\theta = \pi/2$, we calculate

$$\lim_{\theta\to\pi/2} -\frac{Y_{00}(\theta,\varphi)}{Y_{20}(\theta,\varphi)} = \frac{2}{\sqrt{5}}. \tag{7.7}$$

Since the node condition holds only in the limit, a small change in the ratio of partial waves may lead to drastically different angular distributions, which explains why absorption and emission sidebands display different distributions.

Moreover, if there are multiple intermediate angular momenta, like in $q = \pm2$ in both helium and neon, these paths will interfere and compete with the propensity rule. At high kinetic energies, the angular part overtakes and the interference between the different pathways dominates. For neon with $m = \pm1$, we have

$$\lim_{k\to\infty}\left|\frac{b^{\pm2}_{a,4,1}}{b^{\pm2}_{a,2,1}}\right| = \left|\frac{\langle Y_{41}|Y_{10}|Y_{31}\rangle\langle Y_{31}|Y_{10}|Y_{21}\rangle}{|\langle Y_{21}|Y_{10}|Y_{31}\rangle|^2 + |\langle Y_{21}|Y_{10}|Y_{11}\rangle|^2}\right| = \frac{\sqrt{8}}{3\sqrt{3}}. \tag{7.8}$$

In Fig. 19 the ionization pathways and angular distributions for the $q = \pm2$ pathways are shown for neon with $m = \pm1$. The two paths add constructively, since the continuum–continuum phase only depends weakly on the intermediate angular momentum, cf. Ref. [80], and will therefore favour a decrease in angular momentum. The angular distribution along the two sidebands differ qualitatively with $q = +2$ showing more nodes than the $q = -2$ sideband. This is an example of the delicacy of the node condition.

[13] We found it quite remarkable that the ratio of the integrals of dipole coupling in Eq. (7.5) could be obtained by evaluating just the final spherical harmonics at the position of the node.

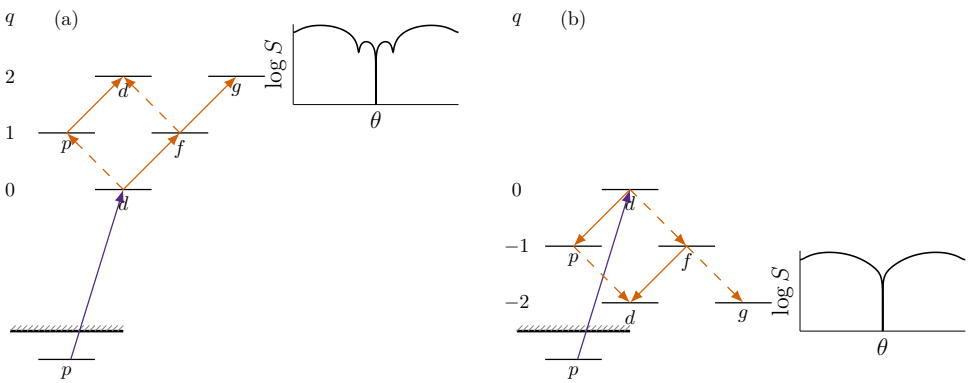

Figure 19: Ionization pathways in LAP in outer-shell neon with $m = \pm 1$. The solid lines in the pathway diagrams represent the transitions that are favoured by the propensity rule. The two pathways that lead to a d partial wave add constructively for both $q = +2$ and $q = -2$.

7.2 Dynamical interference

An atom subjected to intense radiation will have its resonances shifted as shown in Sec. 4.2. Multiphoton couplings between bound states under strong-field conditions can both enhance or inhibit photoionization and lead to rich interference structures in the photoelectron spectrum [81]. This led to the idea of a Ramsey-like[14] resonant-photoionization experiment where two temporally separated pulses are used to probe the atomic system at different times [83–85]. In between the two pulses, in the *dark* period, the two or more populated states develop different phases depending on their energies. This temporal double slit is mediated by atomic resonances and requires intense fields with low frequencies.

It was however known that strong-field conditions severely affects photoionization spectra also in non-resonant photoionization by e.g. shifting the ionization threshold by approximately U_p [16], which lowers the kinetic energy of the ejected electrons [36]. For a non-resonant field, the ac Stark shift, and therefore also the instantaneous U_p, follow the pulse envelope. Similarly to the above-mentioned experiments including bound states, the shift of the ionization potential follows the pulse envelope. This spurred the interest of a *dynamical interference* effect where photoelectrons at a certain kinetic energy would be created at two instances in time and thus showing sign of interference in the spectrum [86]. The interest was also driven by the new generation of light sources such as FEL at hand[15].

The formal criteria that need to be satisfied in order to record dynamical interference were

[14] See for instance Ref. [82] on Ramsey interference.

[15] Observation of dynamical interference using FEL radiation was the initial incentive to Paper IV. It turned out that dynamical interference did not play a role, but instead an in situ measurement of Rabi oscillations was done, which we discuss further in Sec. 10.

formulated in Ref. [87]; (i) the ac Stark shift should be larger than the spectral width of the pulse, and (ii) the ionization rate should be low enough to not deplete the initial state. These two criteria have been difficult to meet simultaneously with a single field. On the one hand, the field needs to be intense enough for (i) to hold, but a too intense field quickly depletes the atom, thus inhibiting (ii) to be fulfilled. At very large intensity however, the ionization rate decreases with intensity in what is known as *atomic stabilization* [88], contrary to lowest-order perturbation theory, which would predict that the one-photon ionization rate increases linearly with intensity, as shown by Eq. (1.2). Therefore, it was predicted that dynamical interference could only be seen at the onset of atomic stabilization [89–92].

In Paper VI we identified interference fringes in LAP using an XUV+IR setup as dynamical interference, at intensities far below the atomic stabilization regime, and found that the criteria (i) and (ii) could be simultaneously met in an XUV+IR setup The criteria are then separated so that the IR controls the ac Stark shift [criterion (i)] and the XUV controls the ionization rate [criterion (ii)]. We predict that this makes it possible to observe the dynamical interference effect, shown in Fig. 20, under experimentally feasible conditions.

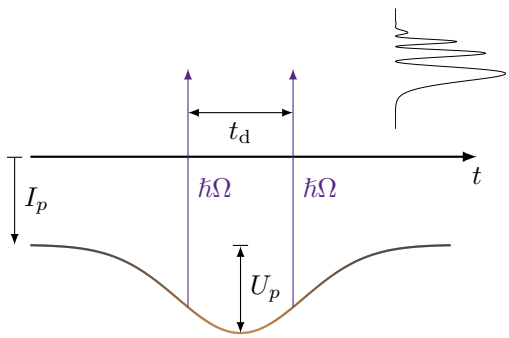

Figure 20: Sketch of photoionization using an XUV field under dressing of a strong IR field of Gaussian envelope. The IR field shifts the atomic levels relative to the ionization threshold such that the photoelectron can interfere with itself at different times. The instantaneous IR intensity is illustrated with the gradient of the bound state, ranging from low (black) to high (orange), and the ponderomotive shift is illustrated in the bound state. The time delay between the two ionization events, t_d, is given in Eq. (7.16).

To understand this effect, we extend the model of Jiang and Burgdörfer [92] to an XUV+IR setup. The complex amplitude for a transition to a continuum state with energy $\varepsilon = k^2/2$ is modeled by

$$c(\varepsilon) = -\mathrm{i}p_{\varepsilon,a}A_0 \int_{-\infty}^{\infty} \mathrm{d}t'\; g_\Omega(t',\tau_\Omega)\mathrm{e}^{\mathrm{i}(\varepsilon-\Omega-\varepsilon_a)t'}\mathrm{e}^{\frac{\Gamma(\Omega)}{2}G_\Omega(t',\tau_\Omega)}\mathrm{e}^{\mathrm{i}\Delta(\omega)G_\omega(t',\tau_\omega)}, \quad (7.9)$$

where Γ is the ionization rate and Δ is the ac Stark shift. The XUV intensity envelope is denoted g_Ω, and the integrated intensity envelope for the XUV and IR pulses are denoted

G_Ω and G_ω, respectively. For Gaussian pulses, the integrated envelopes are given by

$$G(t',\tau) = \int_{-\infty}^{t'} \mathrm{d}t''\, g^2(t'',\tau) = \int_{-\infty}^{t'} \mathrm{d}t''\, \exp\left[-4\ln 4 \left(\frac{t''}{\tau}\right)^2\right]. \tag{7.10}$$

In writing Eq. (7.9) we have assumed that only the XUV contributes to the ionization, $\Gamma \approx \Gamma(\Omega)$, due to absorption of an XUV photon, and the IR determines the energy shifts of the bound states, $\Delta \approx \Delta(\omega)$, due to both absorption and emission of IR photons.

In agreement with the result in the atomic stabilization regime, Jiang and Burgdörfer showed with the use of the stationary-phase approximation (SPA) that the contribution to the complex amplitude in Eq. (7.9) comes largely from two instances in time, t_i, $i = 1, 2$, separated by a time $t_\mathrm{d} = t_2 - t_1$; on the rise and fall of the field [92]. We confirm this also for the XUV+IR setup by similar calculations. By postulating that the integral in Eq. (7.9) can be replaced by a sum over all times of stationary phase, t_i, we get

$$c(\varepsilon) = -\mathrm{i}p_{\varepsilon,a} A_0 \sum_i h(t_i) \sqrt{\frac{2\pi\mathrm{i}}{f''(t_i)}} \mathrm{e}^{\mathrm{i}f(t_i)}, \tag{7.11}$$

where we have defined the auxiliary functions for ionization, $h(t)$, phase $f(t)$, and the second time derivative of the phase, $f''(t)$,

$$h(t) = \mathrm{e}^{-\frac{\Gamma(\Omega)}{2} G_\Omega(t,\tau_\Omega)}, \tag{7.12}$$

$$f(t) = (\varepsilon - \varepsilon_a - \Omega)t + \Delta(\omega) G_\omega(t,\tau_\omega), \tag{7.13}$$

$$f''(t) = \frac{\mathrm{d}^2 f}{\mathrm{d}t^2} = -\frac{4\Delta(\omega)t}{\tau_\omega^2} g_\omega^2(t,\tau_\omega). \tag{7.14}$$

The times t_i that contribute to Eq. (7.11) are then found when the phase is stationary,

$$\frac{\mathrm{d}f}{\mathrm{d}t} = \varepsilon - \varepsilon_a - \Omega + \Delta(\omega) g_\omega(t,\tau_\omega) = 0, \tag{7.15}$$

and by solving Eq. (7.15) for time, we obtain that ionization occurs at two instances separated by a delay t_d,

$$t_i = \pm\frac{t_\mathrm{d}}{2} = \pm\tau_\omega \sqrt{\ln\left(\sqrt{\frac{\Delta(\omega)}{\varepsilon_a + \Omega - \varepsilon}}\right)}, \tag{7.16}$$

where the ionization instances are referenced from $t = 0$, which is the point in time where the ponderomotive shift is maximum. The two ionization instances are depicted in Fig. 20 for a specific kinetic energy of the photoelectron. The dependence on the final kinetic energy, as given in Eq. (7.16), gives rise to modulations along the energy axis.

The result in Eq. (7.16) further shows that dynamical interference makes the relation between ionization instances and photoelectron kinetic energy accessible by controlling the intensity of the assisting IR field. In Fig. 21 we show the model of laser-assisted dynamical interference in Eq. (7.9) together with the SPA result in Eq. (7.11). The SPA result is only shown for the kinetic energy range where the real solutions of t_i are defined. The discrepancies at high and low kinetic energies may be alleviated by considering higher-order derivatives of the stationary phase. We note that the SPA result agrees with the model in the region where t_d grows linearly.

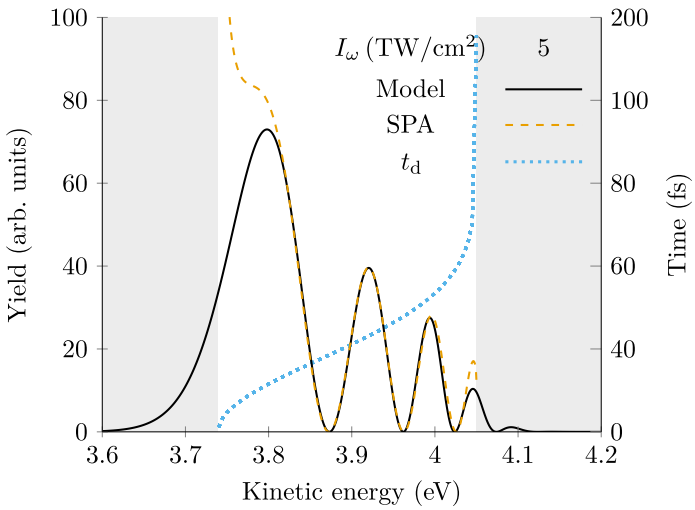

Figure 21: The model of dynamical interference by LAP in Eq. (7.9) in neon $2p$ compared to the SPA result in Eq. (7.11). The relation between kinetic energy and delay between the ionization instances is shown on the second y-axis.

Since most of the ionization occurs when the IR is brightest, and the U_p shift is the strongest, the lowest peak in the kinetic energy spectrum is the most prominent, with the height of the peaks decreasing with kinetic energy. According to the rule of thumb that is discussed in Sec. 7.3, the zeroth contribution to the peaks is of the order

$$c_{\mathbf{k}}^{(0)} \sim J_0\left(\frac{\mathbf{k}\cdot\mathbf{A}_0}{\omega}\right). \tag{7.17}$$

By tuning the intensity of the IR field, the relative peak strengths in the interference pattern can be controlled.

Finally, the *type* of interference that occurs can be depends on the choice of the envelopes. If the IR field is varying (e.g. Gaussian) and equally long as the XUV field, the interference pattern is of dynamical-interference type as explained above. If, on the other hand, the IR field is chosen to have a flat-top envelope, the interference pattern will be of a Ramsey

type [82]. For overlapped pulses, the major part of ionization due to the XUV field happens when the IR is turned on and the photoelectron is shifted down by the ponderomotive energy of the IR, but some ionization happens on the flanks of the XUV pulse, when the flat-top IR is turned off. This will give a photoelectron distribution that consists of two parts: (i) a large peak with no interference shifted down by the ponderomotive energy of the IR, and (ii) a smaller peak with interference fringes centered about the unshifted kinetic energy. The dark period, which in a standard Ramsey-type experiment is a free evolution of the atom in between two illumination periods, is now due to the photoelectron being pulled down to lower kinetic energy. During the dark period the phase evolves as a function of the energy of the bound state and on the ac stark shift of the IR. The electrons that are released after the turn off of the IR field will therefore interfere with the electrons that were released before the turn on. This situation is illustrated in Fig. 22. In the schematic in Fig. 22a, we illustrate the dark phase by the shaded gray background, and the U_p shift applied to the bound state. The instantaneous intensity of the IR field is shown by the color of the bound state, ranging from black (low) to orange (high). The corresponding photoelectron spectrum, retrieved using TDCIS is shown in Fig. 22b, is shown on a relative energy axis centered about the kinetic energy estimate of the multiphoton extension of the photoelectric effect in Eq. (1.3), denoted $\langle E_k^0 \rangle$.

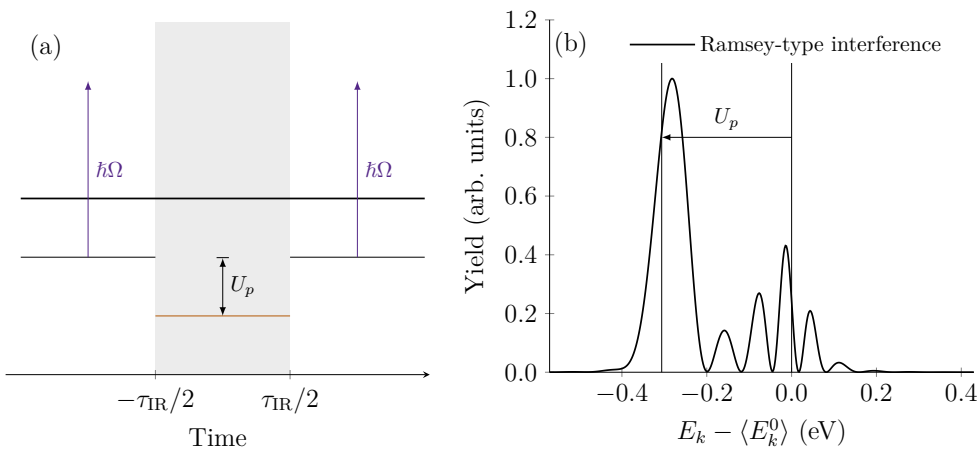

Figure 22: Ramsey-type dynamical interference controlled by a strong flat-top IR field, which is turned on and off during photoionization. (a) Diagrammatic representation. The dark period is shaded gray and the instantaneous IR intensity is illustrated with the color of the bound state, with black representing low and orange representing high. (b) Photoelectron spectrum with the kinetic energy axis relative to the estimate of the multiphoton extension of the photoelectric effect, $\langle E_k^0 \rangle$.

7.3 A rule of thumb for multiphoton interaction phases

The third LAP regime in this thesis is the combination of multiple weak XUV fields and a weak assisting IR field. This is a very common setup for attosecond interferometric ex-

periments that we study by deriving a rule of thumb, introduced in Paper II. The rule of thumb is capable of explaining the general phase and amplitude effects in a broad selection of experiments. The derivation of the rule of thumb was worked out for Paper II and is given below.

To derive the rule of thumb, we assume that the probe field is infinitely long. We also assume that the XUV field only contributes through absorption of photons, and that the role of the IR field is to dress the continuum. We can therefore make use of the rotating-wave approximation, see e.g. Ref. [22], and write the vector potential as

$$A(t) = \frac{1}{2\mathrm{i}} \sum_i A_{\Omega_i,0} \exp[-\mathrm{i}(\Omega_i t - \delta_i)] F(t,\tau) + A_{\omega,0} \sin(\omega t - \varphi). \tag{7.18}$$

The Volkov phase acquired in the continuum due to the action of the electric field is largely due to the laser field since the rapid modulations of the ionizing XUV field result in small integral values. We therefore approximate the Volkov action, for instance in velocity gauge, Eq. (6.5), as

$$\begin{aligned} \mathrm{e}^{\mathrm{i}\mathcal{S}(\mathbf{k},t)} &= \exp\left[\mathrm{i}\int^t \mathrm{d}t' \left(\varepsilon_k + \mathbf{k}\cdot\mathbf{A}_{\omega,0}\sin(\omega t' - \varphi) + \frac{A_{\omega,0}^2}{2}\sin^2(\omega t' - \varphi)\right)\right] \\ &= \exp\left[\mathrm{i}(\varepsilon_k + U_p)t\right] \exp\left[-\mathrm{i}\frac{\mathbf{k}\cdot\mathbf{A}_{\omega,0}}{\omega}\cos(\omega t - \varphi)\right] \\ &\times \exp\left[-\mathrm{i}\frac{U_p}{2\omega}\sin\left(2(\omega t - \varphi)\right)\right]. \end{aligned} \tag{7.19}$$

The two oscillating terms in Eq. (7.19) can be simplified by using the Jacobi–Anger expansions, see Ref. [93],

$$\exp(\mathrm{i}z\cos\phi) = \sum_{n=-\infty}^{\infty} \mathrm{i}^n J_n(z)\exp(\mathrm{i}n\phi), \tag{7.20a}$$

$$\exp(\mathrm{i}z\sin\phi) = \sum_{n=-\infty}^{\infty} J_n(z)\exp(\mathrm{i}n\phi), \tag{7.20b}$$

to obtain

$$\begin{aligned} \mathrm{e}^{\mathrm{i}\mathcal{S}(\mathbf{k},t)} = &\sum_{n=-\infty}^{\infty} (-\mathrm{i})^n \exp(\mathrm{i}n\varphi) J_n\left(\frac{\mathbf{k}\cdot\mathbf{A}_{\omega,0}}{\omega}\right) \sum_{m=-\infty}^{\infty} \exp[\mathrm{i}2m\varphi] J_m\left(\frac{U_p}{2\omega}\right) \\ &\times \exp[\mathrm{i}(\varepsilon_k + U_p - n\omega - 2m\omega)t]. \end{aligned} \tag{7.21}$$

The sum over n and m indices have been reversed with the only change in the sign of the factors $\exp[\mathrm{i}n\varphi]$ and $\exp[-\mathrm{i}n\omega t]$, and respectively $\exp[\mathrm{i}\delta]$ and $\exp[-\mathrm{i}\Omega t]$. This is due to

the relation

$$(-\mathrm{i})^{-n} J_{-n} = (-\mathrm{i})^{n} J_n. \tag{7.22}$$

We note that this type of manipulation of the action in continuous fields is a common technique to study laser-assisted processes with many applications [94]. By inserting the Volkov state with the action given by Eq. (7.21) into the KFR expression in Eq. (6.33), we arrive at

$$\begin{aligned} c_{\mathbf{k}} \approx \frac{1}{2} \sum_{n=-\infty}^{\infty} (-\mathrm{i})^n \exp[\mathrm{i}n\varphi] J_n \left(\frac{\mathbf{k} \cdot \mathbf{A}_{\omega,0}}{\omega} \right) \\ \times \sum_{m=-\infty}^{\infty} \exp[\mathrm{i}2m\varphi] J_m \left(\frac{U_p}{2\omega} \right) \langle \mathbf{k} | \hat{p}_z | a \rangle \exp[\mathrm{i}\delta] \\ \times \int \mathrm{d}t \; A_{\Omega,0} F(t) \exp[\mathrm{i}(\varepsilon_k + I_p + U_p - \Omega - n\omega - 2m\omega)t], \end{aligned} \tag{7.23}$$

We have here made the assumption that only the XUV field contributes to ionization, and that the term quadratic in the vector potential in Eq. (6.33) can be neglected. As mentioned in Sec. 6.3, this assumption holds for photoelectrons of high kinetic energy ejected along or antiparallel to the polarization axis. If the rule of thumb is to be applied to photoelectron ejected perpendicular to the polarization axis, the quadratic term would need to be included. The ionization potential I_p is further introduced because we choose the zero-point energy at the ionization threshold. For small ponderomotive shifts, $U_p \ll 2\omega$, the zeroth term of the sum over m is dominant and is kept, but the other vanish. From Eq. (7.23) a simple rule of thumb can be extracted by identifying some key factors. The dipole matrix element and the time integral are collected as the *common* elementary photoionization process

$$f_{\mathbf{k}a}^{(n)} = \frac{1}{2} \langle \mathbf{k} | \hat{p}_z | a \rangle \exp[\mathrm{i}\delta] \int \mathrm{d}t \; A_{\Omega,0} F(t) \exp[\mathrm{i}(\varepsilon_k + I_p + U_p - n\omega - \Omega)t], \tag{7.24}$$

for a given exchange of n laser photons. The complex amplitude for an exchange of n photons can hence be written as

$$c_{\mathbf{k}}^{(n)} \approx (-\mathrm{i})^{|n|} J_{|n|} \left(\frac{\mathbf{k} \cdot \mathbf{A}_{\omega,0}}{\omega} \right) \exp[\mathrm{i}n\varphi] f_{\mathbf{k}}^{(\mathrm{pump})}, \tag{7.25}$$

where the directionality of the photoelectron measured from the polarization axis is contained in the Bessel function $J_{|n|}$. We identify $\arg[(-\mathrm{i})^{|n|}] = -|n|\pi/2$ as a multiphoton *interaction* phase shift that accumulates with every continuum light–matter interaction. The interaction phase appears explicitly from the *first* Jacobi–Anger expansion in Eq. (7.20a), due to the arbitrary choice of a sine-type vector potential, which we opt for in Eq. (7.18). We note that also Kuchiev opts for this choice of the vector potential in Ref. [95]. This convention differs from the convention used in e.g. the development of

the soft-photon approximation in Ref. [96], where a cosine vector potential is used. If a cosine vector potential is used, the *second* Jacobi–Anger expansion in Eq. (7.20b), where the factor i^n is implicit in the field, must be employed. The phase convention for the fields hence changes the phases of the transition amplitudes, which has caused some confusion, although both descriptions provide equivalent predictions [97–99]. In Eq. (11) in Ref. [96], the nth component of the S-matrix amplitude depends on whether the net exchange of photons is positive or negative, whereas the accumulation of interaction phases in Eq. (7.25) is equivalent for absorption and emission because the use of relation in Eq. (7.22). When multiphoton transitions are studied, we find that the present phase convention transparently reveals the phases of the transitions.

The identification of the interaction phase shift is the key point of Paper II, since it explains how strong carrier-envelope phase shifts get imprinted on the photoelectron signal for interferometric experiments with an unbalanced number of photons. The rule of thumb therefore generally provides qualitative explanations for multiphoton phase shifts in a variety of interferometric experiments in attosecond and free-electron laser experiments. For a quantitative agreement with the experimental results, energy-dependent phases [2] and continuum–continuum phases [80, 100, 101], must be considered.

8 Interferometric photoelectron scenarios

In this section, we study three interferometric experiments from attosecond and free-electron laser sciences that make use of multiphoton transitions in the continuum to interfere ionization pathways. These experiment enable characterization of attosecond pulses and may be used to provide information on the target species and the ionization dynamics. The first experiment is the famous Reconstruction of Attosecond Beating By two-photon Transitions (RABBIT) method [102, 103]. This method combines a comb of XUV pulses, which corresponds to odd harmonics of a fundamental IR field in the frequency domain, and a weak synchronized IR field to make photoelectrons interfere. Experimentally, the IR field synchronization is controlled by a delay stage that determines the phase of the IR field relative to the XUV field, $\varphi = \omega\tau$. For practical reasons, we instead directly alter the carrier-envelope phase (CEP) by tuning φ. Both pathways contain two interactions with the fields, and the interferometric arms are therefore balanced in the number of interactions. We contrast the RABBIT experiment to two experiments where the number of interactions in the two interferometric arms are instead unbalanced. The second experiment, performed by Laurent et al. [104], is a laser-assisted photoionization experiment where photoelectrons are ejected using a comb of even and odd harmonics, generated by means of two-color high-harmonic generation ($\omega/2\omega$ HHG), see Ref. [105, 106], coupled together by the fundamental IR field. The third experiment, performed by Maroju et al. [107], is a free-electron laser experiment, where two FEL beams with a photon energy difference of

$\Delta\Omega^{\mathrm{FEL}} = \Omega^{\mathrm{FEL}}_{>} - \Omega^{\mathrm{FEL}}_{<} = 3\hbar\omega$ are coupled by a laser field of photon energy $\hbar\omega$. Since the photoelectrons may reach a certain kinetic energy with either an odd or an even number of interactions with photons in the two latter experiments, there is a mixing of orbital parity. All these experiments can be replicated with a vector potential, linearly polarized along the z-axis, of the form given in Eq. (7.3).

8.1 Example 1: Odd high-order harmonics (RABBIT)

The RABBIT method is an interferometric method where photoelectrons ejected by absorption of photons of XUV wavelength in a comb of odd harmonics, often generated by means of HHG, are interfered by the successive interaction with a synchronized, fundamental, IR field. By multicolor ionization of the atom, the photoelectron spectrum displays a comb of peaks that correspond to the harmonics and is separated by twice the fundamental IR photon energy and, labeled H_{2q+1}. In between the harmonic peaks, sideband peaks SB_{2q} form, which are populated by either absorption of an IR photon from H_{2q-1} or by emission of an IR photon from H_{2q+1}. The intensity signal of the sidebands modulate as a function of the delay between the harmonics and the IR field [108], and by measuring the relative phase between two consecutive sidebands, the RABBIT method has successfully been used to characterize attosecond pulse trains [102, 109, 110], and to probe the dynamics of the ionized system itself; for instance in atoms [73, 111] and molecules [112].

As mentioned above, RABBIT is exceptional since it has a balanced number of interactions in its interferometric arms, and an odd number of interactions in the continuum are needed to reach a sideband. The ionization pathways are as follows. To lowest order, either one absorption or one emission of a laser photon is involved. To reach a harmonic peak on the other hand, an even number of interactions in the continuum are instead needed. To second order, either zero interactions with the laser field (direct ionization), or two interactions with the laser field (redistribution from neighboring harmonic peaks), are needed. In Fig. 23, we show the ionization pathways in a RABBIT experiment, together with a spectrogram measured along the polarization axis that shows the modulations of the sidebands and the harmonics as a function of CEP.

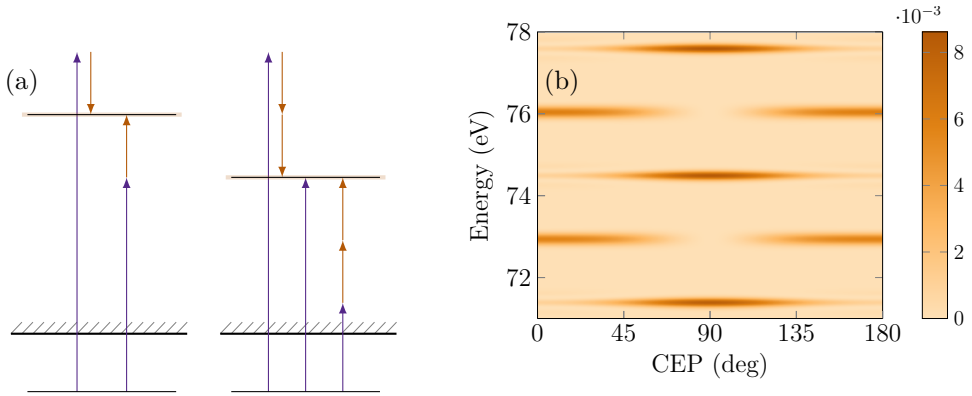

Figure 23: (a) Ionization pathways of the sidebands and the harmonics in a RABBIT experiment, respectively. (b) The corresponding photoelectron spectrogram measured along the polarization. The sidebands and the harmonics modulate off phase.

To model the modulations in Fig. 23b, we turn to the rule of thumb derived in Sec. 7.3, Eq. (7.25). We apply the rule of thumb to RABBIT in accordance with the pathway diagrams in Fig. 23a to get the complex amplitudes

$$c_{\mathbf{k}}^{\mathrm{SB}} \approx -\mathrm{i}J_1 \mathrm{e}^{\mathrm{i}\varphi} - \mathrm{i}J_1 \mathrm{e}^{-\mathrm{i}\varphi}, \tag{8.1a}$$

$$c_{\mathbf{k}}^{\mathrm{H}} \approx J_0 - J_2 \mathrm{e}^{\mathrm{i}2\varphi} - J_2 \mathrm{e}^{-\mathrm{i}2\varphi}, \tag{8.1b}$$

from which the probability densities are readily given by

$$|c_{\mathbf{k}}^{\mathrm{SB}}|^2 \approx 4J_1^2 \cos^2\varphi, \tag{8.2a}$$

$$|c_{\mathbf{k}}^{\mathrm{H}}|^2 \approx J_0^2 + 4J_0J_2 - 8J_0J_2 \cos^2\varphi, \tag{8.2b}$$

which has the interpretation that a sideband in RABBIT is generated when the attosecond pulses overlap with the extremum of the IR electric field. The total probability is conserved, $|c_{\mathbf{k}}^{\mathrm{SB}}|^2 + |c_{\mathbf{k}}^{\mathrm{H}}|^2 = 1$, which can be easily seen by expanding the Bessel functions for weak fields: $J_0(2\xi) = 1 - \xi^2 + \mathcal{O}\left(\xi^4\right)$, $J_1(2\xi) = \xi + \mathcal{O}\left(\xi^3\right)$ and, $J_2(2\xi) = \xi^2/2 + \mathcal{O}\left(\xi^4\right)$.

The interaction phase in Eq. (8.1a) appears in both the absorption term and the emission term of the sideband amplitude and does therefore not contribute to the probability density in Eq. (8.2a). This may at first glance make the interaction phase seem unnecessary to describe the dynamics in a RABBIT experiment. The interaction phase is however needed to ensure that the redistribution of population between sideband and harmonic peaks is correctly described, and the inclusion of the interaction phase explains the conservation of probability in continuum transitions. We note that third-order perturbation theory is required to each consistent result in second order due to interference effects between different orders.

8.2 Example 2: Even and odd high-order harmonics

In a LAP experiment with an attosecond pulse train of even and odd harmonics coupled by a weak IR probe field, Laurent et al. showed that the asymmetric electron emission along the polarization axis of atomic targets can be controlled on an attosecond timescale [104]. The train of harmonics, generated by a combination of 800 nm and 400 nm in an $\omega/2\omega$ HHG, cf. Ref. [105, 106], ionize argon atoms under dressing of the weak IR field to create energy-degenerate electron wave packets with a mix of odd and even parities. The interference between photoelectrons of different parities resulted in asymmetric emission along the polarization axis, which we call an up–down asymmetry, and depending on the relative delay between the IR and the train of harmonics, they demonstrated a control of the asymmetric electron emission on an attosecond timescale. The method has later been extended for attosecond pulse characterization [113].

Based on a checkerboard pattern in the photoelectron spectrum, they proposed that there is a phase shift of $\delta = -\pi/2$ between even and odd harmonics generated this way [104]. The general view at the time was that $\omega/2\omega$ HHG generates one attopulse every IR cycle, see Ref. [106], but this idea requires that the odd and the even harmonics have zero relative phase. In Paper II we confirm that a phase shift of $\delta = -\pi/2$ between the odd and the even harmonics leads to a checkerboard pattern in the photoelectron spectrum. In Fig. 24 we show a KFR calculation of the experiment by Laurent et al. generated by odd and even harmonics with a relative phase difference of $\delta = -\pi/2$. We show in Fig. 24a the photoelectron spectrogram along the polarization axis, where even and odd harmonics modulate off phase. We further show the up–down asymmetry in Fig. 24b where the difference between photoelectrons emitted parallel and anti-parallel to the polarization axis, $S_+(\varphi) - S_-(\varphi)$, are shown.

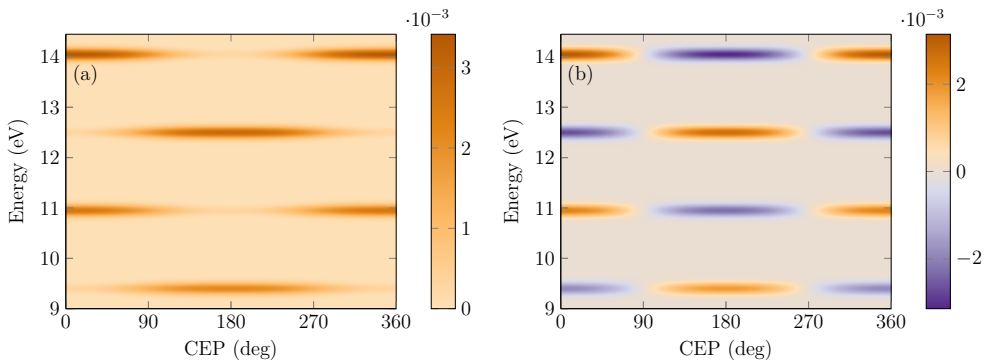

Figure 24: (a) Photoelectron spectrogram along the polarization, S_+, of the experiment by Laurent et al [113]. (b) Asymmetry between the photoelectrons emitted along, and anti-parallel to, the polarization axis, $S_+(\varphi) - S_-(\varphi)$.

We further found in Paper II that the limitation to one- and two-photon ionization pro-

cesses is insufficient for this type of experiment. Although the weak IR coupling, also the adjacent harmonic peaks, coupled by two IR photons, must be considered in order to count the photon interactions consistently. The rule of thumb in Eq. (7.25) applied to this setup yields the following expression for the transition amplitudes for the laser-assisted harmonics:

$$\begin{aligned} c_{\mathbf{k}}^{(\mathrm{odd})} = &- J_2 \exp[-\mathrm{i}2\varphi] - \mathrm{i}J_1 \exp[-\mathrm{i}(\varphi - \delta)] \\ &+ J_0 - \mathrm{i}J_1 \exp[\mathrm{i}(\varphi + \delta)] - J_2 \exp[\mathrm{i}2\varphi], \end{aligned} \tag{8.3a}$$

$$\begin{aligned} c_{\mathbf{k}}^{(\mathrm{even})} = &- J_2 \exp[-\mathrm{i}(2\varphi - \delta)] - \mathrm{i}J_1 \exp[-\mathrm{i}\varphi] \\ &+ J_0 \exp[\mathrm{i}\delta] - \mathrm{i}J_1 \exp[\mathrm{i}\varphi - J_2 \exp[\mathrm{i}(2\varphi + \delta)]. \end{aligned} \tag{8.3b}$$

The phase shift between odd harmonics and even harmonics is modeled by the introduction of δ in the even harmonics. This yields the probabilities

$$|c_{\mathbf{k}}^{(\mathrm{odd})}|^2 = 1 + 2\xi \sin(\delta)\cos(\varphi) + \mathcal{O}(\xi^3), \tag{8.4a}$$

$$|c_{\mathbf{k}}^{(\mathrm{even})}|^2 = 1 - 2\xi \sin(\delta)\cos(\varphi) + \mathcal{O}(\xi^3). \tag{8.4b}$$

This expression differs from that of Laurent et al. in Ref. [104] by the absence of a 2ω modulation[16] – the RABBIT term – and with the rule of thumb an explanation to why this term should not be present is readily given. This term would come from the interference of the two J_1 terms by absorption or emission of one IR photon like in RABBIT,

$$c_{\mathbf{k}}^{(2\omega)} = -\mathrm{i}J_1 \exp(-\mathrm{i}\varphi) - \mathrm{i}J_1 \exp(\mathrm{i}\varphi), \tag{8.5a}$$

$$|c_{\mathbf{k}}^{(2\omega)}|^2 = \frac{\xi^2}{2}\left(1 + \cos(2\varphi)\right) + \mathcal{O}\left(\xi^4\right). \tag{8.5b}$$

The complementary signal is then given by the direct ionization term and the two terms from including the two adjacent harmonics,

$$c_{\mathbf{k}}^{(\mathrm{compl.})} = -J_2 \exp[-\mathrm{i}(2\varphi - \delta)] + J_0 \exp[\mathrm{i}\delta] - J_2 \exp[\mathrm{i}(2\varphi + \delta)], \tag{8.6a}$$

$$|c_{\mathbf{k}}^{(\mathrm{compl.})}|^2 = 1 - \frac{\xi^2}{2}\left(1 + \cos(2\varphi)\right) + \mathcal{O}\left(\xi^4\right). \tag{8.6b}$$

By expanding the RABBIT term in Eq. (8.5b) and the complementary term in Eq. (8.6b) to second order in the interaction, it is seen that they cancel. This hinges on the assumption that the harmonics are equally strong. In Fig. 25, the RABBIT and the complementary pathways are shown together with the modulations to show the cancellation. In Fig. 25 we show the ionization pathways for the RABBIT signal and the complement signal from Eq. (8.5)–(8.6). Their opposite modulations are shown in Fig. 25c.

[16] As mentioned in the beginning of Sec. 8, the relative phase difference between the train of harmonics and the IR field, $\varphi = \omega\tau$, is controlled by changing the delay. The 2ω modulation refers to a modulation which occurs at twice frequency of the IR field.

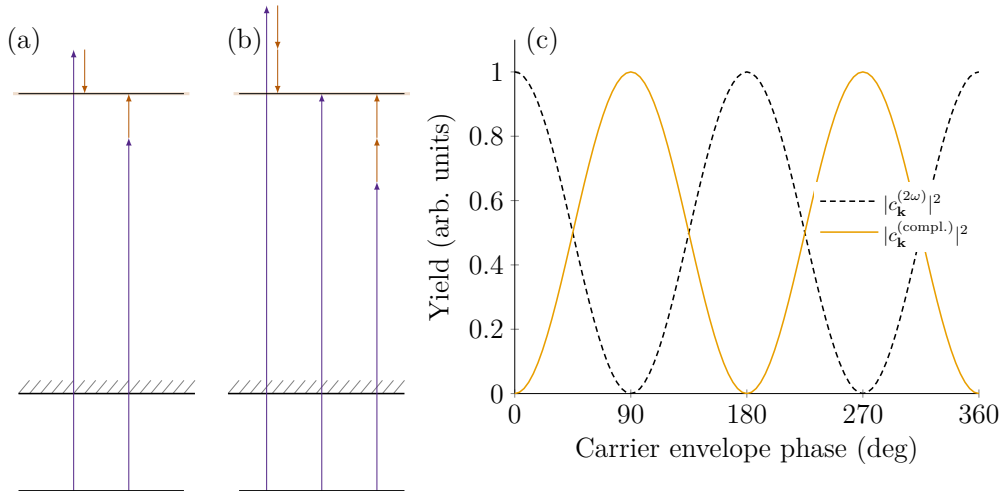

Figure 25: (a) The two-photon RABBIT pathway in Eq. (8.5) to an odd harmonic peak, and (b) the complementary pathway in Eq. (8.6). (c) The modulation of the odd harmonic peak due to the interactions in (a) and (b). At equally strong harmonics, the two terms cancel.

The KFR result in Fig. 24 agrees with TDCIS (not shown) for photoelectrons along or anti-parallel to the polarization axis. However, we found in Paper II that the general angular distribution differed between the two theories, which implies that methods beyond KFR are required to correctly describe the photoionization dynamics in arbitrary emission angles.

8.3 Example 3: Free-electron laser radiation with $3n$ harmonics

Our third example of a LAP experiment is an FEL experiment performed at FERMI by Maroju et al. [107]. Here two FEL beams with an energy spacing of $\Delta\Omega^{\mathrm{FEL}} = \Omega_{>}^{\mathrm{FEL}} - \Omega_{<}^{\mathrm{FEL}} = 3\hbar\omega$ are used to ionized neon atoms and a synchronized weak IR field with angular frequency ω couple the two harmonic peaks to *twin sidebands*. The two twin sidebands modulate off phase by $-\pi/2$ and display an up–down asymmetry[17]. In this regard, the experiment can therefore be viewed as a *higher-order* version of the even–odd orbital parity-mixing experiment above by Laurent et al. [104]. The photoionization pathways and the spectrogram along $\theta = 0$ are shown in Fig. 26.

[17] One of the major motivations for Paper II was our interest in understanding the origin of the phase shift between the two twin sidebands. In a small passage in Ref. [107], this shift is mentioned as "*trivial*". Perhaps it was not trivial *enough* for us, which we are very thankful for.

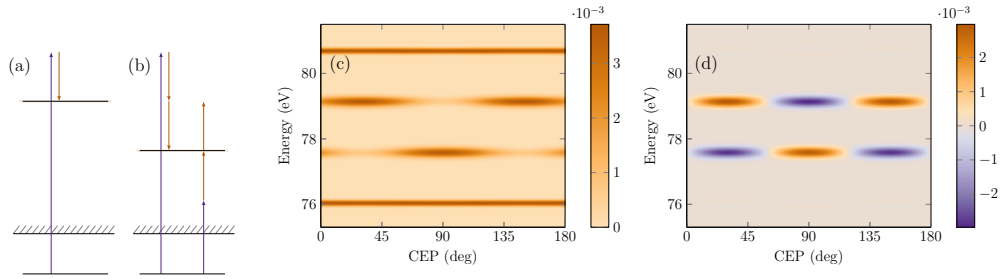

Figure 26: Photoionization pathways to the (a) upper twin sideband, and (b) the lower twin sideband, in the experiment by Maroju et al. [107]. (c) Corresponding photoelectron spectrogram that shows the twin sideband (reprinted from Paper II), and (d) the asymmetry between the photoelectrons emitted along, and anti-parallel to, the polarization axis, $S_+(\varphi) - S_-(\varphi)$.

Using the rule of thumb, we therefore model the transition amplitudes as

$$c_{\mathbf{k}}^{(\text{high})} = -\mathrm{i}J_1 \exp[-\mathrm{i}\varphi] - J_2 \exp[\mathrm{i}2\varphi], \tag{8.7a}$$

$$c_{\mathbf{k}}^{(\text{low})} = -J_2 \exp[-\mathrm{i}2\varphi] - \mathrm{i}J_1 \exp[\mathrm{i}\varphi], \tag{8.7b}$$

where we have assumed that the elementary photoionization processes are equal for the two FEL harmonics: $f_{\mathbf{k}}^{>} = f_{\mathbf{k}}^{<} = 1$. Similar to RABBIT, the two sidebands are populated from two pathways, but with a difference in the number of interactions in the upper and lower pathways. This leads to the following probabilities

$$|c_{\mathbf{k}}^{(\text{high})}|^2 = \frac{\xi^2}{4} + \frac{\xi^3}{8}\sin(3\varphi) + \mathcal{O}(\xi^4), \tag{8.8a}$$

$$|c_{\mathbf{k}}^{(\text{low})}|^2 = \frac{\xi^2}{4} - \frac{\xi^3}{8}\sin(3\varphi) + \mathcal{O}(\xi^4), \tag{8.8b}$$

and it is the unbalanced pathways that lead to the phase shift between the two sidebands. With the convention of a sine-type vector potential, the interpretation is that the phase shift comes from the interaction phase. Similar to Maquet et al., Maroju et al. also employ the cosine phase convention for the field in Ref. [107], and in Ref. [114], Maroju et al. derive expressions equivalent to Eq. (8.8). Further, in Ref. [115], coherent control of the population of the twin sidebands on an attosecond time scale have been shown.

9 Above-Threshold Ionization

Above-threshold ionization is the multiphoton ionization process in which the field is strong enough such that the atom absorbs more than the minimum number of photons to overcome the ionization threshold. Typically, this is described by the reaction

$$A + q\gamma \to A^+ + e^-, \tag{9.1}$$

where q is the number of absorbed photons γ with energy $\hbar\omega$. This process was first revealed by Agostini et al. [7], see schematic in Fig. 2, in which xenon atoms were illuminated by a strong laser with a photon energy that would require six photons to be absorbed for an electron to be ejected. In the photoelectron spectrum, they however measured two peaks: one corresponding to absorption of six photons, and one corresponding to absorption of seven photons. This indicated that the photoelectron had absorbed a photon in the continuum. We have shown ATI spectra in this thesis, e.g. in hydrogen in Fig. 9 and Fig. 10, in helium in Fig. 13, and neon in Fig. 11, and will in this section give general comments on the ATI spectra that we have calculated in this thesis[18].

Photoelectrons measured in an ATI experiment are often classified as either *direct* electrons or *rescattered* electrons. Direct electrons are the photoelectrons that are ejected by absorption of a number of photons and do not interact again with the ion after the ionization event, while the rescattered electrons are driven back to the ion, off which they may scatter to attain a higher kinetic energy [52]. The classical kinetic energy bound for direct electrons is found by calculating the drift energy of an electron in a monochromatic field [52], and depends on the polarization of the field. For linear polarization, the direct electron may attain at maximum a kinetic energy of $E_{\mathbf{k}} = 2U_p$, while for circular polarization the bound is already at $E_{\mathbf{k}} = U_p$. Quantum mechanically, this bound is not as strict, but the classical limits are useful for assignation of cut offs in ATI spectra. The importance of rescattering in ATI was recognized by Kuchiev [95] and implemented later by several authors [116, 117]. Above a kinetic energy of $2U_p$, most of the photoelectrons have scattered off the ion, and they form a plateau of ATI peaks with a cutoff at $10U_p$ [118, 119]. In this thesis, we calculate ATI spectra within the TDCIS theory and within the KFR theory. As discussed in conjunction to the theory of KFR, Sec. 6.3, the limitation of not including any interaction with the photoelectron and the ion restricts the method to direct ionization without taking into account rescattering off the ion. We have focused on the experiment by Zipp et al. [120] where the ATI process is probed by a field of half the frequency. The basis for this experiment, and how it relates to RABBIT is discussed in Sec 9.1.

9.1 Two-color ($2\omega/\omega$)

An experiment that in a clear way relates strong-field physics to attosecond physics is the $2\omega/\omega$ ATI experiment by Zipp et al. [120]. Argon atoms are photoionized by ATI using a frequency-doubled 400 nm field and probed by the fundamental 800 nm field, both linearly polarized along the same axis. The ATI process creates photoelectron population in the continuum with a spacing of 2ω, and the probe field creates sidebands that may be

[18] We mention that ATI is sometimes referred to experiments where the photon energy is smaller than the ionization potential of the atom such that multiple photons needs to be absorbed for ionization to happen. We include also in the definition experiments where one photon would be enough to ionize, but where additional photons are absorbed in the continuum.

populated by either absorption from the ATI peak below or emission from the ATI peak above. The setup for this experiment is depicted in Fig. 27 by pathway diagrams. We show in Fig. 27a the photoionization pathways to an ATI sideband and in Fig. 27b the photoionization pathways to an ATI peak, together with CEP modulation of the third ATI sideband compared to a RABBIT sideband in Fig. 27c. When the two fields are delayed relative each other, modulations of the sidebands (and of the ATI peaks) appear with a period equal to that of the RABBIT experiment[19], but with a phase shift due to the interaction phase.

It is remarkable that despite the very different premise for this experiment, being based on the nonlinear ATI process rather than the linear photoionization process ignited by the XUV harmonics, this experiment have much in common with the RABBIT experiment. In fact, we use the same definition for the vector potential as in the LAP experiment, Eq. (7.16), but with the $\Omega = 2\omega$ being a frequency-doubled field of an amplified Ti:sapphire laser with angular frequency ω.

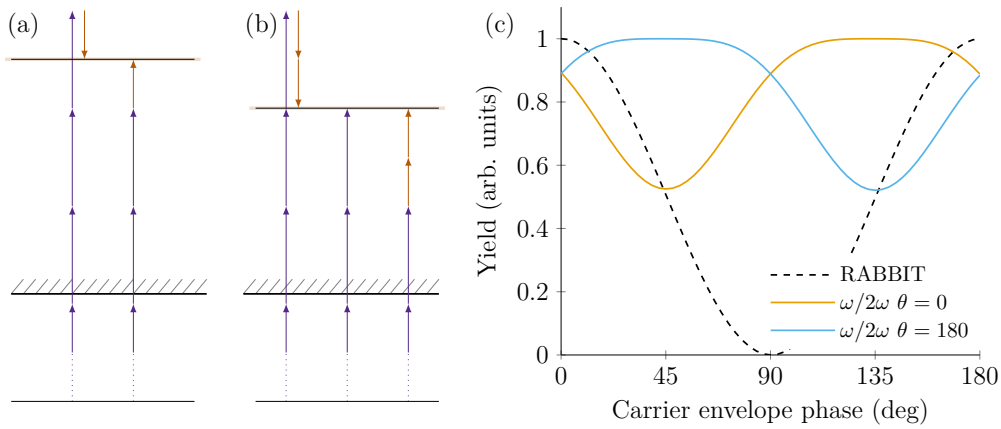

Figure 27: Photoionization pathways of the $\omega/2\omega$ experiment by Zipp et al. [120] for (a) sideband and (b) ATI peaks. (c) Comparison of the CEP modulation of the $\omega/2\omega$ sideband for $\theta = 0$ and $\theta = 180$ to CEP modulation in a RABBIT sideband along $\theta = 0$.

To model this experiment, we note that for each absorbed photon in the ATI process, an interaction phase is accumulated according to the rule of thumb. The upper ATI peak has thus acquired a $-\pi/2$ from the surplus of one interaction in the continuum compared to the lower ATI peak. The rule of thumb then gives the following contributions to the

[19] The period is only equal to the RABBIT period provided that the delay stage is implemented in the 800 nm field, as described below.

transition amplitudes,

$$c_{\mathbf{k}}^{(\mathrm{SB})} = -iJ_1 \exp\left[-i\left(\varphi + \frac{\pi}{2}\right)\right] - iJ_1 \exp[i\varphi], \tag{9.2a}$$

$$c_{\mathbf{k}}^{(\mathrm{ATI})} = -J_2 \exp\left[-i\left(2\varphi + \frac{\pi}{2}\right)\right] + J_0 - J_2 \exp\left[i\left(2\varphi + \frac{\pi}{2}\right)\right], \tag{9.2b}$$

where photoelectrons in in the *up* directions are considered. Similar to the experiments by Laurent et al. [104], and Maroju et al. [107], there is an up–down asymmetry. The probabilities are then given by

$$|c_{\mathbf{k}}^{(\mathrm{SB})}|^2 = \xi^2 \cos^2\left(\frac{\pi}{4} + \varphi\right) + \mathcal{O}\left(\xi^4\right), \tag{9.3a}$$

$$|c_{\mathbf{k}}^{(\mathrm{ATI})}|^2 = 1 - \xi^2 \cos^2\left(\frac{\pi}{4} + \varphi\right) + \mathcal{O}\left(\xi^4\right), \tag{9.3b}$$

where there is a phase shift $-\pi/4$ compared to the RABBIT modulations, which indeed is seen in our simulations in Paper II. This $\pi/4$ shift compared to the RABBIT modulations is on the *absolute* scale and can therefore only be seen if the experiment is simultaneously compared to a known reference experiment. In Eq. (9.2)-(9.3), we have made the strong assumption that the photoelectron peaks of the ATI comb are comparable in strength before the cut off. We find it remarkable that despite the assumption of equal strength of the adjacent ATI peaks, the rule of thumb is able to reproduce these modulations.

We mention that the amplitudes presented in Eq. (9.2) are retrieved when using the definition of the vector potential presented in Eq. (7.3), with the delay (or in our case CEP) referenced from the 2ω ATI (pump) fields. This coincides with the usual definition for a RABBIT analysis, where the IR field acts as a probe of the XUV pump. Both Zipp et al. [120], and following work by López et al. [98, 99], introduce however the delay/CEP in the 2ω arm, and further use the convention of a cosine vector potential. This seemed to lead to a discrepancy between our work in Paper II and their work. They define the field from the electric field, neglecting the slowly varying envelope,

$$E(t) = E_{2\omega} \sin(2\omega t + \varphi) + E_{\omega} \sin(\omega t), \tag{9.4}$$

which compares to the electric field employed by us in Paper II:

$$E(t) = E_{2\omega} \cos(2\omega t + \pi) + E_{\omega} \cos(\omega t + \pi - \varphi). \tag{9.5}$$

If their definition of the field is used, the sidebands will be located at $\varphi = 0$ and the ATI peaks will be located at $\varphi = \pi$, as opposed to when using the RABBIT field definition where the sidebands are located at $\varphi = \pi/4$ and the ATI peaks at $\varphi = 3\pi/4$. The two results are however equivalent and it is possible to relate them by the transformation $t \to t - \pi/(2\omega) - \varphi/\omega$ [97]. It is our experience that the convention used in this thesis makes the interpretation of attosecond experiments based on LAP or ATI more easy to understand in terms of multiphoton interaction phases.

10 Photoionization from a Rabi-cycling atom at XUV wavelengths

With the high degree of coherence and shot-to-shot reproducibility of seeded free-electron lasers such as FERMI [13], experiments with coherent control of light–matter processes at XUV wavelengths have become possible [121]. This is the subject for Paper IV, where Rabi oscillations in helium atoms at XUV wavelengths were directly observed for the first time. The experiment is performed by illuminating helium atoms with an intense XUV field ($I = 2\times10^{13}\,\mathrm{W/cm^2}$) tuned to the $1s^2\,{}^1S_0 - 1s4p\,{}^1P_1$ transition at $\hbar\omega_{ba} = 23.742\,\mathrm{eV}$, which couples the ground state to the excited state and periodically drives population between the two states. In spite of a large intensity of the XUV field, the ponderomotive energy of the field is low, due to the large central frequency of the XUV field. Yet, we observe in this experiment both weak-field and strong-field features, the latter requiring a theoretical description beyond lowest-order perturbation theory. By absorption of one photon from the excited state or of two photons from the ground state, some electronic population is ejected and recorded in the photoelectron spectrum, where the Rabi dynamics is directly measured. We mention that earlier predictions to indirectly observe Rabi dynamics driven by fields of short wavelengths have been made, in both atoms [122–124] and molecules [125], where coupling between two manifolds of vibrational states rather than two distinct states, lead to an AT splitting in the photoelectron spectrum [126]. In this section, we give a theoretical background to this experiment.

10.1 Rabi dynamics

An important part of Paper IV was to distinguish photoelectrons stemming from the ground state $|a\rangle$ from the electrons stemming from the excited state $|b\rangle$. In order to distinguish between these two ionization paths, we study the Rabi amplitudes in Eq. (1.16), where initially all the population is in the ground state. At resonance, with $\Delta\omega = 0$, the Rabi amplitudes for the ground state and the excited state modulate as

$$a(t) = \cos\frac{\Omega t}{2}, \tag{10.1a}$$

$$b(t) = -\mathrm{i}\sin\frac{\Omega t}{2}, \tag{10.1b}$$

so that the probability of finding the atom in the ground state, shown in Fig. 28a, hence modulates off phase with half a Rabi period compared to the probability of finding the atom in the excited state, shown in Fig. 28b. The relative phases of the amplitudes are shown by the color of the lines. It is seen that after a completed Rabi cycle the atom returns to its previous state, but with a phase shift of π. Given the initial condition that the population is initially in the ground state, the phase jumps occur at every $(n+\frac{1}{2})$th completed period in the ground state, and at every nth completed period in the excited state.

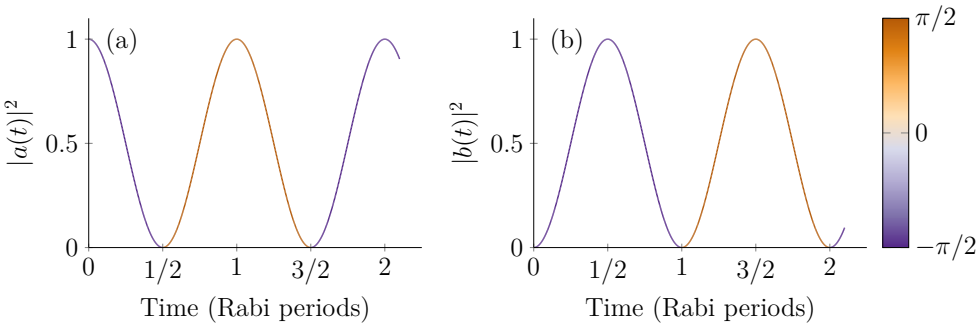

Figure 28: Probability of finding the atom in (a) the ground state and (b) the excited state as a function of time when driving Rabi oscillations at resonance. The acquired phase is shown by the line color.

The frequency-domain correspondence to the Rabi oscillations is an AT doublet, which is separated by the generalized Rabi frequency [25]. In the experiment of Paper IV, the Rabi-oscillating atom is coupled to a continuum by absorption of one photon from the excited state or by absorption of two photons from the ground state, via all other accessible states $1snp$. These two ionization pathways are shown in the photon diagram of Fig. 29. Each photoionization event separately yields a unimodal photoelectron distribution with spectral width determined by the pulse parameters. However, the photoelectrons are ejected with the phase that was acquired during the Rabi oscillation inherited, see Fig. 28, which means that electrons ejected at odd cycles and electrons ejected at even cycles interfere to form an AT doublet.

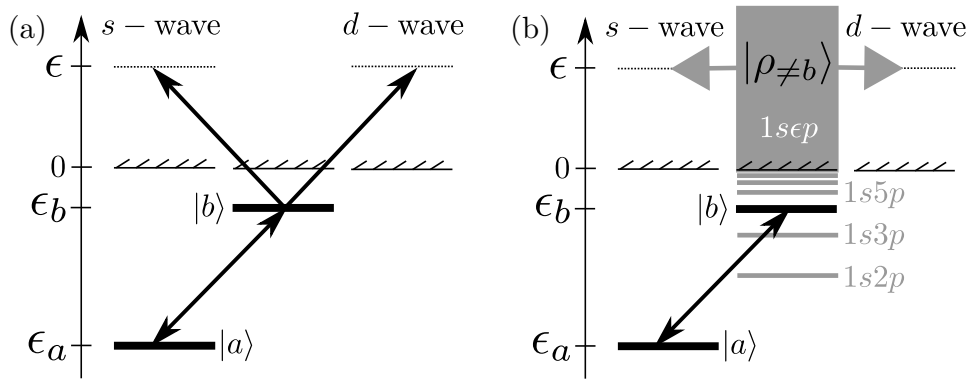

Figure 29: Photoionization from (a) the excited $1s4p$ state by a one-photon resonant process, or (b) via all states other than $1s4p$ by a non-resonant two-photon process. Figure modified from Paper IV.

In Paper IV, the pulse length of 56 fs FWHM compares to the Rabi period of $2\pi/\Omega = 52$ fs at resonance. The experiment is therefore performed in the regime of 1 – 1.5 Rabi periods,

depending on the exact pulse shape[20]. If the electron is ejected after one full Rabi period, but before one and a half Rabi periods, one could distinguish between electrons ejected from the ground state and the excited state by the number of peaks in the photoelectron spectrum. The electrons ejected from the ground state would then have completed a full cycle and have acquired a π phase shift before being ejected, whereas electrons ejected from the excited state would only have completed half a Rabi period since the excited state is first populated after half a Rabi period. The electrons that are ejected from the ground state will therefore interfere destructively, leading to an AT doublet, while the electrons ejected from the excited state will only show a single peak.

Another way to distinguish the photoelectrons stemming from the ground state from those stemming from the excited state is to study the asymmetry of the AT doublet. From Eq. (1.16) it is seen that only the ground-state amplitude has an antisymmetric frequency component that depends on detuning. In Fig. 30a,c we show photoelectron spectra with pulse parameters as in Paper IV and a smooth-flat-top envelope, together with the ground-state population in Fig. 30b,d, for both the initial condition that the population is in the ground state (the top row), and that the population is in the excited state (the bottom row). The three lines correspond to three values of detuning from the photon energy that results in symmetric AT peaks, $\omega = \omega_{\mathrm{sym}} + \Delta\omega$: black, $\hbar\Delta\omega = -0.13\,\mathrm{eV}$; orange, $\hbar\Delta\omega = 0$; sky blue, $\hbar\Delta\omega = 0.13\,\mathrm{eV}$. The asymmetry of the two AT peak with detuning in Fig. 30a indicates that the photoelectrons are ejected, at least partly, from the ground state. For the field strength used in the experiment, we estimated the ionization probability ratio between the one-photon resonant ionization process and the two-photon non-resonant process to be roughly $10^4 : 1$ in favour of the one-photon resonant process. However, the dipole matrix elements from the set of complement states to the continuum are stronger than the dipole matrix element from $1s4p$ to the continuum by a factor of 10^4 in favour of the non-resonant pathway. This means that the two processes happen with comparable strength. The two ionization processes interfere such that the kinetic energy where one finds the symmetric AT peaks is blue shifted. For the other initial condition that the excited state is populated, shown in Fig. 30c,d, there is no sign of an AT peak. The ground-state population however modulates in a similar fashion.

We further note that when the frequency is increased, the contrast of the peak increases in Fig. 30a. A possible explanation to this may be that the population ejected from the excited state has not had time to develop an AT peak, and the combined signal from the ground state and the excited state may then result in a lack of contrast. In Fig. 30b, the ground-state population is shown for three mentioned cases. It is seen that the chosen pulse parameters give Rabi modulation of close to 1.5 periods, with the red-detuned case below 1.5 periods. However, the loss of contrast may partly be explained by macroscopic volume

[20] A Gaussian pulse with FWHM equal to the width of a flat-top pulse will result in 1.5 times more Rabi periods, see the area theorem in Ref. [127].

average effects of the stretched beam focus.

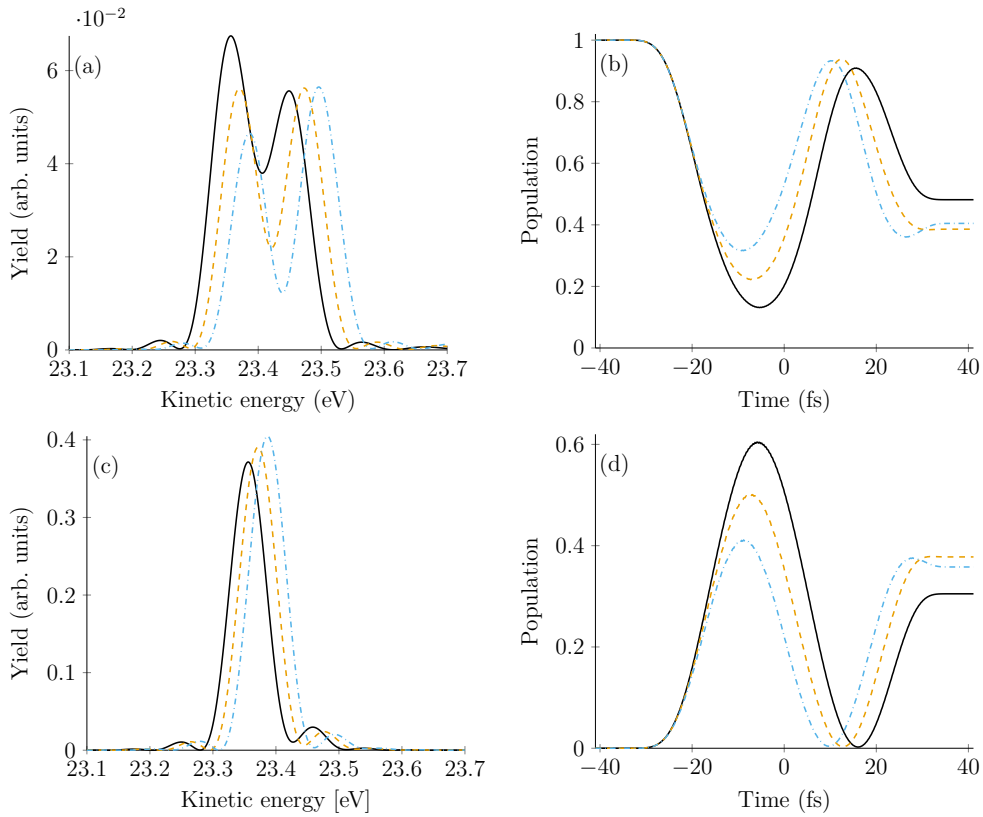

Figure 30: Left column: Photoelectron spectra centered about the frequency of symmetric AT peaks, ω_{sym} (orange), and asymmetric AT peaks obtained with a detuning of $\hbar\Delta\omega = -13\,\mathrm{eV}$ (black), and $\hbar\Delta\omega = +13\,\mathrm{eV}$ (sky blue). Right column: Ground state population as a function of time. In (a) and (b), the population is initially in the ground state, whereas in (c) and (d) the population is initially in the excited state.

Photoelectron angular distribution

There is a strong angular dependence on to the scaling of the dipole matrix elements. The $10^4 : 1$ scaling in favour to the two-photon process holds for transitions to the d continuum, while to the s continuum, there is only a factor $10^2 : 1$ in favour of the two-photon process. This renders the one-photon process stronger when measuring s-partial waves, and there is therefore a strong angular dependence. In Fig. 31 we show a photoelectron spectra measured (a) along the polarization axis and (b) perpendicular to the polarization axis using the frequency of symmetric AT peaks, $\omega = \omega_{\mathrm{sym}}$, and detuning $\hbar\Delta\omega = -13\,\mathrm{eV}$ and $\hbar\Delta\omega = +13\,\mathrm{eV}$, respectively. The clear minimum at the frequency of symmetric peaks ω_{sym} for the spectrum measured along the polarization axis indicates that more of

the signal stems from the ground state than in the spectrum measured perpendicular to the polarization axis. The change in the ground state–excited state emission mixture is further seen from the shift of the symmetric-peak frequency, where in the spectrum measured perpendicular to the polarization axis, the blue detuning required for symmetric peaks is smaller.

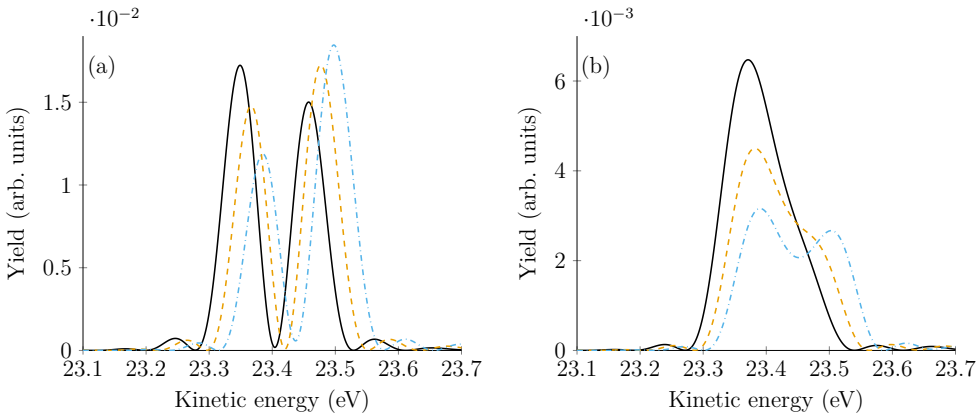

Figure 31: Angle-resolved photoelectron spectra along (a) the polarization axis, and (b) at $\theta = 90$ degrees from the polarization axis, obtained with fields of frequency centered about the frequency of symmetric AT peaks, ω_{sym} (orange), and with a detuning of $\hbar\Delta\omega = -13\,\mathrm{eV}$ (black) and $\hbar\Delta\omega = +13\,\mathrm{eV}$ (sky blue).

11 Summary and outlook

In this thesis we have applied the TDCIS method to study photoionization in noble gas atoms that are subject to different types of XUV and IR light sources commonly used in attosecond and free-electron laser sciences. The work has consisted of three prominent parts with almost uniform distribution of time on these: implementation and validation of surface-flux methods, development of the TRK correction to velocity gauge TDCIS, and application to experiments.

Information on the photoionization process is extracted by studying the photoelectron spectrum, which we retrieve using the surface-flux methods tSURFF and iSURFF that we have implemented in this thesis. The retrieved photoelectron spectra are fully differential, which means that all relevant quantum numbers are revealed. The photoelectron spectra can thus provide insight in a range of experiments. While we have focused on fundamental processes in a selection of novel interferometric single-ionization experiments made in noble gas atoms, attosecond and free-electron laser sciences have progressed along many parallell tracks. The implemented surface-flux methods can in future works be applied to matter described within frameworks other than TDCIS, to study for instance photodetachment in molecules or pump–probe experiments in solids.

The majority of the results we present is retrieved using TDCIS implemented in the velocity gauge. While the convergence properties of velocity gauge is enticing, the size-inconsistency problem due to the truncation of the configuration space hampers its use in experiments with strong low-frequency fields. This is further the regime where convergence of the length gauge can be problematic, due to the large number of angular momenta required. This led us to develop a correction based on the TRK sum rule, which mediates the application to strong-field experiments, and therefore opens the possibility to use velocity gauge in the strong-field regime. However, the TRK correction is perturbative in the vector potential and is expected to fail at very strong fields. It would therefore be of interest to further improve the correction to higher order (maybe infinite) in the vector potential to unlock the most extreme regimes of attosecond science. Moreover, one could also be inspired to use a similar technique of corrections based on effective potentials in other problems to e.g. include effects of double ionization.

Our theoretical and numerical development have been done in close collaboration with experimental groups, both the attosecond group in Lund and in a larger collaboration in Paper IV. The close connection to experiments has been directly beneficial to the theoretical development and validation of the implementation. Finally, there are predictions in this thesis that would be interesting to confirm with experiments in the future. For instance, the angular distributions in higher-order sidebands in helium and neon that we predicted in Paper I and the laser-assisted dynamical interference effect that we predicted in Paper VI.

Appendices

A Matrix elements in tSURFF

The tSURFF equations in Sec. 6.4 are derived in the formalism of second quantization, and here we show explicitly how these terms are derived.

A.1 Wick's theorem and notation

We evaluate the sequence of creation and annihilation operators using Wick's theorem, using a notation slightly modified from that of Ref. [26]. A *contraction* is defined as the difference between the ordinary product and the normal product of two arbitrary operators, $\hat{x}$ and $\hat{z}$. Since only contraction of holes with holes and particles with particles yields any contribution, we distinguish the notation between them. We denote contraction of hole operators $\hat{a}, \hat{b}, \hat{c}, \ldots$ with lines above and contraction of particle operators $\hat{p}, \hat{q}, \hat{r}, \ldots$ with lines below,

$$\overset{\square}{\hat{a}}\hat{c} = \hat{a}\hat{c} - \{\hat{a}\hat{c}\}, \tag{A.1a}$$

$$\hat{p}\underset{\square}{\hat{q}} = \hat{p}\hat{q} - \{\hat{p}\hat{q}\}. \tag{A.1b}$$

An arbitrary product $\hat{I} = \hat{i}\hat{j}\hat{k}\ldots$ of operators written on normal form $\{\hat{I}\}$ gives zero when acting on the reference vacuum,

$$\{\hat{I}\}|\Phi_0\rangle = 0. \tag{A.2}$$

Wick's theorem [128] can be expressed as

$$\hat{I} = \{\hat{I}\} + \{\overset{\square}{\underset{\square}{\hat{I}}}\}, \tag{A.3}$$

where $\{\overset{\square}{\underset{\square}{\hat{I}}}\}$ represents all possible single, double, triple, ..., contractions within $\hat{I}$ and a subsequent rearrangement of the remaining operators to normal form.

When we evaluate operator products, we will use Wick's theorem to exchange the operator product for contractions and normal forms. In the end we are only interested in the *fully* contracted terms, and introduce a new notation that corresponds to this. The notation signifies that the left- and the right-hand sides are equal upon action on the vacuum,

$$\hat{I} = \{\hat{I}\} + \{\overset{\square}{\underset{\square}{\hat{I}}}\} \overset{\circ}{=} \boxed{\hat{I}}. \tag{A.4}$$

where $\boxed{\hat{I}}$ represents the sum of fully contracted products in $\hat{I}$. Consider the two following examples of operator products:

$$\hat{a}_b^\dagger \hat{a}_a = \{\hat{a}_b^\dagger \hat{a}_a\} + \{\overset{\square}{\hat{a}_b^\dagger}\hat{a}_a\} = -\hat{a}_a \hat{a}_b^\dagger \delta_{ab} \overset{\circ}{=} \delta_{ab}. \tag{A.5}$$

and

$$\begin{aligned}\hat{a}_a^\dagger \hat{a}_p \hat{a}_q^\dagger \hat{a}_b &= \{\hat{a}_a^\dagger \hat{a}_p \hat{a}_q^\dagger \hat{a}_b\} + \{\hat{a}_a^\dagger \hat{a}_p \hat{a}_q^\dagger \hat{a}_b\} + \{\hat{a}_a^\dagger \hat{a}_p \hat{a}_q^\dagger \hat{a}_b\} + \{\hat{a}_a^\dagger \hat{a}_p \hat{a}_q^\dagger \hat{a}_b\} \\ &= \hat{a}_q^\dagger \hat{a}_b \hat{a}_a^\dagger \hat{a}_p - \delta_{ab} \hat{a}_q^\dagger \hat{a}_p - \delta_{pq} \hat{a}_b \hat{a}_a^\dagger + \delta_{ab}\delta_{pq} \overset{\circ}{=} \delta_{ab}\delta_{pq},\end{aligned} \tag{A.6}$$

The normal forms $\hat{a}_a \hat{a}_b^\dagger$ and $\hat{a}_q^\dagger \hat{a}_p$ give zero, and only the terms which are fully contracted are left.

A.2 Matrix elements of the TDCIS Hamiltonian

In this section, we evaluate the matrix element $\langle \chi_{\mathbf{k},a} | \hat{\Theta} \hat{H} | \Psi \rangle$ in detail for each part of the TDCIS Hamiltonian in Eq. (5.7). Since the expressions are lengthy, we occasionally refer to parts of the expressions by the subnumbering of the particular expression. For example, Eq. (A.7a) refers to only the first term on the right-hand side of Eq. (A.7), not including the left-hand side.

Matrix element of the mean-field Hamiltonian

The matrix element with the mean-field Hamiltonian $\hat{H}_0^{(\mathrm{HF})}$ is given by a zero-particle term and two one-particle terms,

$$\langle \chi_{\mathbf{k},a} | \hat{\Theta} \hat{H}_0^{(\mathrm{HF})} | \Psi \rangle = \sum_{p,c,rs,bq} \varepsilon_c \langle r|\hat{\theta}|s\rangle \langle \Phi_0 | \hat{a}_a^\dagger \hat{a}_p \hat{a}_r^\dagger \hat{a}_s \hat{a}_q^\dagger \hat{a}_b | \Phi_0 \rangle \langle \mathbf{k}|p\rangle \mathrm{e}^{\mathrm{i}\mathcal{S}_a(\mathbf{k},t)} \alpha_b^q(t) \tag{A.7a}$$

$$+ \sum_{p,tu,rs,bq} \langle r|\hat{\theta}|s\rangle \langle t|\hat{h}^{(\mathrm{HF})}|u\rangle \langle \Phi_0 | \hat{a}_a^\dagger \hat{a}_p \hat{a}_r^\dagger \hat{a}_s \hat{a}_t^\dagger \hat{a}_u \hat{a}_q^\dagger \hat{a}_b | \Phi_0 \rangle \times \langle \mathbf{k}|p\rangle \mathrm{e}^{\mathrm{i}\mathcal{S}_a(\mathbf{k},t)} \alpha_b^q(t) \tag{A.7b}$$

$$- \sum_{p,cd,rs,bq} \langle r|\hat{\theta}|s\rangle \langle c|\hat{h}^{(\mathrm{HF})}|d\rangle \langle \Phi_0 | \hat{a}_a^\dagger \hat{a}_p \hat{a}_r^\dagger \hat{a}_s \hat{a}_d \hat{a}_c^\dagger \hat{a}_q^\dagger \hat{a}_b | \Phi_0 \rangle \times \langle \mathbf{k}|p\rangle \mathrm{e}^{\mathrm{i}\mathcal{S}_a(\mathbf{k},t)} \alpha_b^q(t). \tag{A.7c}$$

For these three terms, we simplify the operator products using Wick's theorem

$$\hat{a}_a^\dagger \hat{a}_p \hat{a}_r^\dagger \hat{a}_s \hat{a}_q^\dagger \hat{a}_b \stackrel{\circ}{=} \hat{a}_a^\dagger \hat{a}_p \hat{a}_r^\dagger \hat{a}_s \hat{a}_q^\dagger \hat{a}_b = \delta_{ab}\delta_{pr}\delta_{qs}, \tag{A.8a}$$

$$\begin{aligned} \hat{a}_a^\dagger \hat{a}_p \hat{a}_r^\dagger \hat{a}_s \hat{a}_t^\dagger \hat{a}_u \hat{a}_q^\dagger \hat{a}_b &\stackrel{\circ}{=} \left(\hat{a}_a^\dagger \hat{a}_p \hat{a}_r^\dagger\right) \hat{a}_s \hat{a}_t^\dagger \left(\hat{a}_u \hat{a}_q^\dagger \hat{a}_b\right) \\ &\stackrel{\circ}{=} \delta_{pr}\delta_{qu} \left(\hat{a}_a^\dagger \hat{a}_s \hat{a}_t^\dagger \hat{a}_b\right) = \delta_{pr}\delta_{qu}\delta_{ab}\delta_{st}, \end{aligned} \tag{A.8b}$$

$$\begin{aligned} \hat{a}_a^\dagger \hat{a}_p \hat{a}_r^\dagger \hat{a}_s \hat{a}_d \hat{a}_c^\dagger \hat{a}_q^\dagger \hat{a}_b &\stackrel{\circ}{=} \left(\hat{a}_a^\dagger \hat{a}_p \hat{a}_r^\dagger\right) \hat{a}_s \hat{a}_d \left(\hat{a}_c^\dagger \hat{a}_q^\dagger \hat{a}_b\right) \\ &\stackrel{\circ}{=} -\delta_{pr}\delta_{bc}(\hat{a}_a^\dagger \hat{a}_s \hat{a}_d \hat{a}_q^\dagger) = \delta_{pr}\delta_{bc}\delta_{ad}\delta_{qs}, \end{aligned} \tag{A.8c}$$

which simplify the three terms in Eq. (A.7) to

$$(\text{A.7a}) = \sum_{c,pq} \varepsilon_c \langle \mathbf{k}|p\rangle\langle p|\hat{\theta}|q\rangle \mathrm{e}^{\mathrm{i}\mathcal{S}_a(\mathbf{k},t)} \alpha_a^q(t) = \sum_{c,q} \varepsilon_c \langle \mathbf{k}|\hat{\theta}|q\rangle \mathrm{e}^{\mathrm{i}\mathcal{S}_a(\mathbf{k},t)} \alpha_a^q(t), \tag{A.9a}$$

$$(\text{A.7b}) = \sum_{tqp} \langle \mathbf{k}|p\rangle\langle p|\hat{\theta}|t\rangle\langle t|\hat{h}^{(\mathrm{HF})}|q\rangle \mathrm{e}^{\mathrm{i}\mathcal{S}_a(\mathbf{k},t)} \alpha_a^q(t) = \sum_{q} \langle \mathbf{k}|\hat{\theta}\hat{h}^{(\mathrm{HF})}|q\rangle \mathrm{e}^{\mathrm{i}\mathcal{S}_a(\mathbf{k},t)} \alpha_a^q(t), \tag{A.9b}$$

$$(\text{A.7c}) = -\sum_{b,pq} \langle \mathbf{k}|p\rangle\langle p|\hat{\theta}|q\rangle\langle b|\hat{h}^{(\mathrm{HF})}|a\rangle \mathrm{e}^{\mathrm{i}\mathcal{S}_a(\mathbf{k},t)} \alpha_b^q(t) = -\sum_{q} \varepsilon_a \langle \mathbf{k}|\hat{\theta}|q\rangle \mathrm{e}^{\mathrm{i}\mathcal{S}_a(\mathbf{k},t)} \alpha_a^q(t). \tag{A.9c}$$

In total, we have for the mean-field Hamiltonian,

$$\langle \chi_{\mathbf{k},a}|\hat{\Theta}\hat{H}_0^{(\mathrm{HF})}|\Psi\rangle = \sum_q \left[\langle \mathbf{k}|\hat{\theta}\hat{h}^{(\mathrm{HF})}|q\rangle + \left(\sum_c \varepsilon_c - \varepsilon_a\right)\langle \mathbf{k}|\hat{\theta}|q\rangle\right] \mathrm{e}^{\mathrm{i}\mathcal{S}_a(\mathbf{k},t)} \alpha_a^q(t). \tag{A.10}$$

Matrix element of the zero-body potential

The matrix element with the zero-body potential $\hat{V}_0$ is evaluated similarly to the term in Eq. (A.7a) to

$$\begin{aligned} \langle \chi_{\mathbf{k},a}|\hat{\Theta}\hat{V}_0|\Psi\rangle &= -\frac{1}{2}\sum_{p,c,rs,bq} \langle c|u^{(\mathrm{HF})}|c\rangle\langle r|\hat{\theta}|s\rangle\langle \Phi_0|\hat{a}_a^\dagger \hat{a}_p \hat{a}_r^\dagger \hat{a}_s \hat{a}_q^\dagger \hat{a}_b|\Phi_0\rangle\langle \mathbf{k}|p\rangle \mathrm{e}^{\mathrm{i}\mathcal{S}_a(\mathbf{k},t)} \alpha_b^q(t) \\ &= E_1^{(\mathrm{HF})} \sum_q \langle \mathbf{k}|\hat{\theta}|q\rangle \mathrm{e}^{\mathrm{i}\mathcal{S}_a(\mathbf{k},t)} \alpha_a^q(t). \end{aligned} \tag{A.11}$$

Matrix element of the one-body interaction potential

Further, the matrix element involving the one-body field-interaction operator is given by

$$\langle \chi_{\mathbf{k},a}|\hat{\Theta}\hat{V}_1^{(\mathrm{int})}|\Psi\rangle = \sum_{p,tu,rs,bq} \langle r|\hat{\theta}|s\rangle\langle t|\hat{v}_1^{(\mathrm{int})}|u\rangle\langle\Phi_0|\hat{a}_a^\dagger\hat{a}_p\hat{a}_r^\dagger\hat{a}_s\hat{a}_t^\dagger\hat{a}_u\hat{a}_q^\dagger\hat{a}_b|\Phi_0\rangle\langle\mathbf{k}|p\rangle \mathrm{e}^{\mathrm{i}\mathcal{S}_a(\mathbf{k},t)}\alpha_b^q(t) \tag{A.12a}$$

$$- \sum_{p,cd,rs,bq} \langle r|\hat{\theta}|s\rangle\langle c|\hat{v}_1^{(\mathrm{int})}|d\rangle\langle\Phi_0|\hat{a}_a^\dagger\hat{a}_p\hat{a}_r^\dagger\hat{a}_s\hat{a}_d\hat{a}_c^\dagger\hat{a}_q^\dagger\hat{a}_b|\Phi_0\rangle\langle\mathbf{k}|p\rangle \mathrm{e}^{\mathrm{i}\mathcal{S}_a(\mathbf{k},t)}\alpha_b^q(t). \tag{A.12b}$$

The two hole–particle cross terms, e.g. $\langle t|\hat{v}_1^{(\mathrm{int})}|c\rangle$ do not contribute since they lead to an unbalanced number of hole- and particle operators. For instance, the operator product corresponding to $\langle t|\hat{v}_1^{(\mathrm{int})}|c\rangle$ gives

$$\begin{aligned}\hat{a}_a^\dagger\hat{a}_i\hat{a}_r^\dagger\hat{a}_s\left(\hat{a}_c^\dagger\hat{a}_t\hat{a}_q^\dagger\hat{a}_b\right) &\overset{\circ}{=} \delta_{bc}\delta_{qt}\left(\hat{a}_a^\dagger\hat{a}_d\hat{a}_r^\dagger\hat{a}_s + \hat{a}_a^\dagger\hat{a}_p\hat{a}_r^\dagger\hat{a}_s\right)\\ &\overset{\circ}{=} \delta_{bc}\delta_{qt}\left(\delta_{ad}\{\hat{a}_r^\dagger\hat{a}_s\} + \delta_{ur}\{\hat{a}_a^\dagger\hat{a}_s\}\right) \overset{\circ}{=} 0.\end{aligned} \tag{A.13}$$

We have emphasized the unbalanced set of operators in Eq. (A.13) by expanding the plane wave on also the core orbitals, and not only the virtual orbitals by writing the plane wave set of operators as $\hat{a}_a^\dagger\hat{a}_i$, instead of $\hat{a}_a^\dagger\hat{a}_p$. The operator products corresponding to Eq. (A.12a)–(A.12b) are evaluated using Eq. (A.8b)–(A.8c). We get

$$\text{(A.12a)} = \sum_{tqp}\langle\mathbf{k}|p\rangle\langle p|\hat{\theta}|t\rangle\langle t|\hat{v}_1^{(\mathrm{int})}|q\rangle \mathrm{e}^{\mathrm{i}\mathcal{S}_a(\mathbf{k},t)}\alpha_a^q(t) = \sum_q\langle\mathbf{k}|\hat{\theta}\hat{v}_1^{(\mathrm{int})}|q\rangle \mathrm{e}^{\mathrm{i}\mathcal{S}_a(\mathbf{k},t)}\alpha_a^q(t), \tag{A.14a}$$

$$\text{(A.12b)} = -\sum_{b,pq}\langle\mathbf{k}|p\rangle\langle p|\hat{\theta}|q\rangle\langle b|\hat{v}_1^{(\mathrm{int})}|a\rangle \mathrm{e}^{\mathrm{i}\mathcal{S}_a(\mathbf{k},t)}\alpha_b^q(t) = -\sum_{b,q}\langle\mathbf{k}|\hat{\theta}|q\rangle\langle b|\hat{v}_1^{(\mathrm{int})}|a\rangle \mathrm{e}^{\mathrm{i}\mathcal{S}_a(\mathbf{k},t)}\alpha_b^q(t), \tag{A.14b}$$

which in total gives us

$$\langle \chi_{\mathbf{k},a}|\hat{\Theta}\hat{V}_1^{(\mathrm{int})}|\Psi\rangle = \sum_q\left(\langle\mathbf{k}|\hat{\theta}\hat{v}_1^{(\mathrm{int})}|q\rangle\alpha_a^q(t) - \sum_b\langle\mathbf{k}|\hat{\theta}|q\rangle\langle b|\hat{v}_1^{(\mathrm{int})}|a\rangle\alpha_b^q(t)\right)\mathrm{e}^{\mathrm{i}\mathcal{S}_a(\mathbf{k},t)}. \tag{A.15}$$

Matrix element of the two-body potential

The matrix element for the two-body potential is given by the operator product between the one-body Heaviside operator and the two-body Coulomb potential operator, which

evaluates to

$$\begin{aligned}\langle\chi_{\mathbf{k},a}|\hat{\Theta}\hat{V}_2|\Psi\rangle = \frac{1}{2}\sum_{p,rs,ijkl,bq} &\langle r|\hat{\theta}|s\rangle\langle ij|r_{12}^{-1}|kl\rangle \\ &\langle\Phi_0|\hat{a}_a^\dagger\hat{a}_p\hat{a}_r^\dagger\hat{a}_s\{\hat{a}_i^\dagger\hat{a}_j^\dagger\hat{a}_l\hat{a}_k\}\hat{a}_q^\dagger\hat{a}_b|\Phi_0\rangle \\ &\langle\mathbf{k}|p\rangle\mathrm{e}^{\mathrm{i}\mathcal{S}_a(\mathbf{k},t)}\alpha_b^q(t).\end{aligned} \tag{A.16}$$

Four cases of $\{\hat{a}_i^\dagger\hat{a}_j^\dagger\hat{a}_l\hat{a}_k\}$, corresponding to two direct Coulomb interactions, and two exchange Coulomb interactions will give contributions. These elements have the operator product

$$\begin{aligned}\hat{a}_a^\dagger\hat{a}_p\hat{a}_r^\dagger\hat{a}_s\{\hat{a}_c^\dagger\hat{a}_t^\dagger\hat{a}_d\hat{a}_u\}\hat{a}_q^\dagger\hat{a}_b &\overset{\circ}{=} \left(\hat{a}_a^\dagger\hat{a}_p\hat{a}_r^\dagger\right)\hat{a}_s\hat{a}_t^\dagger\hat{a}_d\left(\hat{a}_c^\dagger\hat{a}_u\hat{a}_q^\dagger\hat{a}_b\right) \\ &\overset{\circ}{=} \delta_{pr}\delta_{qu}\delta_{bc}\left(\hat{a}_a^\dagger\hat{a}_s\hat{a}_t^\dagger\hat{a}_d\right) \overset{\circ}{=} \delta_{pr}\delta_{qu}\delta_{bc}\delta_{st}\delta_{ad}, \qquad \text{(A.17a)} \\ \hat{a}_a^\dagger\hat{a}_p\hat{a}_r^\dagger\hat{a}_s\{\hat{a}_c^\dagger\hat{a}_t^\dagger\hat{a}_u\hat{a}_d\}\hat{a}_q^\dagger\hat{a}_b &\overset{\circ}{=} -\delta_{pr}\delta_{qu}\delta_{bc}\delta_{st}\delta_{ad}, \qquad \text{(A.17b)}\end{aligned}$$

which yields

$$\begin{aligned}\langle\chi_{\mathbf{k},a}|\hat{\Theta}\hat{V}_2|\Psi\rangle &= \sum_{b,pqt}\langle\mathbf{k}|p\rangle\langle p|\hat{\theta}|t\rangle\left(\langle bt|r_{12}^{-1}|qa\rangle - \langle bt|r_{12}^{-1}|aq\rangle\right)\mathrm{e}^{\mathrm{i}\mathcal{S}_a(\mathbf{k},t)}\alpha_b^q(t) \\ &= \sum_{b,qt}\langle\mathbf{k}|\hat{\theta}|t\rangle\left(\langle bt|r_{12}^{-1}|qa\rangle - \langle bt|r_{12}^{-1}|aq\rangle\right)\mathrm{e}^{\mathrm{i}\mathcal{S}_a(\mathbf{k},t)}\alpha_b^q(t).\end{aligned} \tag{A.18}$$

Matrix element of the HF shift

Finally, for the energy shift $E^{(\mathrm{HF})}$ we use the result of Eq. (A.7a)–(A.8a), since it is a zero-body operator, to obtain

$$\langle\chi_{\mathbf{k},a}|\hat{\Theta}E^{(\mathrm{HF})}|\Psi\rangle = E^{(\mathrm{HF})}\sum_q\langle\mathbf{k}|\hat{\theta}|q\rangle\mathrm{e}^{\mathrm{i}\mathcal{S}_a(\mathbf{k},t)}\alpha_a^q(t). \tag{A.19}$$

Final expression of the matrix element of the TDCIS Hamiltonian

In total, the matrix element for the second term in Eq. (6.40) is evaluated to

$$\begin{aligned}\langle\chi_{\mathbf{k},a}|\hat{\Theta}(r_c)\hat{H}|\Psi\rangle = \sum_q \Bigg\{ &\left[\langle\mathbf{k}|\hat{\theta}\hat{h}^{(\mathrm{HF})}|q\rangle + \left(\sum_c \varepsilon_c - \varepsilon_a + E_1^{(\mathrm{HF})}\right)\langle\mathbf{k}|\hat{\theta}|q\rangle\right]\alpha_a^q(t) \\ &+ \sum_{b,t}\langle\mathbf{k}|\hat{\theta}|t\rangle(\langle bt|r_{12}^{-1}|qa\rangle - \langle bt|r_{12}^{-1}|aq\rangle)\alpha_b^q(t) - E^{(\mathrm{HF})}\langle\mathbf{k}|\hat{\theta}|q\rangle\alpha_a^q(t) \\ &+ \langle\mathbf{k}|\hat{\theta}\hat{v}_1^{(\mathrm{int})}|q\rangle\alpha_a^q(t) - \sum_b\langle\mathbf{k}|\hat{\theta}|q\rangle\langle b|\hat{v}_1^{(\mathrm{int})}|a\rangle\alpha_b^q(t)\Bigg\}\mathrm{e}^{\mathrm{i}\mathcal{S}_a(\mathbf{k},t)},\end{aligned} \tag{A.20}$$

which simplifies to

$$\begin{aligned}\langle\chi_{\mathbf{k},a}|\hat{\Theta}(r_c)\hat{H}|\Psi\rangle = \sum_q \Bigg[&\left(\langle\mathbf{k}|\hat{\theta}\hat{h}^{(\mathrm{HF})}|q\rangle - \varepsilon_a\langle\mathbf{k}|\hat{\theta}|q\rangle\right)\alpha_a^q(t) \\ &+ \sum_{b,t}\langle\mathbf{k}|\hat{\theta}|t\rangle\left(\langle bt|r_{12}^{-1}|qa\rangle - \langle bt|r_{12}^{-1}|aq\rangle\right)\alpha_b^q(t) \\ &+ \langle\mathbf{k}|\hat{\theta}\hat{v}_1^{(\mathrm{int})}|q\rangle\alpha_a^q(t) - \sum_b\langle\mathbf{k}|\hat{\theta}|q\rangle\langle b|\hat{v}_1^{(\mathrm{int})}|a\rangle\alpha_b^q(t)\Bigg]\mathrm{e}^{\mathrm{i}\mathcal{S}_a(\mathbf{k},t)}.\end{aligned} \tag{A.21}$$

For a large r_c, the matrix element of the one-body HF Hamiltonian tends to the kinetic term only, and the matrix elements of the two-body Coulomb potential tends to zero, and we may thus approximate Eq. (A.21) as

$$\begin{aligned}\langle\chi_{\mathbf{k},a}|\hat{\Theta}(r_c)\hat{H}|\Psi\rangle \approx \sum_q \Bigg[&\left(\langle\mathbf{k}|\hat{\theta}\hat{t}|q\rangle - \varepsilon_a\langle\mathbf{k}|\hat{\theta}|q\rangle + \langle\mathbf{k}|\hat{\theta}\hat{v}_1^{(\mathrm{int})}|q\rangle\right)\alpha_a^q(t) \\ &- \sum_b\langle\mathbf{k}|\hat{\theta}|q\rangle\langle b|\hat{v}_1^{(\mathrm{int})}|a\rangle\alpha_b^q(t)\Bigg]\mathrm{e}^{\mathrm{i}\mathcal{S}_a(\mathbf{k},t)}.\end{aligned} \tag{A.22}$$

A.3 Matrix elements of the Volkov Hamiltonian

We here work out the matrix elements of the two parts of the adjusted Volkov Hamiltonian in Eq. (6.17). The kinetic part is given by

$$\begin{aligned}\langle\chi_{\mathbf{k},a}|\hat{T}\hat{\Theta}|\Psi\rangle &= \sum_{p,tu,rs,qb}\langle t|\hat{t}|u\rangle\langle r|\hat{\theta}|s\rangle\langle\Phi_0|\hat{a}_a^\dagger\hat{a}_p\hat{a}_t^\dagger\hat{a}_u\hat{a}_r^\dagger\hat{a}_s\hat{a}_q^\dagger\hat{a}_b|\Phi_0\rangle\alpha_b^q(t)\mathrm{e}^{\mathrm{i}\mathcal{S}_a(\mathbf{k},t)}\langle\mathbf{k}|p\rangle \\ &= \sum_q\langle\mathbf{k}|\hat{t}\hat{\theta}|q\rangle\mathrm{e}^{\mathrm{i}\mathcal{S}_a(\mathbf{k},t)}\alpha_a^q(t),\end{aligned} \tag{A.23}$$

where we have used that the operator product evaluates to

$$\hat{a}_a^\dagger\hat{a}_p\hat{a}_t^\dagger\hat{a}_u\hat{a}_r^\dagger\hat{a}_s\hat{a}_q^\dagger\hat{a}_b \overset{\circ}{=} \delta_{ab}\delta_{pt}\delta_{ur}\delta_{qs}, \tag{A.24}$$

and the field part is given by

$$\begin{aligned}\langle\chi_{\mathbf{k},a}|\hat{V}_1^{(\mathrm{int})}\hat{\Theta}|\Psi\rangle &= \sum_{p,tu,rs,qb}\langle t|\hat{v}_1^{(\mathrm{int})}|u\rangle\langle r|\hat{\theta}|s\rangle\langle\Phi_0|\hat{a}_a^\dagger\hat{a}_p\hat{a}_t^\dagger\hat{a}_u\hat{a}_r^\dagger\hat{a}_s\hat{a}_q^\dagger\hat{a}_b|\Phi_0\rangle\alpha_b^q(t)\mathrm{e}^{\mathrm{i}\mathcal{S}_a(\mathbf{k},t)}\langle\mathbf{k}|p\rangle \\ &= \sum_q\langle\mathbf{k}|\hat{t}\hat{\theta}|q\rangle\mathrm{e}^{\mathrm{i}\mathcal{S}_a(\mathbf{k},t)}\alpha_a^q(t).\end{aligned} \tag{A.25}$$

In total, we arrive at

$$\langle\chi_{\mathbf{k},a}|\hat{H}_a^{(\mathrm{V})}\hat{\Theta}|\Psi\rangle = \sum_q\left(\langle\mathbf{k}|\hat{t}\hat{\theta}|q\rangle + \langle\mathbf{k}|\hat{v}_1^{(\mathrm{int})}\hat{\theta}|q\rangle - \varepsilon_a\langle\mathbf{k}|\hat{\theta}|q\rangle\right)\mathrm{e}^{\mathrm{i}\mathcal{S}_a(\mathbf{k},t)}\alpha_a^q(t). \tag{A.26}$$

References

[1] C. Cohen-Tannoudji, J. Dupont-Rock, and G. Grynberg, *Atom–Photon Interactions* (Wiley, 2004).

[2] A. F. Starace, "Theory of atomic photoionization", in *Encyclopedia of physics / handbuch der physik* (Springer Berlin Heidelberg, 1982), pp. 1–121.

[3] H. Bethe and E. Salpeter, *Quantum mechanics of one- and two-electron atoms* (Plenum Pub. Corp., 1977).

[4] G. S. Voronov and N. B. Delone, "Many-photon ionization of the xenon atom by ruby laser radiation", Journal of Experimental and Theoretical Physics (1966).

[5] P. Agostini, G. Barjot, J. Bonnal, G. Mainfray, C. Manus, and J. Morellec, "Multiphoton ionization of hydrogen and rare gases", IEEE Journal of Quantum Electronics **4**, 667–669 (1968).

[6] G. Mainfray and G. Manus, "Multiphoton ionization of atoms", Rep. Prog. Phys. **54**, 1333 (1991).

[7] P. Agostini, F. Fabre, G. Mainfray, G. Petite, and N. K. Rahman, "Free-Free Transitions Following Six-Photon Ionization of Xenon Atoms", Phys. Rev. Lett. **42**, 1127–1130 (1979).

[8] Y. Gontier, M. Poirier, and M. Trahin, "Multiphoton absorptions above the ionisation threshold", J. Phys. B: Atom. Mol. Phys. **13**, 1381 (1980).

[9] A. Permogorov, G. Cantono, D. Guenot, A. Persson, and C.-G. Wahlström, "Effects of pulse chirp on laser-driven proton acceleration", Sci Rep **12**, 3031 (2022).

[10] D. Strickland and G. Mourou, "Compression of amplified chirped optical pulses", Optics Communications **56**, 219–221 (1985).

[11] K. Yamanouchi, W. T. Hill III, and G. G. Paulus, eds., *Progress in ultrafast intense laser science XIII*, 1st ed., Springer Series in Chemical Physics (Springer International Publishing, Basel, Switzerland, Jan. 2018).

[12] E. A. Seddon et al., "Short-wavelength free-electron laser sources and science: a review", Rep. Prog. Phys. **80**, 115901 (2017).

[13] E. Allaria et al., "Highly coherent and stable pulses from the FERMI seeded free-electron laser in the extreme ultraviolet", Nature Photon **6**, 699–704 (2012).

[14] V. Ayvazyan et al., "First operation of a free-electron laser generating GW power radiation at 32 nm wavelength", Eur. Phys. J. D **37**, 297–303 (2006).

[15] A. A. Sorokin, S. V. Bobashev, T. Feigl, K. Tiedtke, H. Wabnitz, and M. Richter, "Photoelectric Effect at Ultrahigh Intensities", Phys. Rev. Lett. **99**, 213002 (2007).

[16] P. H. Bucksbaum, R. R. Freeman, M. Bashkansky, and T. J. McIlrath, "Role of the ponderomotive potential in above-threshold ionization", J. Opt. Soc. Am. B, JOSAB **4**, 760–764 (1987).

[17] L. V. Keldysh, "Ionization in the field of a strong electromagnetic wave", Sov. Phys. JETP **20** (1965).

[18] M. Y. Ivanov, M. Spanner, and O. Smirnova, "Anatomy of strong field ionization", Journal of Modern Optics **52**, 165–184 (2005).

[19] A. McPherson et al., "Studies of multiphoton production of vacuum-ultraviolet radiation in the rare gases", J. Opt. Soc. Am. B, JOSAB **4**, 595–601 (1987).

[20] M. Ferray, A. L'Huillier, X. F. Li, L. A. Lompre, G. Mainfray, and C. Manus, "Multiple-harmonic conversion of 1064 nm radiation in rare gases", J. Phys. B: At. Mol. Opt. Phys. **21**, L31 (1988).

[21] P. Salières, A. L'Huillier, P. Antoine, and M. Lewenstein, "Study of The Spatial and Temporal Coherence of High-Order Harmonics", in *Advances In Atomic, Molecular, and Optical Physics*, Vol. 41, edited by B. Bederson and H. Walther (Academic Press, Jan. 1, 1999), pp. 83–142.

[22] C. J. Foot, *Atomic Physics*, Oxford Master Series in Physics (Oxford University Press, Oxford, New York, Nov. 25, 2004), 344 pp.

[23] H. R. Reiss, "Theoretical methods in quantum optics: S-matrix and Keldysh techniques for strong-field processes", Progress in Quantum Electronics **16**, 1–71 (1992).

[24] I. I. Rabi, "Space Quantization in a Gyrating Magnetic Field", Phys. Rev. **51**, 652–654 (1937).

[25] S. H. Autler and C. H. Townes, "Stark Effect in Rapidly Varying Fields", Phys. Rev. **100**, 703–722 (1955).

[26] I. Lindgren and J. Morrison, *Atomic Many-Body Theory*, 2nd ed., Springer Series on Atomic, Optical, and Plasma Physics (Springer-Verlag, Berlin Heidelberg, 1986).

[27] C. F. Fischer, T. Brage, and P. Jönsson, *Computational Atomic Structure: An MCHF Approach* (Routledge, New York, Feb. 14, 2022), 280 pp.

[28] D. A. Varshalovich, A. N. Moskalev, and V. K. Khersonskii, *Quantum Theory of Angular Momentum* (World Scientific, Oct. 1988).

[29] A. Szabo and N. S. Ostlund, *Modern Quantum Chemistry: Introduction to Advanced Electronic Structure Theory* (Dover Publications, 1996), 480 pp.

[30] W. Kuhn, "Über die Gesamtstärke der von einem Zustande ausgehenden Absorptionslinien", Z. Physik **33**, 408–412 (1925).

[31] J. Jackson, *Classical electrodynamics* (Wiley, Jan. 1, 2012).

[32] A. D. Bandrauk, F. Fillion-Gourdeau, and E. Lorin, "Atoms and molecules in intense laser fields: gauge invariance of theory and models", J. Phys. B: At. Mol. Opt. Phys. **46**, 153001 (2013).

[33] D. H. Kobe, "Gauge-invariant resolution of the controversy over length versus velocity forms of the interaction with electric dipole radiation", Phys. Rev. A **19**, 205–214 (1979).

[34] L. B. Madsen, "Gauge invariance in the interaction between atoms and few-cycle laser pulses", Phys. Rev. A **65**, 053417 (2002).

[35] D. H. Kobe and A. L. Smirl, "Gauge invariant formulation of the interaction of electromagnetic radiation and matter", American Journal of Physics **46**, 624–633 (1978).

[36] E. Cormier and P. Lambropoulos, "Optimal gauge and gauge invariance in nonperturbative time-dependent calculation of above-threshold ionization", J. Phys. B: At. Mol. Opt. Phys. **29**, 1667–1680 (1996).

[37] U. Fano, "Propensity rules: An analytical approach", Phys. Rev. A **32**, 617–618 (1985).

[38] D. Busto et al., "Fano's Propensity Rule in Angle-Resolved Attosecond Pump-Probe Photoionization", Phys. Rev. Lett. **123**, 133201 (2019).

[39] H. Margenau, "Van der Waals Potential in Helium", Phys. Rev. **56**, 1000–1008 (1939).

[40] N. Rohringer, A. Gordon, and R. Santra, "Configuration-interaction-based time-dependent orbital approach for ab initio treatment of electronic dynamics in a strong optical laser field", Phys. Rev. A **74**, 043420 (2006).

[41] L. Greenman, P. J. Ho, S. Pabst, E. Kamarchik, D. A. Mazziotti, and R. Santra, "Implementation of the time-dependent configuration-interaction singles method for atomic strong-field processes", Phys. Rev. A **82**, 023406 (2010).

[42] T. Sato, T. Teramura, and K. L. Ishikawa, "Gauge-Invariant Formulation of Time-Dependent Configuration Interaction Singles Method", Applied Sciences **8**, 433 (2018).

[43] K. L. Ishikawa and T. Sato, "A Review on Ab Initio Approaches for Multielectron Dynamics", IEEE Journal of Selected Topics in Quantum Electronics **21**, 1–16 (2015).

[44] L. Tao and A. Scrinzi, "Photo-electron momentum spectra from minimal volumes: the time-dependent surface flux method", New J. Phys. **14**, 013021 (2012).

[45] Y. Orimo, T. Sato, and K. L. Ishikawa, "Application of the time-dependent surface flux method to the time-dependent multiconfiguration self-consistent-field method", Phys. Rev. A **100**, 013419 (2019).

[46] F. Morales, T. Bredtmann, and S. Patchkovskii, "iSURF: a family of infinite-time surface flux methods", J. Phys. B: At. Mol. Opt. Phys. **49**, 245001 (2016).

[47] D. M. Wolkow, "Über eine Klasse von Lösungen der Diracschen Gleichung", Z. Physik **94**, 250–260 (1935).

[48] F. H. M. Faisal, "Multiple absorption of laser photons by atoms", J. Phys. B: At. Mol. Phys. **6**, L89–L92 (1973).

[49] H. R. Reiss, "Effect of an intense electromagnetic field on a weakly bound system", Phys. Rev. A **22**, 1786–1813 (1980).

[50] J.-A. You, N. Rohringer, and J. M. Dahlström, "Attosecond photoionization dynamics with stimulated core-valence transitions", Phys. Rev. A **93**, 033413 (2016).

[51] J. J. Sakurai and J. Napolitano, *Modern quantum mechanics*, 2nd ed. (Cambridge University Press, Cambridge, 2017).

[52] W. Becker, F. Grasbon, R. Kopold, D. B. Milošević, G. G. Paulus, and H. Walther, "Above-Threshold Ionization: From Classical Features to Quantum Effects", in *Advances In Atomic, Molecular, and Optical Physics*, Vol. 48, edited by B. Bederson and H. Walther (Academic Press, Jan. 1, 2002), pp. 35–98.

[53] A. Palacios, C. W. McCurdy, and T. N. Rescigno, "Extracting amplitudes for single and double ionization from a time-dependent wave packet", Phys. Rev. A **76**, 043420 (2007).

[54] D. E. Manolopoulos, "Derivation and reflection properties of a transmission-free absorbing potential", The Journal of Chemical Physics **117**, 9552 (2002).

[55] C. W. McCurdy and F. Martín, "Implementation of exterior complex scaling in B-splines to solve atomic and molecular collision problems", J. Phys. B: At. Mol. Opt. Phys. **37**, 917–936 (2004).

[56] Y. Orimo, T. Sato, A. Scrinzi, and K. L. Ishikawa, "Implementation of the infinite-range exterior complex scaling to the time-dependent complete-active-space self-consistent-field method", Phys. Rev. A **97**, 023423 (2018).

[57] A. Scrinzi, "Infinite-range exterior complex scaling as a perfect absorber in time-dependent problems", Phys. Rev. A **81**, 053845 (2010).

[58] A. Karamatskou, S. Pabst, Y.-J. Chen, and R. Santra, "Erratum: Calculation of photoelectron spectra within the time-dependent configuration-interaction singles scheme [Phys. Rev. A 89, 033415 (2014)]", Phys. Rev. A **91**, 069907 (2015).

[59] L. Landau and E. Lifshitz, *Quantum mechanics: Non-relativistic theory*, Course of Theoretical Physics (Elsevier Science, 1991).

[60] S. Carlström, M. Spanner, and S. Patchkovskii, "General time-dependent configuration-interaction singles. I. Molecular case", Phys. Rev. A **106**, 043104 (2022).

[61] Y. Saad, *Iterative Methods for Sparse Linear Systems*, Other Titles in Applied Mathematics (Society for Industrial and Applied Mathematics, Jan. 1, 2003), 537 pp.

[62] S. Patchkovskii and H. G. Muller, "Simple, accurate, and efficient implementation of 1-electron atomic time-dependent Schrödinger equation in spherical coordinates", Computer Physics Communications **199**, 153–169 (2016).

[63] A. D. Becke, "A multicenter numerical integration scheme for polyatomic molecules", J. Chem. Phys. **88**, 2547–2553 (1988).

[64] L. Rosenberg, "Levinson-Seaton theorem for potentials with an attractive Coulomb tail", Phys. Rev. A **52**, 3824–3826 (1995).

[65] H. Friedrich, *Theoretical Atomic Physics*, 1st ed. (Springer Berlin, Heidelberg, 1991), IX, 316.

[66] B. Simon, "The definition of molecular resonance curves by the method of exterior complex scaling", Physics Letters A **71**, 211–214 (1979).

[67] A. Scrinzi and N. Elander, "A finite element implementation of exterior complex scaling for the accurate determination of resonance energies", J. Chem. Phys. **98**, 3866–3875 (1993).

[68] C. Leforestier et al., "A comparison of different propagation schemes for the time dependent Schrödinger equation", Journal of Computational Physics **94**, 59–80 (1991).

[69] E. Lindroth and J. M. Dahlström, "Attosecond delays in laser-assisted photodetachment from closed-shell negative ions", Phys. Rev. A **96**, 013420 (2017).

[70] J. Vinbladh, J. M. Dahlström, and E. Lindroth, "Many-body calculations of two-photon, two-color matrix elements for attosecond delays", Phys. Rev. A **100**, 043424 (2019).

[71] J. Caillat et al., "Attosecond Resolved Electron Release in Two-Color Near-Threshold Photoionization of N_2", Phys. Rev. Lett. **106**, 093002 (2011).

[72] F. Calegari et al., "Ultrafast electron dynamics in phenylalanine initiated by attosecond pulses", Science **346**, 336–339 (2014).

[73] Á. Jiménez-Galán, L. Argenti, and F. Martín, "Modulation of Attosecond Beating in Resonant Two-Photon Ionization", Phys. Rev. Lett. **113**, 263001 (2014).

[74] J. Cooper and R. N. Zare, "Angular Distribution of Photoelectrons", J. Chem. Phys. **48**, 942–943 (1968).

[75] J. W. Cooper, "Photoelectron-angular-distribution parameters for rare-gas subshells", Phys. Rev. A **47**, 1841–1851 (1993).

[76] D. M. Villeneuve, P. Hockett, M. J. J. Vrakking, and H. Niikura, "Coherent imaging of an attosecond electron wave packet", Science **356**, 1150–1153 (2017).

[77] S. Heuser et al., "Angular dependence of photoemission time delay in helium", Phys. Rev. A **94**, 063409 (2016).

[78] C. Cirelli et al., "Anisotropic photoemission time delays close to a Fano resonance", Nat Commun **9**, 1–9 (2018).

[79] I. A. Ivanov and A. S. Kheifets, "Angle-dependent time delay in two-color XUV+IR photoemission of He and Ne", Phys. Rev. A **96**, 013408 (2017).

[80] J. M. Dahlström et al., "Theory of attosecond delays in laser-assisted photoionization", Chemical Physics, Attosecond Spectroscopy **414**, 53–64 (2013).

[81] R. R. Freeman, P. H. Bucksbaum, H. Milchberg, S. Darack, D. Schumacher, and M. E. Geusic, "Above-threshold ionization with subpicosecond laser pulses", Phys. Rev. Lett. **59**, 1092–1095 (1987).

[82] G. Grynberg, A. Aspect, C. Fabre, and C. Cohen-Tannoudji, *Introduction to Quantum Optics by Gilbert Grynberg* (Sept. 2010).

[83] V. C. Reed and K. Burnett, "Role of resonances and quantum-mechanical interference in the generation of above-threshold-ionization spectra", Phys. Rev. A **43**, 6217–6226 (1991).

[84] R. R. Jones, C. S. Raman, D. W. Schumacher, and P. H. Bucksbaum, "Ramsey interference in strongly driven Rydberg systems", Phys. Rev. Lett. **71**, 2575–2578 (1993).

[85] R. R. Jones, "Interference Effects in the Multiphoton Ionization of Sodium", Phys. Rev. Lett. **74**, 1091–1094 (1995).

[86] P. V. Demekhin and L. S. Cederbaum, "Dynamic Interference of Photoelectrons Produced by High-Frequency Laser Pulses", Phys. Rev. Lett. **108**, 253001 (2012).

[87] M. Baghery, U. Saalmann, and J. M. Rost, "Essential Conditions for Dynamic Interference", Phys. Rev. Lett. **118**, 143202 (2017).

[88] M. Gavrila, "Atomic stabilization in superintense laser fields", J. Phys. B: At. Mol. Opt. Phys. **35**, R147–R193 (2002).

[89] K. Toyota, O. I. Tolstikhin, T. Morishita, and S. Watanabe, "Siegert-state expansion in the Kramers-Henneberger frame: Interference substructure of above-threshold ionization peaks in the stabilization regime", Phys. Rev. A **76**, 043418 (2007).

[90] K. Toyota, O. I. Tolstikhin, T. Morishita, and S. Watanabe, "Interference substructure of above-threshold ionization peaks in the stabilization regime", Phys. Rev. A **78**, 033432 (2008).

[91] O. I. Tolstikhin, "Siegert-state expansion for nonstationary systems. IV. Three-dimensional case", Phys. Rev. A 77, 032712 (2008).

[92] W.-C. Jiang and J. Burgdörfer, "Dynamic interference as signature of atomic stabilization", Opt. Express, OE **26**, 19921–19931 (2018).

[93] I. S. Gradshteyn and I. M. Ryzhik, *Table of Integrals, Series, and Products*, Eighth Edition (Academic Press, 2014), 1156 pp.

[94] L. B. Madsen, "Strong-field approximation in laser-assisted dynamics", American Journal of Physics **73**, 57–62 (2004).

[95] M. Y. Kuchiev, "JETP Letters: issues online", JETP **45**, 319–321 (1987).

[96] A. Maquet and R. Taïeb, "Two-colour IR+XUV spectroscopies: the "soft-photon approximation"", Journal of Modern Optics **54**, 1847–1857 (2007).

[97] D. Arbó, Private communication, Aug. 12, 2021.

[98] S. D. López, S. Donsa, S. Nagele, D. G. Arbó, and J. Burgdörfer, "Phase delays in ω–2ω above-threshold ionization", Phys. Rev. A **104**, 043113 (2021).

[99] D. G. Arbó, S. D. López, and J. Burgdörfer, "Semiclassical strong-field theory of phase delays in ω–2ω above-threshold ionization", Phys. Rev. A **106**, 053101 (2022).

[100] K. Klünder et al., "Probing Single-Photon Ionization on the Attosecond Time Scale", Phys. Rev. Lett. **106**, 143002 (2011).

[101] J. Fuchs et al., "Time delays from one-photon transitions in the continuum", Optica, OPTICA **7**, 154–161 (2020).

[102] P. M. Paul et al., "Observation of a Train of Attosecond Pulses from High Harmonic Generation", Science **292**, 1689–1692 (2001).

[103] E. S. Toma and H. G. Muller, "Calculation of matrix elements for mixed extreme-ultraviolet–infrared two-photon above-threshold ionization of argon", J. Phys. B: At. Mol. Opt. Phys. **35**, 3435 (2002).

[104] G. Laurent, W. Cao, H. Li, Z. Wang, I. Ben-Itzhak, and C. L. Cocke, "Attosecond Control of Orbital Parity Mix Interferences and the Relative Phase of Even and Odd Harmonics in an Attosecond Pulse Train", Phys. Rev. Lett. **109**, 083001 (2012).

[105] I. J. Kim et al., "Highly Efficient High-Harmonic Generation in an Orthogonally Polarized Two-Color Laser Field", Phys. Rev. Lett. **94**, 243901 (2005).

[106] J. Mauritsson, P. Johnsson, E. Gustafsson, A. L'Huillier, K. J. Schafer, and M. B. Gaarde, "Attosecond Pulse Trains Generated Using Two Color Laser Fields", Phys. Rev. Lett. **97**, 013001 (2006).

[107] P. K. Maroju et al., "Attosecond pulse shaping using a seeded free-electron laser", Nature **578**, 386–391 (2020).

[108] V. Véniard, R. Taïeb, and A. Maquet, "Phase dependence of (N+1)-color (N>1) ir-uv photoionization of atoms with higher harmonics", Phys. Rev. A **54**, 721–728 (1996).

[109] Y. Mairesse and F. Quéré, "Frequency-resolved optical gating for complete reconstruction of attosecond bursts", Phys. Rev. A **71**, 011401 (2005).

[110] H. Muller, "Reconstruction of attosecond harmonic beating by interference of two-photon transitions", Appl Phys B **74**, s17–s21 (2002).

[111] M. Swoboda et al., "Phase Measurement of Resonant Two-Photon Ionization in Helium", Phys. Rev. Lett. **104**, 103003 (2010).

[112] S. Haessler et al., "Phase-resolved attosecond near-threshold photoionization of molecular nitrogen", Phys. Rev. A **80**, 011404 (2009).

[113] G. Laurent, W. Cao, I. Ben-Itzhak, and C. L. Cocke, "Attosecond pulse characterization", Opt. Express, OE **21**, 16914–16927 (2013).

[114] P. K. Maroju et al., "Analysis of two-color photoelectron spectroscopy for attosecond metrology at seeded free-electron lasers", New J. Phys. **23**, 043046 (2021).

[115] P. K. Maroju et al., "Attosecond coherent control of electronic wave packets in two-colour photoionization using a novel timing tool for seeded free-electron laser", Nat. Photon., 1–8 (2023).

[116] W. Becker, A. Lohr, and M. Kleber, "Effects of rescattering on above-threshold ionization", J. Phys. B: At. Mol. Opt. Phys. **27**, L325 (1994).

[117] D. Bao, S. G. Chen, and J. Liu, "Rescattering effect in above-threshold ionization processes", Appl. Phys. B **62**, 313–318 (1996).

[118] G. G. Paulus, W. Nicklich, H. Xu, P. Lambropoulos, and H. Walther, "Plateau in above threshold ionization spectra", Phys. Rev. Lett. **72**, 2851–2854 (1994).

[119] G. G. Paulus, W. Becker, and H. Walther, "Classical rescattering effects in two-color above-threshold ionization", Phys. Rev. A **52**, 4043–4053 (1995).

[120] L. J. Zipp, A. Natan, and P. H. Bucksbaum, "Probing electron delays in above-threshold ionization", Optica **1**, 10.1364/OPTICA.1.000361 (2014).

[121] K. C. Prince et al., "Coherent control with a short-wavelength free-electron laser", Nature Photon **10**, 176–179 (2016).

[122] K. J. LaGattuta, "Above-threshold ionization of atomic hydrogen via resonant intermediate states", Phys. Rev. A **47**, 1560–1563 (1993).

[123] M. G. Girju, K. Hristov, O. Kidun, and D. Bauer, "Nonperturbative resonant strong field ionization of atomic hydrogen", J. Phys. B: At. Mol. Opt. Phys. **40**, 4165–4178 (2007).

[124] N. Rohringer and R. Santra, "Resonant Auger effect at high x-ray intensity", Phys. Rev. A 77, 053404 (2008).

[125] A. Palacios, H. Bachau, and F. Martín, "Step-ladder Rabi oscillations in molecules exposed to intense ultrashort vuv pulses", Phys. Rev. A 74, 031402 (2006).

[126] Z. Sun and N. Lou, "Autler-Townes Splitting in the Multiphoton Resonance Ionization Spectrum of Molecules Produced by Ultrashort Laser Pulses", Phys. Rev. Lett. **91**, 023002 (2003).

[127] J. H. Eberly, "Area Theorem rederived", Opt. Express, OE **2**, 173–176 (1998).

[128] G. C. Wick, "The Evaluation of the Collision Matrix", Phys. Rev. **80**, 268–272 (1950).

Publications

THIS THESIS IS ABOUT ionization of atoms by illuminating them with light. We implement theoretical methods to gain information on the photoionization process, with particular focus on multiphoton ionization and strong-field effects in attosecond metrology and coherent control of photoelectrons in free-electron sciences. This work was performed at the Department of Physics at Lund University and defended the 27th of May 2023.

Printed by Media-Tryck, Lund 2023 NORDIC SWAN ECOLABEL 3041 0903

LUND UNIVERSITY

Lund University
Faculty of Engineering
Department of Physics

978-91-8039-514-4